A Novel Phonon-Scintillation Cryogenic Detector and Cabling Solution for Dark Matter Direct Detection

Xiaohe Zhang
St Catherine's College, Oxford



Thesis submitted in partial fulfilment of the requirements for the degree of Doctor of Philosophy at the University of Oxford

Hilary Term, 2015

Abstract

The EDELWEISS experiment is one of the dark matter direct detection experiments. It aims to detect WIMP interactions using an array of cryogenic germanium detectors. In the previous EDELWEISS-II phase, the cables and connectors used have been identified as a major source of neutron background in the experiment, which means that further effort aimed at better WIMP-nucleon interaction detection sensitivity requires a new, different cold cabling solution connecting the detectors to the front-end electronics.

Motivated by this, a new two-section cold cabling system based on semi-flexible laminated copper and stainless steel cables has been developed for the EDELWEISS-III phase at Oxford. Batches of prototypes have been tested first in a cryostat at Oxford as part of a phonon-scintillation detector module, and then at the LSM underground laboratory in several EDELWEISS-III commissioning runs. Following that, a final set of cabling has been produced and installed in the EDELWEISS-III setup, which is currently conducting a science run aiming to improve its sensitivity reach compared to the previous results. This new cold cabling system has shown similar electrical performance as the previous coaxial cabling when comparing different cold cabling configurations in a commissioning run at LSM. Also, its background contribution is within the EDELWEISS-III requirements, according to radioactivity level tests and Monte Carlo simulations. In addition, the assembled connectors have allowed hundreds of signal tracks to be installed within a few days and the low material and space budget has made the cables compatible with the compact cryostat design. Besides reading out detectors for dark matter detection, prototypes of this cabling solution for a wider application range have also been produced at Oxford.

The next generation dark matter direct detection experiments aim to achieve detection sensitivity better by a few orders of magnitude. This requires a target mass at tonne-scale, which converts to thousands of cryogenic detectors. Cryogenic phonon-scintillation detectors used in current dark matter searches can provide excellent performance but they usually require individual tuning and attention, making operation in large-scale experiments difficult. It is also technically challenging to stably produce such detectors in large quantity.

Therefore, a scalable, robust novel detector concept for cryogenic phonon-scintillation detectors to be used in future rare event search experiments has been developed in this work. This detector module consists of a phonon detector based on a $CaMoO_4$ scintillating crystal as the target with an attached NTD-Ge sensor as the thermometer, and a light detector based on a low-temperature PMT. To provide the high voltage necessary for PMT operation while ensuring the detector module can be cooled down and that the performance of the phonon detector is unaffected, a high voltage supply system based on a Cockcroft-Walton generator (CWG), a transformer and a small AC input has been designed and tested in the cryostat. The laminated cabling system is chosen for reading out the phonon channel and connecting the CWG and the PMT. A test run has demonstrated that, the high voltage can be provided to the PMT without causing a problem to the detector operation, and it is feasible to operate the low-temperature PMT at a temperature as low as 17 mK. Testing with a cobalt-57 gamma source, the phonon detector and the light detector have achieved resolutions of 1.07 keV and 34.2 keV for the 122.06 keV peak respectively. This is

close to the performance of detectors used in the current dark matter direct searches, proving this detector concept can be applied to future large-scale dark matter direct detection experiments and other rare event searches.

Using the light channel in this detector setup, the scintillation properties of $CaMoO_4$ has been studied. In this work, the experimental data of its scintillation decay time constant has been extended from the previous 7 K to milli-Kelvin temperatures. The data are interpreted using a three-level model, confirming the existence of a metastable emission level in $CaMoO_4$, and giving various parameters of its emission centre. This suggests that the work related to producing a high voltage supply and demonstrating the excellent performance of a low-temperature PMT could also be attractive to scintillator studies at cryogenic temperatures.

Acknowledgements

The work presented in this thesis would not be possible without the help of many people. First I want to thank my supervisor, Professor Hans Kraus, for giving me the opportunity to do my DPhil work at Oxford, more than 9000 km away from my hometown. His vast knowledge and experience in physics have been invaluable throughout my research.

The staff of various workshops in the physics department has also made a great contribution to my DPhil research. Paul Pattinson and Martin Scott of PFU, a big thank you for patiently trying out all my ideas and pushing limits for the laminated cables, and helping me in any way you can during the cabling mass production. Mike Tacon and everyone in the mechanical workshop, thank you for sharing your expertise when I tried to design the connector and other pieces, and making the drawings become reality. I also want to thank Robert Storey, who has been really kind and tried his best to provide the liquid helium at short notice when things went wrong. And thank you every one in the electronics workshop for all your help.

Working as a member of the EDELWEISS collaboration has been a great experience. In particular, the super-intense installation trips to LSM will always be special memories for me. I am really grateful to the whole collaboration.

I would also like to thank all my colleagues in the group. You have provided enormous help in my work and made the office / lab a very pleasant environment. A special thanks to Mark Pipe for all the work in our attempts to cool a PMT in the S400 cryostat (it is really sad that things have not turned out as expected…), and Junsong Lin, who has helped me in so many ways.

Thank you to the China Scholarship Council for funding my DPhil work.

My life at Oxford would be very different without all my friends. Thank you all for the amazing house renting experience, the weekend dinners and the holiday trips. I will always remember the Chinese New Year, the Christmas and all the other traditional holidays we celebrated in UK.

And finally, mum and dad, whose support means everything to me. Thank you for encouraging my curiosity about the world, which makes me who I am.

Table of Contents

Introduction 1

1 Dark Matter and Detection 4

1.1 Astrophysical Evidence for Dark Matter 4

1.1.1 Rotation Curves of Spiral Galaxies 4

1.1.2 Gravitational Lensing 6

1.2 Dark Matter in Cosmology 8

1.2.1 Cosmic Microwave Background 10

1.2.2 Big Bang Nucleosynthesis 11

1.3 Dark Matter Candidates 13

1.3.1 Properties of Dark Matter 13

1.3.2 WIMP 14

1.4 WIMP Searches 17

1.4.1 Direct Detection 18

1.4.2 Direct Detection Techniques 22

1.4.3 Indirect Detection 26

1.4.4 Detection in Particle Colliders 28

2 The EDELWEISS and EURECA Experiment 30

2.1 The EDELWEISS Experiment 30

2.1.1 Radioactive Background Sources and EDELWEISS Shielding Setup 31

2.1.2 Cryogenic Germanium Detectors 32
2.1.3 Final Results of EDELWEISS-II 36
2.1.4 EDELWEISS-III Prospects 38
2.2 The EURECA Experiment 38
3 Laminated Semi-Flexible Cabling System 41
3.1 General Cable Construction and Fabrication Process 42
3.1.1 Laminated Cables 42
3.1.2 Low-Radioactive Connectors 47
3.2 Radioactive Background Control and Material screening 49
3.2.1 Element Screening Based on (α, n) Reaction Cross-Section 50
3.2.2 Radioactivity Contaminations Test Results 54
3.3 Capacitance 55
3.3.1 Design Implications 56
3.3.2 Numerical Calculation and Measurements 59
3.4 Heatload 62
3.4.1 Temperature Stages in Dilution Refrigerator 62
3.4.2 Thermal Conductivity 65
3.4.3 Heatload Calculation 66
3.4.4 Heat Anchoring Quality 70
3.5 Final Design 72
4 Cabling Applications and Performance 76

4.1 Application in EDELWEISS-III 76
4.2 Performance 81
4.2.1 Microphonic Noise and Noise Spectra 82
4.2.2 Resolution with Different Cabling Setups 85
4.2.3 Estimated Background in EDELWEISS-III Induced by Cold Cabling 86
4.3 Future Applications in EURECA and Other Rare Event Searches 89
5 Cryogenic Phonon-Scintillation Detector Development 92
5.1 Detector Setup 93
5.1.1 Detector Module Layout 93
5.1.2 Detector Housing 97
5.2 Target Crystal – Scintillator 106
5.3 Heat Channel – NTD-Ge Sensor 109
5.3.1 Resistance of the NTD-Ge Sensor 109
5.3.2 Sensitivity of the NTD-Ge Sensor 111
5.3.3 Heat Capacity 112
5.3.4 Linearity of Response 115
5.3.5 Data Acquisition for Phonon Detector 116
5.4 Light Channel - Low Temperature PMT 119
5.4.1 PMT Cryogenic Light Detector 119
5.4.2 High Voltage Power Supply 120
5.4.3 Light Detector Readout System 126

6 Phonon-Scintillation Detector Tests and Data Analysis 128

6.1 Light Detector Operation and PMT response 129

6.1.1 HV Supply Frequency Response 129

6.1.2 Effects on Phonon Channel Signal from PMT HV Supply 130

6.1.3 PMT Response at Low Temperature 133

6.2 Test Source – Cobalt-57 136

6.3 Data Processing 139

6.3.1 Phonon Detector Data Analysis 140

6.3.2 Light Detector Data Analysis 145

6.3.3 Pulse Correlation 146

6.4 Energy Spectrum and Resolution 149

6.4.1 Phonon Detector Energy Resolution 149

6.4.2 Light Detector Energy Resolution 153

6.4.3 Light Collection 155

6.4.4 Light Yield Plot 157

6.5 Temperature Dependence of $CaMoO_4$ Scintillation Decay Time 158

6.5.1 Decay Constant Measurement 158

6.5.2 Temperature Dependence 160

Conclusions and Perspectives 164

Appendix A 169

Bibliography 172

Introduction

The study of dark matter has been on-going ever since Fritz Zwicky postulated the concept in the 1930s, and then Vera Rubin and Kent Ford showed flat rotation curves for many galaxies in the 1970s. There is compelling cosmological and astrophysical evidence suggesting that the majority of matter in the Universe is attributed to the non-luminous dark matter. Its exact nature is as yet unknown but many candidates have been proposed. Amongst them, a general class of weakly interacting massive particles (WIMPs) is currently the most motivated one and the target of many dark matter detection experiments. There are different methods of detecting WIMPs, one of them being the direct detection method which searches for the recoil energy deposited in the detector when a WIMP is scattered by the target nuclei. Many technologies have been developed and are currently employed in dark matter direct detection experiments around the world, and this thesis focuses on one of them that uses cryogenic detectors operated at milli-Kelvin temperatures. The EDELWEISS experiment is such a dark matter direct detection experiment, which aims to detect WIMP interactions using an array of cryogenic germanium detectors located at the LSM underground laboratory.

In the previous EDELWEISS-II phase, which concluded in 2010, the cables and connectors have been identified as a major source of neutron background in the experiment. The following upgraded EDELWEISS-III phase, aiming at better WIMP-nucleon interaction detection sensitivity, therefore requires a different cold cabling solution that runs in the vicinity of the detectors. Because of this necessity, a new

two-section cold cabling system based on semi-flexible laminated copper and stainless steel cables for EDELWEISS-III has been developed in this work.

In the future, after EDELWEISS-III, the next generation dark matter direct detection experiments aim to achieve a detection sensitivity that is higher by a few orders of magnitude. For example, EDELWEISS will be collaborating with other groups around Europe to combine their expertise in building the EURECA experiment – a facility that can house a target of up to 1000 kg mass, which converts to thousands of phonon-ionisation and phonon-scintillation cryogenic detectors.

Cryogenic phonon-scintillation detectors used in current dark matter searches can provide excellent performance but they usually require individual tuning and attention. Operating thousands of these detectors in parallel will require a huge amount of effort. It is also technically challenging to stably produce such detectors in large quantities. Therefore, the remaining part of this work focuses on the development of a scalable, robust novel detector concept for cryogenic phonon-scintillation detectors to be used in future rare event search experiments.

This thesis begins with an overview of dark matter and its detection in Chapter 1. Then in Chapter 2, the EDELWEISS experiment, its setup, the EDELWEISS-II result and EDELWEISS-III prospect are described. The future EURECA experiment is also introduced here.

Chapter 3 focuses on introducing the design of the semi-flexible laminated cabling solution that I developed for EDELWEISS-III. The general cable construction and fabrication processes are described. Then different aspects to be considered concerning the laminated cables and their implications on various parameters are discussed. The final design is also described in this chapter. Chapter 4 presents the application and performance of this cabling system. Its application in the

EDELWEISS-III is described first, followed by the performance of this cabling solution during prototype tests and EDELWEISS runs. The possibility of applying it to next generations of dark matter direct detections and other rare event searches is also introduced here.

Chapter 5 moves on to the cryogenic phonon-scintillation detector concept developed for future rare event search experiments. This chapter first outlines the general setup of the prototype detector module. It then discusses the configurations and properties of individual components, including the target crystal, the phonon detector and the light detector, in detail. The feasibility and performance of this phonon-scintillation prototype detector is tested in the K400 cryostat at Oxford. The detector response and test results are discussed in Chapter 6. Finally, the temperature dependence of the scintillation decay time of the $CaMoO_4$ target crystal, covering the range down to milli-Kelvin temperatures, obtained using this setup is also presented and discussed in this chapter.

1 Dark Matter and Detection

Dark matter is inferred to exist from gravitational effects on visible matter and background radiation, but is undetectable through emitted or scattered electromagnetic radiation. It plays a crucial role in explaining many observations in large-scale astrophysical systems. Although the exact nature of dark matter is not known yet, there is strong evidence supporting its existence.

This chapter will start with presenting some astrophysical evidence for the existence of dark matter, and then describe the cosmological aspects of it. Following that, potential dark matter candidates are introduced. In the next section, different schemes of detection are presented. Some experiments aiming to detect dark matter are also briefly introduced here.

1.1 Astrophysical Evidence for Dark Matter

The story of dark matter starts with astrophysical observations. It was first postulated by Fritz Zwicky in the 1930s to account for the "missing mass" in the Coma Cluster of galaxies [1, 2]. In the following 80 years since then, as more and more observational evidence has emerged, it has become rather difficult to deny its existence in the Universe. In this section, some of the most important astrophysical evidence is presented.

1.1.1 Rotation Curves of Spiral Galaxies

Galaxies are massive, gravitationally bound systems. In spiral galaxies, most of the observable matter concentrates within a thin central plane, known as the disk. The

stars, gas and dust in the disk rotate around the Galactic Centre in roughly circular orbits. The orbital velocity distribution is related to the density profile of the galaxy - for a certain star that orbits at a radius *r*, its velocity *v* is given by Kepler's Law:

$$v = \sqrt{\frac{GM(r)}{r}}, \tag{1.1}$$

where *M(r)* is the mass within the orbit. This means when the stars and other luminous matter within the radius *r* are all taken into account, the rotation velocity should fall off as $1/\sqrt{r}$ as the radius increases.

But Zwicky's study shows that the rotation velocity of objects in the Coma Cluster is much larger than this prediction if only considering the luminous matter alone [1, 2]. This is further supported by measurements of the rotation curves of many other galaxies [3, 4, 5]. In fact, the rotation curves are observed to be roughly flat, which requires a much larger average density within the galaxies. The most likely explanation for this discrepancy is that the galaxies consist mainly of a spherical non-luminous "dark matter" halo.

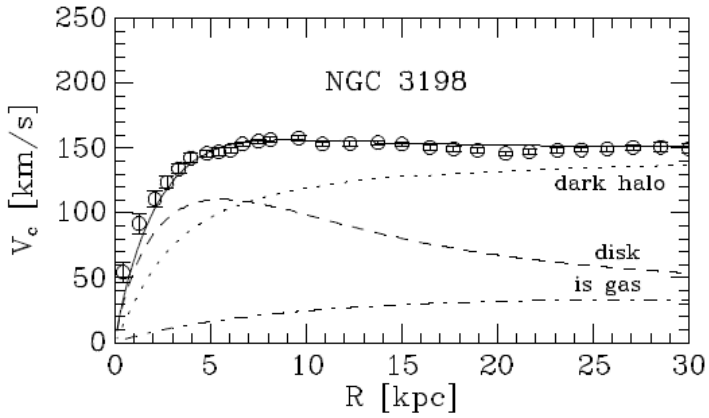


Figure 1.1: The rotation curve of galaxy NGC 3198. Circles with error bars are observed data. The solid line represents a fit to the data. The dashed line, dotted line and dot-dashed line are calculated contributions from the stellar disk, the necessary dark matter halo and gas, respectively. Plot taken from [6] (with permission from Springer).

As an example, Figure 1.1 shows the rotation curve of spiral galaxy NGC 3198 and one way of decomposing it into various contributing entities.

1.1.2 Gravitational Lensing

More compelling evidence for the existence of dark matter has been obtained by exploiting the phenomenon of gravitational lensing. As described by Einstein's theory of General Relativity, the space-time around a massive object is curved. As a consequence, the path of photons is deflected towards the massive object as they pass through the gravitational field, and this massive object acts as a lens. This effect can be used to probe the dark sector as the mass of the lensing matter can be calculated based on the observation and it can be any kind of matter, luminous or not.

Strong Lensing

When the source, the lensing mass and the telescope are in a very good alignment, then strong-lensing occurs. This lensing effect can be so strong that light emitted by the source can travel along multiple paths around the lensing mass and all deflected back to the telescope, hence multiple images appear. In the rare case of perfect alignment, instead of a point-like light source, the image observed will be a luminous circle [7], which is called the "Einstein ring". One example of Galaxy cluster Abell 2218 acting as a powerful lens is shown in Figure 1.2. Strong lens studies of galaxies and clusters of galaxies have shown that these systems are dominated by a non-baryonic dark matter component [8].



Figure 1.2: Strong gravitational lensing created by the galaxy cluster Abell 2218. The arc-shaped patterns are the distorted images of very distant galaxies. Image credit: NASA, ESA, Andrew Fruchter (STScI), and the ERO team (STScI + ST-ECF) (released under the Creative Commons Attribution 3.0 Unported license).

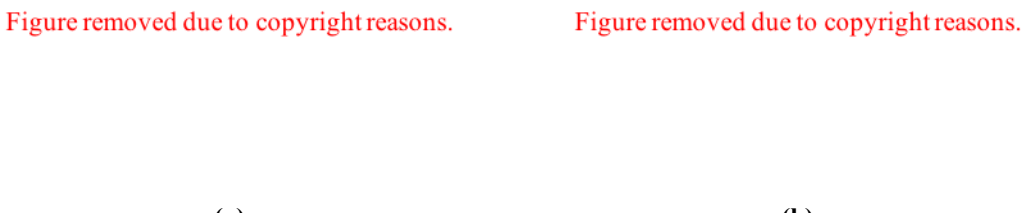
Weak Lensing

In most cases, the distortions of background sources are much smaller and the weak lensing measurement is applied, which involves a statistical study of the lensing effects. By measuring the shapes and orientations of large numbers of galaxies, a mass density profile can be determined.

Another remarkable piece of supporting evidence for dark matter lies in the studies of the merging cluster 1E 0657-558 – the "Bullet Cluster". It is a cluster merger observed shortly after the collision of two sub-clusters.

Based on both wide-field ground-based images and images taken by the Advanced Camera for Surveys (ACS) on the Hubble Space Telescope (HST), Clowe et al. constructed a map of the gravitational potential using weak gravitational lensing as shown in Figure 1.3 (a), which approximately traces the distribution of galaxies. Meanwhile, Figure 1.3 (b) shows the X-ray emissivity map (coloured cloud) from Chandra X-ray Observatory [9]. Since the X-ray emitting plasma is the dominant baryonic matter contribution [10], this effectively shows the baryonic mass distribution. Clearly, the superimposed gravitational potential distribution (green contour lines) does not coincide with the baryonic matter distribution.

This observation is explained by the collisionless nature of dark matter. During the initial collision, the X-ray plasma of each sub-cluster interacts strongly and is slowed down. On the other hand, the dark matter, contributing the majority of the total mass, underwent almost no interaction and passed through each other along with galaxies. This is consistent with the theoretical prediction.



(a) **(b)**

Figure 1.3: Images of the Bullet Cluster: (a) Colour image from the Magellan images of the merging cluster. The green contour lines show the gravitational potential distribution; (b) 500 ks Chandra image of the cluster. The coloured cloud indicates the plasma density. Taken from [9].

1.2 Dark Matter in Cosmology

As the predominant component of matter in the Universe, how does dark matter fit in the big picture? How much dark matter is there? This section will mainly describe the indications of dark matter on a cosmological scale.

In modern cosmology, a basic belief is that the Universe is homogenous and isotropic on a large scale. This is known as the cosmological principle and supported by the observations so far. Taking this assumption, and using general relativity, the Friedmann equation can be obtained [11, 12]:

$$H^2 = \left(\frac{\dot{a}}{a}\right)^2 = \frac{8\pi G}{3}\rho - \frac{k}{a^2} + \frac{\Lambda}{3}, \tag{1.2}$$

where H is the time-dependent Hubble parameter and Λ is the cosmological constant.

The term k in Equation (1.2) is linked to the geometry of the Universe. The three different possible geometries are spherical, flat and hyperbolic, corresponding to k being positive, zero and negative respectively.

For a given value of H, the special value of the density that is required by a flat Universe, $k = 0$, is known as the critical density ρ_c:

$$\rho_c = \frac{3H^2}{8\pi G}. \tag{1.3}$$

Although the Universe is not necessarily flat, the critical density sets a natural scale for the density of the Universe. Consequently, the matter density is usually expressed as the density parameter Ω_m:

$$\Omega_m \equiv \frac{\rho}{\rho_c}. \tag{1.4}$$

Similarly, it is convenient to also define a density parameter for the cosmological constant as:

$$\Omega_\Lambda = \frac{\Lambda}{3H^2}. \tag{1.5}$$

Therefore,

$$\Omega_m + \Omega_\Lambda = 1 + \frac{k}{a^2H^2}. \tag{1.6}$$

So far, observations are all consistent with a flat Universe, where $k = 0$, $\Omega_m + \Omega_\Lambda = 1$.

Considering the contribution of different components, the mass density parameter can be further separated into a baryonic matter part and a dark matter part:

$$\Omega_m = \Omega_b + \Omega_{DM}. \tag{1.7}$$

These parameters can be determined from combining different observations [13].

1.2.1 Cosmic Microwave Background

In its infancy, the Universe was filled with a hot, opaque plasma of electrons and baryons. Photons were constantly scattered, making it impossible for them to travel any considerable distances. Approximately 380,000 years after the Big Bang, as the Universe expanded, it cooled down to a temperature of 3000 K – cold enough for the electrons and protons to combine into neutral hydrogen atoms. This transition is known as the recombination. After recombination, since hydrogen atoms are very ineffective at scattering light, the Universe suddenly became transparent to photons, allowing them to decouple from matter and travel freely. The average photon from the surface of last scattering has never interacted again and is detected by us today as the Cosmic Microwave Background (CMB).

Although the CMB is isotropic on large scale, there are actually slight temperature variations between photons coming from different directions of the sky. This is caused by the baryon acoustic oscillations (BAO) in the primordial baryon-photon fluid before recombination. Tiny density fluctuations of this baryon-photon fluid created gravitational potential wells that attracted and compressed baryons. This then resulted in a hotter plasma with increased outward radiation pressure from the photons. These two opposite forces gave rise to BAO. At the time of recombination, the pattern of oscillations was imprinted in the CMB as the photons left the surface of last scattering [14, 15].

The anisotropies in the CMB can be modelled using several important parameters describing the Universe. Fitting the predicted model to measured CMB spectra can answer many key questions of the Universe, including what percentage baryonic matter and dark matter contribute to the total mass density. Figure 1.4 is the

temperature power spectrum of the CMB background measured by the Planck collaboration. Using the best-fit, the parameters (68% limits) are calculated as:

$$\Omega_b h^2 = 0.02207 \pm 0.00033\,;$$

$$\Omega_{DM} h^2 = 0.1196 \pm 0.0031\,;$$

$$\Omega_\Lambda = 0.686 \pm 0.020\,,$$

where h is the dimensionless reduced Hubble parameter $H_0/(100\ \mathrm{km{\cdot}s^{-1}{\cdot}Mpc^{-1}})$, and H_0 is the Hubble constant. This indicates that the Universe consists of ~5% baryonic matter, ~27% dark matter and ~68% dark energy.

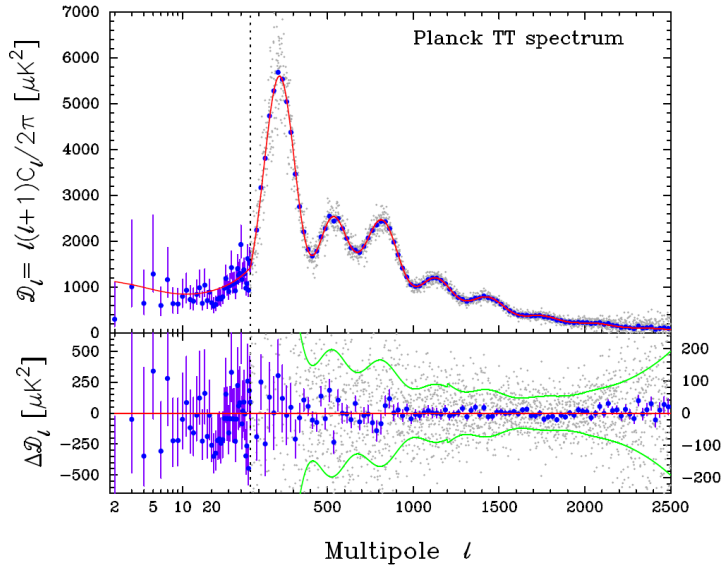


Figure 1.4: Planck temperature power spectrum, taken from [16] (with permission from A&A). The red solid line is the best fit. The peak positions and heights reveal a number of aspects of the Universe. Amongst them, the spectrum shows that atomic matter only constitutes 5% of the Universe, while dark matter contributes 27%. The remaining 68% is contributed by dark energy.

1.2.2 Big Bang Nucleosynthesis

Besides the CMB, the cosmic baryon density can also be constrained by Big Bang Nucleosynthesis (BBN) – the production of light nuclei more complex than hydrogen in the early Universe.

At approximately 3 minutes after the Big Bang, as the Universe expanded and cooled, it became cold enough to allow the formation of elements heavier than

hydrogen. At this point, the process of BBN began until the nuclear reactions became quenched due to the low temperatures and densities less than half an hour later. In BBN, deuterium, helium-3, helium-4 and lithium-7 were produced. The abundances of these light elements depend largely on the fraction of the Universe that is made up of baryonic matter. [17]



Figure 1.5: The abundances of ^{4}He, D, ^{3}He, and ^{7}Li as predicted by the standard model of Big Bang Nucleosynthesis. The solid bands show the 95% CL range. The boxes show the observed light element abundances (smaller boxes: with ±2σ statistical errors; larger boxes: with ±2σ statistical and systematic errors). The narrow and wide vertical bands indicate the baryon density range determined by CMB and the BBN concordance range respectively, each at 95% CL. Plot taken from [18].

Figure 1.5 shows the predictions of BBN and the observed data. It provides a measure of the baryon content:

$$0.019 \leq \Omega_b h^2 \leq 0.024\ (95\%\ CL)\ .$$

This gives a cosmic baryon budget of only ~5%, which is consistent with the CMB result. This indicates that any further matter contribution in the Universe must be non-baryonic, such as dark matter.

1.3 Dark Matter Candidates

With compelling evidence supporting the existence of dark matter, the subsequent question naturally is: what is dark matter made of? Although this is still unresolved, a considerable number of dark matter candidates have been considered so far. This section will first discuss the properties required of a particle to be a candidate and then focus on the most plausible one – WIMP.

1.3.1 Properties of Dark Matter

Obviously, dark matter must be optically dark as it has not been observed yet, thus does not interact electromagnetically. Some baryonic matter could in principle contribute to dark matter, such as white dwarfs, neutron stars, back holes, etc. that are too dim to be detected. They are known as MACHOs – Massive Compact Halo Objects. But as BBN limits the total amount of baryonic matter to ~5%, the majority of dark matter must be non-baryonic [19, 20]. Observations also suggest that dark matter must have very weak interactions with baryonic matter as well as a very small self-interaction cross-section [9].

Based on their velocities, dark matter candidates can be roughly divided into “Hot Dark Matter” or “Cold Dark Matter”. Hot dark matter consists of particles travelling at relativistic speeds. For example, neutrinos are important candidates for hot dark matter. However, hot dark matter alone is not sufficient to comprise the full mass of non-baryonic dark matter. Also, due to its relativistic speed, hot dark matter would have interfered with the process of galaxy formation, putting theoretical models in

conflict with observations [21]. On the other hand, cold dark matter (CDM) consists of particles travelling at non-relativistic velocities. WIMPs are very important candidates in this category. CDM fits better with the observations and simulations of galaxy formation, and thus is generally favoured as the dark matter model.

In addition, dark matter particles must be stable on cosmological time scales to still exist today and have the right relic density to fit the observations.

No fundamental particle within the standard model of particle physics has all the required properties of dark matter. Hence a series of new particles beyond the Standard Model are nominated as the non-baryonic CDM candidates in literature [18, 22, 23]. Amongst them, a general class of weakly interacting massive particles (WIMPs) is the most motivated one and the target of many dark matter detection experiments.

1.3.2 WIMP

The name of this class of particles already contains the main information about its nature. A WIMP (usually denoted as χ) typically has a mass in the range of 10 GeV to a few TeV, and with cross-sections around the scale of weak interaction. WIMPs share many of the properties of neutrinos, but are much heavier, and thus slower. One of the main motivations for WIMPs comes from the fact that if they were in equilibrium in the early Universe, they would naturally produce the correct abundance today.

The WIMP miracle

The WIMP model supposes that as the temperature of the early Universe is larger than the mass of the particle m_χ, all particles are in thermal equilibrium. This is maintained by $\chi\chi$ pair annihilation into standard model particles, and vice versa.

Later, when the Universe cooled to temperatures below m_χ, the number density of dark matter particle is Boltzmann suppressed, dropping exponentially. This means that the number of WIMPs would drop to zero. However, besides cooling, the Universe is also expanding. Once the dark matter particles were so dilute that the annihilation rate became smaller than the expansion rate, they fell out of equilibrium, and the WIMP number per co-moving volume remained constant. This is known as the freeze-out or the chemical decoupling [18, 22]. The WIMP relic density seen today would be approximately [8]:

$$\Omega_\chi h^2 \approx \frac{3\times10^{-27}\text{cm}^3\text{s}^{-1}}{\langle\sigma_{ann}v\rangle}, \tag{1.8}$$

where σ_{ann} is the WIMP annihilation cross-section, and v is the relative velocity of the annihilating particles.

For weak cross-sections, this gives the right order of magnitude for the dark matter density, which is sometimes referred to as the WIMP miracle.

Another important implication from the WIMP miracle is that χ must have non-zero coupling with standard model particles. This suggests how WIMPs could be found. The products of $\chi\chi$ annihilation can be detected, providing means of indirect detection. Dark matter particles should also scatter off normal matter, leaving energy deposited inside the target that can be directly detected. Theoretically, dark matter can also be produced at particle colliders, which could be another way of detecting dark matter. Details of WIMP detection, particularly direct detection, will be discussed in later sections (also see Figure 1.7).

WIMP and Physics beyond Standard Model

A further reason why WIMPs appear to be good dark matter candidates is that many particles in this category can solve more problems than just dark matter. Some actually come from processes of trying to solve other unrelated physics problems.

One example is the Lightest Supersymmetric Particle (LSP) from Supersymmetry (SUSY) models. SUSY is proposed to solve the hierarchy problem in particle physics. In this extension of the Standard Model (SM), every SM-particle has a supersymmetric partner, which differs in spin by 1/2 – a fermion's super-partner is a boson and a boson's super-partner is a fermion – thus doubling the number of particles in nature. It also brings in a new symmetry called R-parity. All standard model particles have an R-parity of +1 while SUSY particles have an R-parity of −1. SUSY particles heavier than the LSP are short-lived and will decay to the LSP eventually. Assuming conservation of R-parity, the LSP cannot decay further into Standard Model particles and therefore is stable. The most promising candidate for the LSP and also a very good WIMP candidate is the neutralino, which is a mixture of the super-partners of the Higgs, photon, and Z [23]. It is electrically neutral, as required for a dark matter candidate. It is also its own anti-particle, which means neutralinos can annihilate with themselves, giving the correct dark matter abundance today. Examples of expected neutralino-quark coupling are shown in Figure 1.6.

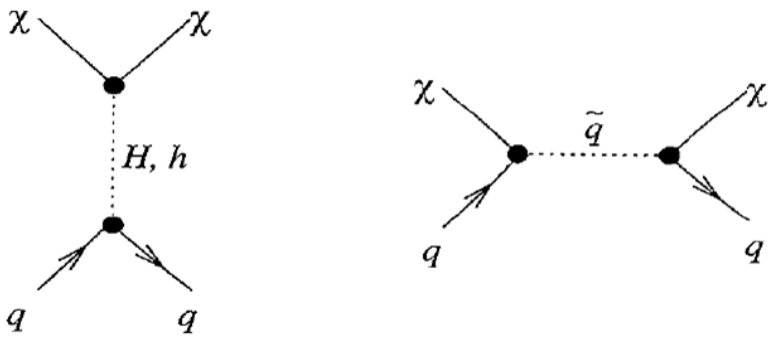


Figure 1.6: Feynman diagrams contributing to neutralino-quark scalar elastic-scattering (spin-independent). Diagrams taken from [26] (with permission from Elsevier).

There are many other possibilities for WIMPs from theories beyond the Standard Model, including the lightest Kaluza-Klein particles (LKP), which come from extra-dimension models, branons in large extra dimension theories, T-odd particles in little Higgs theories, etc. [22] It seems that, similarly to SUSY, many models producing potential dark matter particles have discrete symmetries between standard model particles and newly introduced ones. Thus the lightest particle in the new particle sector is stable, and can only be pair-annihilated. If it is also electrically neutral, then it could be a candidate for dark matter [23].

1.4 WIMP Searches

With a rather large set of theoretical models available, it is necessary to experimentally detect dark matter to determine its exact nature. Being the most plausible dark matter candidate, detecting WIMPs is the main aim of many experiments around the world. As mentioned in Section 1.3.2, these experiments are searching for WIMPs in three different ways (Figure 1.7).

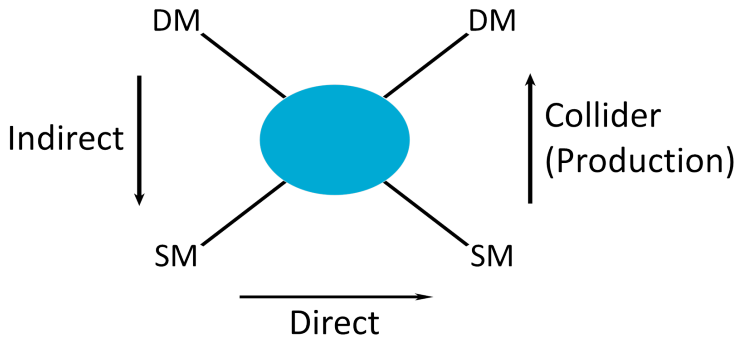


Figure 1.7: Three methods of searching for WIMPs. DM and SM denote WIMPs and standard model particles respectively. Dark matter particles interact with ordinary matter particles weakly, via a variety of possible mechanisms symbolised by the circle in the middle. The three arrows symbolise the direction of time.

This section will focus on the direct detection method, which is the main interest of this thesis, while briefly introducing the principles of the other two approaches as well.

1.4.1 Direct Detection

From the previous discussion, WIMPs have weak but non-zero coupling to baryonic matter. As a result, when WIMPs pass through a target, a small fraction of them could elastically scatter off the nuclei, depositing a potentially measureable recoil energy in the target. The main aim of direct detection experiments is then detecting this deposited recoil energy.

Basic Event Rate of WIMP Scattering

The event rate per unit mass of a detector target with atomic mass A and WIMP-nucleus elastic scattering cross-section σ_N is given by:

$$R = \frac{N_A}{A} \cdot \sigma_N \cdot \frac{\rho_0}{m_\chi} \cdot \langle v \rangle = \frac{N_A}{A} \cdot \sigma_N \cdot \frac{\rho_0}{m_\chi} \int v \frac{f(v, v_E)}{k} d^3v \,, \tag{1.9}$$

where k is a normalisation constant

$$k = \int_0^{2\pi} d\varphi \int_{-1}^{1} d(cos\theta) \int_0^{v_{esc}} f(v, v_E) v^2 dv \,. \tag{1.10}$$

Here, N_A is the Avogadro constant, ρ_0 is the local WIMP density, m_χ is the WIMP mass, v is the velocity onto the target, v_E is the Earth velocity relative to the dark matter distribution, v_{esc} is the local Galactic escape velocity and $f(v, v_E)$ is the WIMP velocity distribution.

There is actually a debate about what is a more realistic velocity distribution model. Conventionally, it is assumed to be a Maxwellian distribution:

$$f(v, v_E) = \exp\left[-\frac{(v + v_E)^2}{{v_0}^2} \right], \tag{1.11}$$

where v_0 is the local circular speed ~220 km/s.

For simplicity, it could be assumed that the Earth velocity and the escape velocity are zero and infinite respectively. Define R_0 as the event rate per unit mass for this condition [24], then

$$k = k_0 = (\pi {v_0}^2)^{3/2} \tag{1.12}$$

and

$$R_0 = \frac{2}{\sqrt{\pi}} \cdot \frac{N_A}{A} \cdot \sigma_N \cdot \frac{\rho_0}{m_\chi} \cdot v_0 \,. \tag{1.13}$$

Therefore,

$$dR = R_0 \cdot \frac{k_0}{k} \cdot \frac{1}{2\pi {v_0}^4} \cdot vf(v, v_E) d^3v \,. \tag{1.14}$$

The WIMP-nucleus scattering is treated in the non-relativistic limit, so the recoil energy can be calculated in terms of the scattering angle in the centre of mass frame θ^*:

$$E_r = \frac{\mu^2 v^2}{m_N} (1 - cos\,\theta^*) \,, \tag{1.15}$$

where m_N is the nucleus mass and $\mu = m_\chi m_N / (m_\chi + m_N)$ is the WIMP-nucleus reduced mass.

Assuming the scattering is uniform in $cos\theta^*$, then the recoil energy E_r is uniformly distributed over the range $0 \leq E_r \leq (2\mu^2 v^2)/m_N$.

Define E_0 as the kinetic energy of a WIMP with a velocity of v_0, $E_0 = \frac{1}{2} m_\chi {v_0}^2$, then the differential event rate is:

$$\begin{aligned} \frac{dR}{dE_r} &= \int_{E_{min}}^{E_{max}} \frac{m_N}{2\mu^2 v^2} dR(E) \\ &= \int_{E_{min}}^{E_{max}} \frac{1}{E_0 r} \frac{{v_0}^2}{v^2} dR(E) \\ &= \frac{1}{E_0 r} \int_{v_{min}}^{v_{max}} \frac{{v_0}^2}{v^2} dR(v) \,, \end{aligned} \tag{1.16}$$

where $r = 4\mu^2 / m_\chi m_N$.

The lower limit is given by the minimum WIMP velocity that can produce a recoil energy E_r above detection threshold. From Equation (1.15), $v_{min} = \sqrt{E_r m_N / 2\mu^2}$. The maximum velocity is defined by the escape velocity v_{esc}. For $v_E = 0$, $v_{esc} = \infty$,

$$\frac{dR(0,\infty)}{dE_r} = \frac{R_0}{E_0 r} e^{-E_r/E_0 r} . \tag{1.17}$$

The exponential distribution means that lowering the energy threshold of detectors will significantly increase the detected event rate, which is crucial in WIMP direct detection experiments.

The expression can be made more realistic by considering non-zero Earth velocity and finite escape velocity. The differential event rate is then given by [24]:

$$\frac{dR(v_E, v_{esc})}{dE_r} = \frac{k_0}{k_1}\left[\frac{dR(v_E,\infty)}{dE_r} - \frac{R_0}{E_0 r} e^{-{v_{esc}}^2/{v_0}^2}\right], \tag{1.18}$$

where

$$k_1 = k_0\left[erf\left(\frac{v_{esc}}{v_0}\right) - \frac{2}{\pi^{1/2}}\frac{v_{esc}}{v_0} e^{-{v_{esc}}^2/{v_0}^2}\right], \tag{1.19}$$

and

$$\frac{dR(v_E,\infty)}{dE_r} = \frac{R_0}{E_0 r}\frac{\pi^{1/2}}{4}\frac{v_0}{v_E}\left[erf\left(\frac{v_{min}+v_E}{v_0}\right) - erf\left(\frac{v_{min}-v_E}{v_0}\right)\right]. \tag{1.20}$$

The results of direct detection experiments will set limits on this differential event rate. Using the standard astrophysical assumptions on the WIMP distribution, only the WIMP mass m_χ and the WIMP-nucleus scattering cross-section σ_N remain unknown. This then allows a corresponding limit for σ to be calculated for each m_χ and eventually placing constrains on the dark matter parameter space in the absence of significant WIMP signals.

Nuclear Form Factor Correction

The previous calculation is based on the assumption of zero momentum transfer, which means that the momentum gained by the recoil nucleus $q = \sqrt{2m_N E_r}$ is near to zero. However, when q increases, the wavelength h/q becomes comparable to the nuclear radius, and effects caused by nuclear structure become more significant. As a result, the effective cross-section will be suppressed [25]. This is represented by a form factor F, so that the cross-section then can be expressed as [24]:

$$\sigma(qr_n) = \sigma_N F^2(qr_n) \,, \tag{1.21}$$

where r_n is the effective nuclear radius and σ_N is the previously defined cross-section at zero momentum transfer.

A commonly used approximation is

$$F^2(qr_n) = e^{-\alpha(qr_n)^2} \,. \tag{1.22}$$

For small qr_n, this could be sufficient. More exact computations for the spin-independent and spin-dependent cases can be found in [24].

Scattering Cross-sections

The total WIMP-nucleus scattering cross-section at zero momentum transfer can be written as [26]

$$\sigma_N = 4{G_F}^2 \mu^2 C_N \,. \tag{1.23}$$

Here, C_N is a dimensionless number, defined as the enhancement factor, which encodes particle physics model information. G_F is the Fermi coupling constant.

The total cross-section contains contributions from the spin-independent (SI) term, which comes from the scalar part of the interaction and spin-dependent (SD) term, which comes from the axial-vector part of the interaction.

For the purpose of comparing limits from experiments using different targets as well as comparing theoretical predictions to experimental results, the WIMP-nucleus cross-section can be expressed in terms of the WIMP-nucleon cross-sections σ_p and σ_n.

In the SI case [26],

$$C_N^{SI} = \frac{1}{\pi {G_F}^2}[Zf_p + (A - Z)f_n]^2 , \tag{1.24}$$

where f_p and f_n are the couplings of WIMPs to protons and neutrons respectively. In most models, WIMPs are Majorana particles (which are their own anti-particles) so that $f_p \simeq f_n$. Then $C_N^{SI}/C_p^{SI} \simeq C_N^{SI}/C_n^{SI} \simeq A^2$. From Equation (1.23),

$$\sigma_p^{SI} = \sigma_N^{SI} \frac{{\mu_p}^2}{\mu^2} \frac{1}{A^2}. \tag{1.25}$$

In the SD case [26],

$$C_N^{SD} = \frac{8}{\pi}(a_p\langle S_p\rangle + a_n\langle S_n\rangle)^2 \frac{J+1}{J}, \tag{1.26}$$

where a_p and a_n are WIMP-proton and WIMP-neutron coupling respectively; $\langle S_p \rangle$ and $\langle S_n \rangle$ are the expectation values of the proton and neutron spins in the nucleus respectively; and J is the total nuclear spin.

As C_N^{SD} contains contributions from both proton and neutron terms, converting experimentally deduced WIMP-nucleus cross-section to WIMP-proton cross-section in the SD case is not as straightforward as the SI case. An alternative method for comparisons is proposed in [27].

Generally, with increasing A, the SI term will increase relative to the SD term and is likely to dominate for $A \gtrsim 30$ [24].

1.4.2 Direct Detection Techniques

From the previous discussion, a low energy threshold and a large target mass are essential to efficiently detect a WIMP-induced spectrum. For a WIMP of mass in the

range of 10 – 1000 GeV and a velocity of about 220 km/s, the recoil energy deposited due to elastic scattering of WIMPs from nuclei will be in the range of 1 – 100 keV. This recoil energy will then transform into different detectable channels. Most of this energy will dissipate into the phonon system, generating phonon / heat signal. A portion of the recoil energy can also generate electron-hole pairs, which can be collected under an applied electrical field, providing the ionisation signal. In addition, part of the deposited energy can excite the target atoms – scintillation signal can then be generated during relaxation. Detailed mechanisms regarding specific targets can be found in literature.

Solid-state Cryogenic Detectors

One of the dark matter direct detection techniques uses cryogenic detectors operated at sub-Kelvin temperatures. As the heat capacity of a dielectric crystal has a $\sim T^3$ dependence, at cryogenic temperatures, a very small energy deposition can still significantly change the absorber's temperature. This property makes it possible to have detectors with excellent energy resolution and low threshold. It is also very important for dark matter detectors to be able to discriminate between the nuclear recoil events and the overwhelming electromagnetic background. Neutrons and WIMPs will interact with the target nucleus and deposit energy via nuclear recoils, while electrons and photons will deposit energy via electron recoils. Because of the very different energy deposition densities of nuclear recoils and electron recoils, the rejection of electron and photon background is usually done by simultaneously measuring the rise of temperature as well as a different channel of signal from one interaction and comparing the ratio of these two signals. The EDELWEISS, CDMS / SuperCDMS and CRESST experiments are examples implementing this kind of technique. In the former two experiments, heat and ionisation signals are measured

using high purity germanium crystals as detector targets. In CRESST, a different type of target, calcium tungstate crystals, is used and it measures heat and scintillation signals instead. Both CRESST (CRESST-II) and CDMS (CDMS II Si) claimed to see an excess of signals implying light WIMPs with a mass in the 6 – 30 GeV range at a certain stage [28, 29]. However, this is in tension with many other results (Figure 1.8). Also, these low-mass regions have later been disfavoured by reanalysis of data or improvements of these experiments [30, 31, 32].

Liquid Noble Gas Detectors

Another important dark matter direct detection technique uses liquid noble gases, mainly xenon and argon, as detector targets. Liquid xenon (LXe) and liquid argon (LAr) are good scintillators and ionisers in response to the passage of radiation. The possibility of building a large, homogeneous, self-shielding detector that is relatively easy to scale-up gives liquid noble gas detectors a big competitive advantage at the higher WIMP mass region. There are two main types of liquid noble gas detectors: two-phase and single-phase. For both types, the LXe or LAr target is surrounded by photomultiplier tubes (PMTs), which measures the scintillation signal. This is normally the main signal. In two-phase experiments, similarly to the cryogenic detectors mentioned above, another channel of signal can be measured for background rejection, which is normally ionisation for liquid noble gases. This is done by implementing a time projection chamber (TPC). The TPC contains both liquid and gas phase of LXe or LAr and an axial electrical field is applied. When the electrons drifted to the phase boundary, they will produce a second electroluminescence photon signal proportional to the total charge, thus providing a second channel. ZEPLIN [33], LUX [34] (and the joint force next-generation LUX-ZEPLIN [35]), XENON [36], and DarkSide [37] all use this kind of detection

principle. In single-phase experiments, the background discrimination is done by studying the pulse shape only using the primary scintillation signal, such as XMASS [38] and DEAP [39].

Other Techniques

Besides these two, there are also other techniques such as superheated liquid detectors used by the PICASSO [40] and COUPP [41] (and now a joint effort PICO [42]) experiments, scintillating crystals used by the DAMA/LIBRA experiment [43], etc. A more comprehensive review can be found in many books and articles like [8] and [44].

The current spin-independent limits placed by selected dark matter direct detection experiments are shown in Figure 1.8.

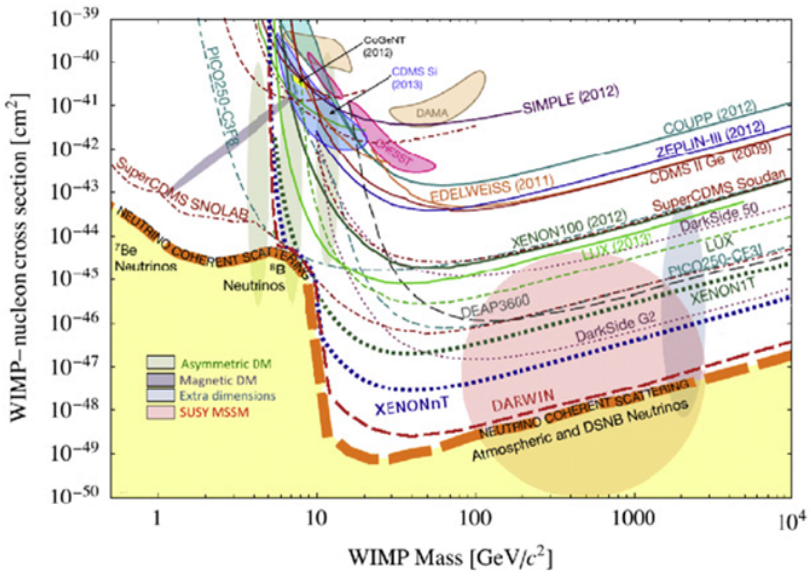


Figure 1.8: Exclusion plot showing current spin-independent limits from selected dark matter direct detection experiments, and projections for selected dark matter experiments that are expected to operate over the next decade. An approximate band where neutrino coherent scattering will begin to limit the experiment sensitivity is also shown. A suite of theoretical model predictions is indicated by the shaded regions. The plot is taken from [45] (with permission from Elsevier) (adapted from [46]).

1.4.3 Indirect Detection

As introduced before, dark matter pair annihilation is greatly suppressed after freeze-out. However, it still continues to happen even though its impact on the dark matter relic density is negligible [22]. Therefore, another approach to WIMP searches is by indirect detection, which involves looking for the annihilation products of WIMP pairs. These detectable products could be neutrinos, gamma rays, positrons, and other anti-particles.

When WIMPs pass through celestial objects, they could be slowed down and become gravitationally bound in these objects due to interactions with atomic matter. This then results in higher densities of WIMPs and increases the probability of annihilation in celestial objects like the Galactic Centre, the Sun or the Earth. Although most of the WIMP annihilation products are absorbed immediately, energetic neutrinos could escape and be detected by neutrino detectors on Earth such as Super-Kamiokande (or Super-K) [47], Antarctic Muon And Neutrino Detector Array (AMANDA), AMANDA's successor IceCube [48], and so on. The mean energy of these neutrinos ranges from ~10 GeV to ~1 TeV [22], separating them from other solar neutrinos. WIMP signals from such neutrino search experiments would be excesses of neutrinos from the direction of the Sun, a nearby and identifiable source, over the atmospheric neutrino background [49]. Similarly to direct detection, the null results then give limits on the cross-section for interactions of dark matter particles with ordinary matter.

Gamma rays created in WIMP annihilations can also be a detectable signature [50]. A continuous spectrum of gamma rays through annihilation into intermediate states, and monoenergetic line features from dark matter directly annihilating into $\gamma\gamma$ and γZ are expected. The size of signals should be most prominent in the direction of the

Galactic Centre [18]. Dwarf galaxies are also promising targets due to their reduced astrophysical background. The Large Area Telescope (LAT) on the Fermi Gamma Ray Space Telescope is one of the experiments looking for this kind of signals. Its recent result combining LAT observations of 25 dwarf galaxies sets some of the most stringent constrains for the dark matter annihilation cross-section [51].

Some discrepancies between expectation and data detected by the Payload for Antimatter Matter Exploration and Light-nuclei Astrophysics (PAMELA) and the Alpha Magnetic Spectrometer (AMS) experiments could also give hints to the detection of dark matter. Both experiments measure the antimatter component of the cosmic radiation. Generally the spectrum of antimatter relative to matter is expected to fall at higher energies [52]. However, the positron fraction, which is defined as the ratio of the positron flux to the combined flux of positrons and electrons, measured by PAMELA deviates obviously from this expectation at energies above ~10 GeV [53]. This is also confirmed by AMS [54], as shown in Figure 1.9. The latest AMS result also showed a new behaviour of the positron fraction at high energy: above ~200 GeV the positron fraction is no longer increasing with energy.

There are several possible explanations for the data, and one of them would be that this excess is due to dark matter annihilation. However, the flux required to account for this discrepancy would be much larger than expected for generic WIMPs [22]. Although some solutions are proposed, it is too early to interpret the unknown contribution as evidence of dark matter. While more data from AMS could provide more clarity, better understanding of astrophysical background will be necessary to determine whether it is useful for detecting dark matter.

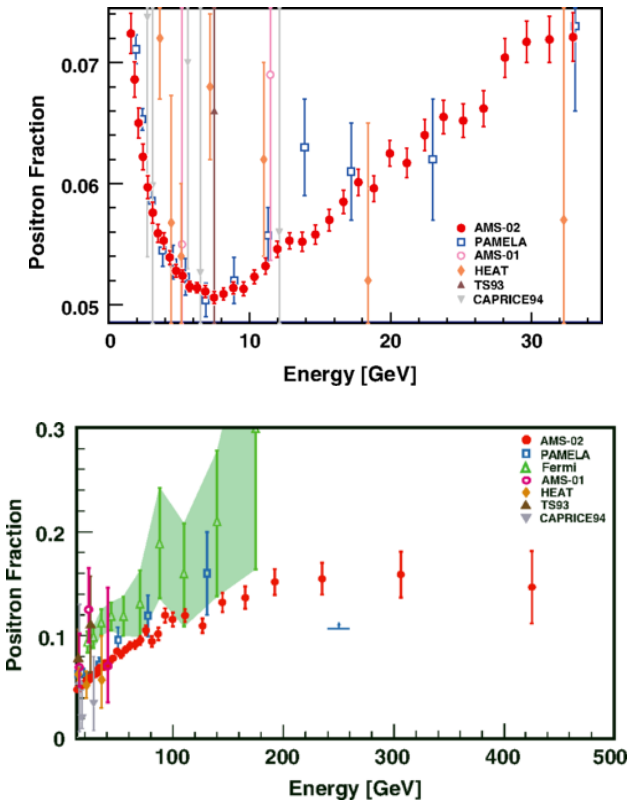


Figure 1.9: The positron fraction measured by AMS: (top) from 1 to 35 GeV; (bottom) above 10 GeV, where it begins to increase. Results from other experiments like PAMELA are also included for comparison. Plots taken from [54] (with permission from American Physical Society).

1.4.4 Detection in Particle Colliders

Complementary to indirect and direct detections, dark matter particles could in principle be produced and studied in modern high energy particle colliders, given the proposed mass range of WIMPs and their interactions with ordinary particles. This approach can be very efficient in probing the very-low-mass WIMP region, while the other experiments are more sensitive at higher mass since the cross-section at collider falls rapidly with mass. These different strategies also provide information of different aspects regarding the nature of dark matter. Therefore, a combination of them can be much more informative than any one approach alone, and preferably, any discovery of dark matter in one approach should be confirmed with the others to be convincing enough.

If produced, WIMPs will traverse layers of detectors and escape without leaving any trace as they do not interact with atomic matter electromagnetically or strongly. Therefore, the searches focus on events that produce pairs of dark matter particles, which then corresponds to a large missing transverse energy / momentum, and jets of standard model particles or photons. Such searches have been conducted in the Large Electron-Positron (LEP) collider [55, 56], the Tevatron [57], and the current Large Hadron Collider (LHC) [58]. So far, there is no excess signal above the standard model background indicating dark matter particles. Like the previous two detection approaches, this then gives more constraints on dark matter model parameters. As an example, Figure 1.10 shows the 90% CL limits on WIMP-nucleon scattering cross-sections deduced from ATLAS results.

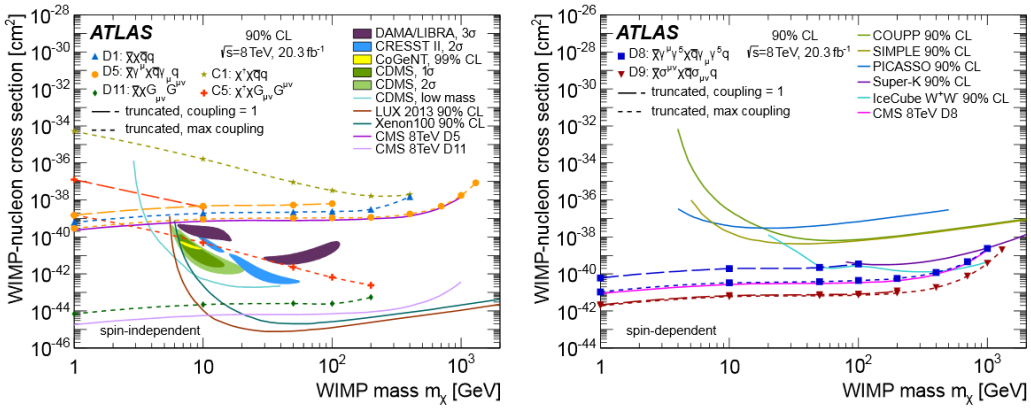


Figure 1.10: Inferred 90% C.L. limits on spin-independent (left) and spin-dependent (right) WIMP-nucleon scattering cross-sections as a function of WIMP mass m_χ from ATLAS detector at LHC. Some direct and indirect detection results are also shown for comparison. Plot taken from [59] **(distributed under the terms of the Creative Commons Attribution 4.0 International License).**

2 The EDELWEISS and EURECA Experiment

Within all the direct dark matter detection efforts around the world, there are several of them conducted at cryogenic temperature. As described in the last chapter, the low energy threshold makes cryogenics detectors excellent for detecting dark matter events that are normally with very low energies. These detectors can also have very good energy resolution and event-by-event background discrimination ability.

The EDELWEISS (Expérience pour DEtecter Les Wimps En SIte Souterrain) experiment is one of these direct WIMP search cryogenic experiments. It aims to detect WIMP interactions using an array of cryogenic germanium detectors.

In the future, the EDELWEISS and CRESST collaborations, as well as other European groups will team up to build a tonne-scale next generation experiment – EURECA (European Underground Rare Event Calorimeter Array).

This chapter will start with describing the experiment setup and detection principle of the EDELWEISS experiment, especially the current EDELWEISS-III stage. Then results of the recent concluded EDELWEISS-II stage will be presented. Further, the initial design of the EURECA experiment will be briefly introduced here as well.

2.1 The EDELWEISS Experiment

The EDELWEISS experiment has been trying to detect WIMP signals with progressively increased sensitivities. The ultra-pure germanium phonon-ionisation detectors are equipped with neutron transmutation doped germanium (NTD-Ge) heat sensors for detecting the heat signal. Simultaneously, the ionisation signals are

detected by the aluminium electrodes covering the germanium crystals. More details will be introduced in Section 2.1.2. The very first stage of EDELWEISS started in 2000 and achieved an exposure of 62 kg·d [60]. The EDELWEISS-II stage following it was conducted in 2009 and 2010, using an array of ten 400 g detectors. A total effective exposure of 384 kg·d has been achieved [68].

The experiment has now been upgraded to the EDELWEISS-III stage, aiming at an even higher sensitivity level and a further suppressed background.

2.1.1 Radioactive Background Sources and EDELWEISS Shielding Setup

The sensitivity level EDELWEISS-III aims for is at the order of 10^{-9} pb (also see [61, 62, 70]), which corresponds to an event rate of 10^{-4} evts/kg/day. Thus, achieving the lowest possible background is mandatory.

By running the experiment in a deep underground laboratory, background induced by cosmic rays can be significantly suppressed. For EDELWEISS, the detectors are operated in the low-radioactivity environment of the Laboratoire Souterrain de Modane (LSM), which is an underground laboratory with an average rock overburden of 4800 metres water equivalent. The muon flux is attenuated by six orders of magnitude compared to sea level, down to ~5μ/m^2/d, by the rock [63].

Alpha particles, electrons, gamma radiation, and neutrons all can be part of the radioactive background. Among them, alphas and electrons have a very short range but gamma radiation and neutrons can affect the background from far away. Fortunately, gamma rays generate electron recoils in detectors, which can be largely discriminated. However, neutron-induced nuclear recoils can give the same signal as what would be expected from WIMPs.

So besides going deep underground, proper shielding, careful design of detectors and strict screening of materials used in the experiment are all crucial to reaching the sensitivity level.

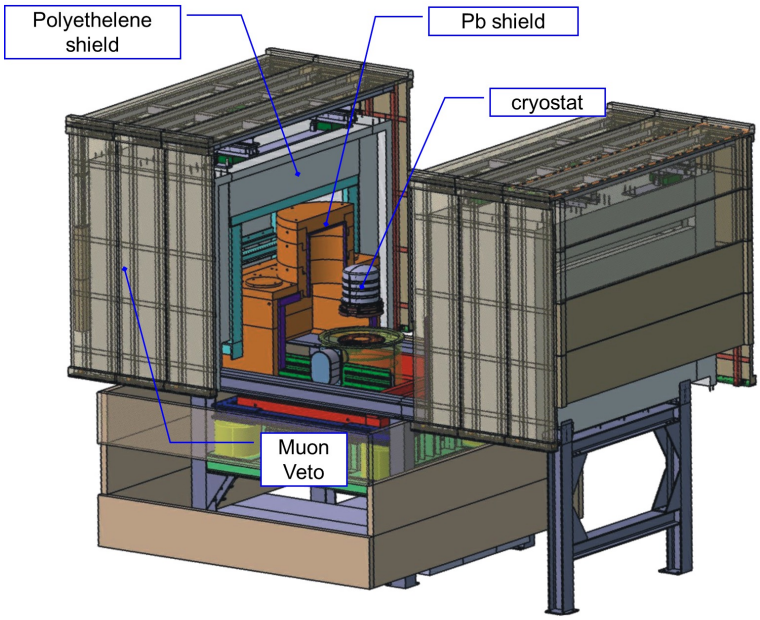


Figure 2.1: The EDELWEISS-III experiment setup.

In the current EDELWEISS-III phase, the copper cryostat is shielded by a 100 m^2 plastic scintillator muon veto system to actively tag muons, 20 cm of lead to shield gamma radiation and 50 cm of polyethylene to shield neutrons as shown in Figure 2.1 [63]. Extra polyethylene (~10 cm) and Roman lead (~15 cm) shielding is added inside the cryostat below the detectors.

2.1.2 Cryogenic Germanium Detectors

In the current EDELWEISS-III phase, an array of 800 g Full InterDigit (FID) germanium detectors (as shown in Figure 2.2) is being used for the WIMP search.

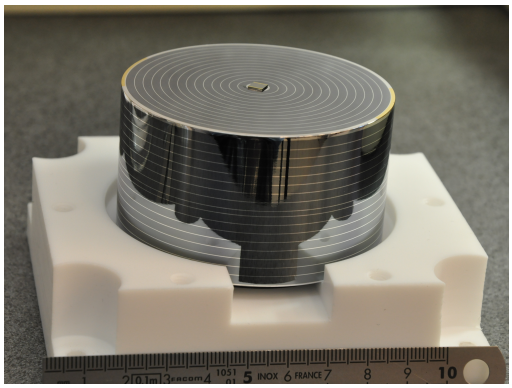


Figure 2.2: High purity germanium crystal (height: 4 cm) with deposited electrodes and NTD-Ge sensors in EDELWEISS-III.

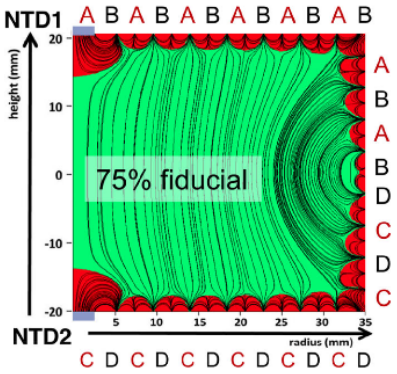


Figure 2.3: Cross-section of FID detectors, showing electrode scheme. B and D are fiducial electrodes; A and C are veto electrodes [64] (with permission from Springer). Details are explained in text.

FID Detector Design

For the detectors' primary heat channel, two NTD-Ge heat sensors are glued onto the top and bottom surfaces of each crystal (one of them is visible in Figure 2.2). The sensor's resistance increases exponentially with decreasing temperature, making it a very sensitive thermometer at milli-Kelvin temperatures. The NTD-Ge sensors used in EDELWEISS are operated at ~18 mK and detect a rise of temperature around a few micro-Kelvins induced by the energy deposition from a particle interaction. Details of this type of sensor will be discussed in Chapter 5.

As mentioned previously, the FID detectors also have an ionisation channel. Measuring phonon and ionisation signals simultaneously allows detection and localisation of scattering events within the crystal and provides a powerful discrimination between nuclear recoils and the background of electron recoils due to their different ionisation yields (see Figure 2.4 and Figure 2.5). The ionisation signals are collected by the aluminium electrodes deposited onto the crystals, covering all the surfaces as shown in Figure 2.2.

One important thing to be noted is that this discrimination mechanism can be applied to events that happened in the bulk of the target crystal, but the ionisation yield is distorted for surface events. EDELWEISS has adopted an interleaved electrode design to address this problem [65]. The electrode scheme and the corresponding electrical field in the FID detectors are shown in Figure 2.3.

The electrodes are arranged as concentric rings. Fiducial electrode rings B and D are biased at ± 4 V and generate a vertical electrical field inside the bulk of detector. Interleaved with B and D, the veto electrode rings A and C are biased at ∓ 1.5 V. They produce a field near and parallel to the surfaces. With such a design, when there is an event, if fiducial electrodes B and D collect opposite and equal charges, while no signal shows on veto electrodes A and C, then it can be identified as a bulk event. On the other hand, if a recoil event occurs approximately 1 mm from the surface (the field parallel to the surfaces, red region in Figure 2.3), charge signals will show on electrodes A and C, which consequently vetoes such event. Using this method, surface events can be discarded and a fiducial volume is defined within the detector.

This is named as the InterDigit design and has been used since EDELWEISS-II, which used ID detectors with electrodes only covering their top and bottom surfaces. For the latest detector version currently used in EDELWEISS-III, the detector's cylindrical outer surface is also covered with electrode rings in addition to the top and bottom flat surfaces. Thus they are called the Full InterDigit detectors, namely, FID. In this new FID design, comparing to the ID detectors, the fiducial volume fraction increases from the previous 40% to 75%, and the height of crystals increases from 2 cm to 4 cm. As a result, the absolute fiducial volume per detector increases from 160 g, as in EDELWEISS-II (ID400 detectors), to 600 g in EDELWEISS-III (FID800 detectors) now.

Electron Recoil Discrimination Performance

To test their rejection performance, two FID detectors are exposed to ^{210}Pb sources with the ^{210}Bi and ^{210}Po daughters, surrounding all surfaces. Both low and high energy betas, as well as 5.3MeV alphas and recoiled 100keV ^{206}Pb, are generated in the decay chain.

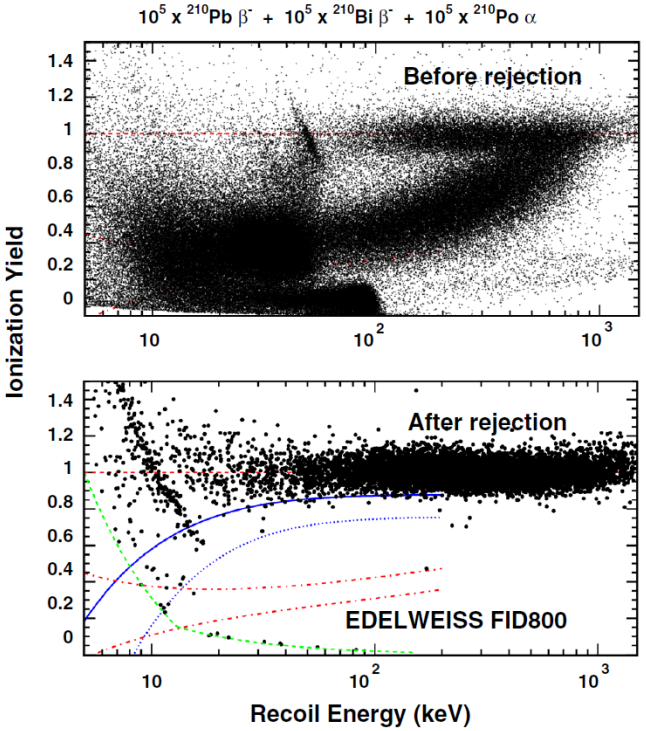


Figure 2.4: For an exposure to ^{210}Pb sources close to equilibrium with the ^{210}Bi and ^{210}Po daughters – (Top) Distribution of ionisation yield as a function of recoil energy observed in two FID detectors, before rejection; (Bottom) Same data after rejecting events without bulk event signature defined above. The red dot-dashed lines represent the band where 90% of all nuclear recoil events are expected. The full and dashed blue lines indicate the 90% and 99.99 % regions for gamma-rays, respectively, and the green dashed hyperbola shows the 2 keV ionization threshold cut. The ionisation yield is the ratio of ionisation signal to the recoil energy, normalised to 1 for electron recoil events. From [64] (with permission from Springer).

For an exposure of 10^5 alphas, which is already more than the number of expected alphas in a 2-year run with 40 FID detectors, the observed event distribution before rejection is shown in the top plot of Figure 2.4. After applying the fiducial cut defined previously, the bottom of Figure 2.4 shows only one event leak into the 90% nuclear recoil band. From this calibration, the rejection factor of FID detectors is determined as 4×10^{-5} (90% CL Poisson limit).

Data Acquisition for Ge detectors

The readout system of Ge detectors is composed of a cold electronics part with FET preamplifiers at the 100 K stage, a room temperature part with ADC "bolometer boxes" (BB) and a data routing system streaming the digitised signals to dedicated computers running the DAQ software, which filter data, make trigger decisions and write data to disks [66, 67].

For FID detectors, there are four ionisation channels for electrodes A, B, C, D and two NTD channels on each detector. The resistances of NTD sensors are measured by sending down modulated excitations while the ionisation pulses give step functions. All channels are read out by 16-bit ADCs at a sampling rate of 100 kHz.

2.1.3 Final Results of EDELWEISS-II

As the experiment has now been upgraded to EDELWEISS-III and is collecting data, the latest official WIMP-nucleon interaction limit results are those of the EDELWEISS-II stage. In EDELWEISS-II, the collaboration completed a WIMP search with ten 400 g ID detectors and achieved a total effective exposure of 384 kg·d. The potential background in the WIMP search region was also carefully calculated.

The final scatterplot is shown in Figure 2.5. Five WIMP candidates are observed and the estimated total neutron background does not contradict this observation. Given the small number of observed events, this gives no indication of WIMP signals. This result can be interpreted in terms of limits on different models. Due to the low statistics and uncertainties in the background estimation, the limits are calculated by considering all 5 events as nuclear recoil candidates. One of the interpretations most commonly adopted by the dark matter detection community is the limit on the cross-section of spin-independent interactions of WIMPs and nucleons. Based on the results

presented here, a cross-section of 4.4×10^{-8} pb is excluded at 90% CL for a WIMP mass of 85 GeV. More details can be found in [68].

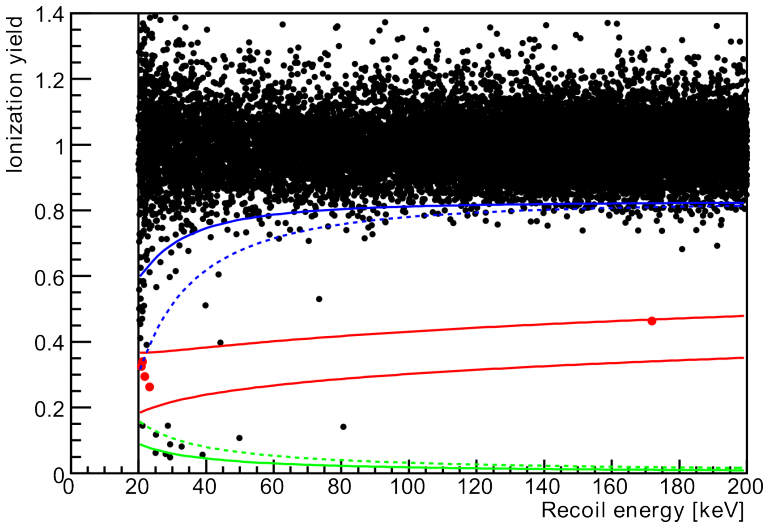


Figure 2.5: Final result of EDELWEISS-II: ionisation yield vs. recoil energy of fiducial events. The bold red lines represent the WIMP search region, which is defined by an ionisation yield inside the 90% acceptance band with recoil energies between 20 and 200 keV. Five observed nuclear recoil candidates are highlighted in red. The continuous and dashed blue lines show the average and worst one-sided 99.99% rejection limits for electron recoils respectively. The continuous and dashed green lines show the average and worst ionization thresholds respetively. Plot taken from [68] (available under the terms of the Creative Commons Attribution License).

The potential neutron background sources are considered as misidentified gamma-ray events, un-rejected surface events, and neutron scattering. The estimated background event contributions are listed in Table 2.1.

Source	**Number of Events**
Misidentified gamma-ray events in NR (nuclear recoil) band	< 0.9
Un-rejected surface events in NR band	< 0.3
Muon-induced neutrons (missed by muon veto)	< 0.7
Neutrons from cables and connectors	< 1.2
Neutrons from other components (walls, shielding, support, electronics, cryostat, crystal holders, electrodes, etc.)	< 1.9

Table 2.1: Estimation of EDELWEISS-II background events in the WIMP search region, using calibration data, radioactivity test results and simulations. Values taken from [63, 68, 69].

From the table we can see that neutron background induced by the cables and connectors used in EDELWEISS-II is already comparable to that contributed by all

the other components combined and greater than all the rest of contributions. Thus for EDELWEISS-III, to achieve better sensitivity with about 4 times more detectors to read-out and 10 times more effective exposure, there must be a better cabling solution, especially for the region closest to the detectors.

Motivated by this necessity, a new cold cabling system has been developed, produced and installed in EDELWEISS-III. This significant contribution is covered in this thesis in Chapter 3 and 4.

2.1.4 EDELWEISS-III Prospects

EDELWEISS-III plans to operate forty of the 800 g FID detectors introduced above. Thus the collaboration will be able to conduct a WIMP search with an array of 32 kg, or a fiducial mass of 24 kg, of germanium. A fiducial exposure of 3000 kg·d is possible in less than 6 months of running.

With improvements in electronics, cabling, cryogenics, and shielding, the current estimated background in EDELWEISS-III is compatible with the goal of obtaining an exposure of 10^4 kg·d with around one background event, which corresponds to the possibility of probing spin-independent WIMP-nucleon cross-section down to the 10^{-9} pb range within 2 years.

2.2 The EURECA Experiment

The next generation of direct dark matter searches, aiming to provide an increase in sensitivity by two orders of magnitude, will be needed to shed more light on the nature of dark matter. To achieve this goal, they will require a target mass at the tonne scale. Hence, the next step for EDELWEISS will be collaborating with other groups around Europe to combine their expertise in building the EURECA experiment – a facility that can house a target of up to 1000 kg mass.

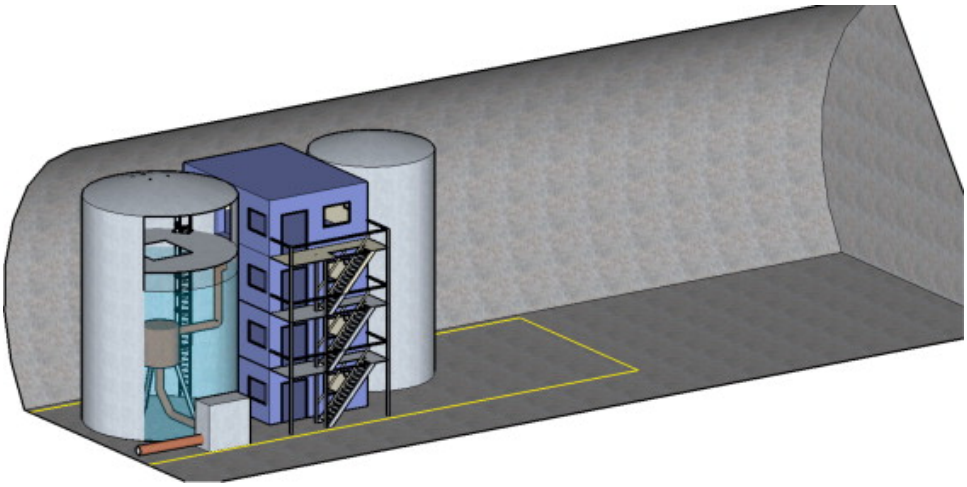


Figure 2.6: Schematic of current EURECA design within the 50m-long hall of the DOMUS extension: the cryostat is installed inside the main water tank (left). The cleanroom tower and water storage tank (right) are next to it. Taken from [70] (available under the terms of the Creative Commons Attribution License).

The conceptual design has been completed. As LSM is the deepest underground lab in Europe, the Fréjus site is the favoured site by the EURECA collaboration. It will be located in a future extension, the Deep Observatory for Multidisciplinary Underground Science (DOMUS), as it will be too large to fit in the current space.

There will be two stages for EURECA. The first phase will involve building the infrastructure, cryostat and shielding, as well as installing and operating a subset of detectors of 150 kg mass. This phase aims to achieve a sensitivity of 3×10^{-10} pb. The second phase will be completed by an addition of 850 kg of detectors and aim at 2×10^{-11} pb as the sensitivity level. Both stages will operate in a cryostat immersed in a dedicated water tank, with the water acting as a shielding layer, as shown in Figure 2.6.

The facility is designed to be able to hold different types of cryogenic detectors: high purity germanium detectors developed by the EDELWEISS collaboration, which are described above, and $CaWO_4$ scintillating bolometers developed by the CRESST collaboration. The $CaWO_4$ bolometer detects simultaneous phonon and scintillation signals and uses transition edge sensors.

Beyond European detectors, EURECA is also designed to host other types of similar cryogenic detectors, in particular, the germanium detectors developed by the SuperCDMS collaboration in the US. In this project, they aim to install 150 kg target mass that is the same as EURECA phase one. The germanium detector used by CDMS, the predecessor of SuperCDMS, is very similar to the ones used in EDELWEISS and has comparable data quality. Therefore, successful collaborative work between the two groups has already been pursued, and both groups can benefit from further cooperation.

The same type of cold cabling developed in this thesis for EDELWEISS-III is also proposed for EURECA.

3 Laminated Semi-Flexible Cabling System

As discussed in previous chapters, direct dark matter detection experiments, like EDELWEISS, impose a number of restrictions regarding their cabling system. In EDELWEISS-II, the cables and connectors used there are even identified as one of the major sources of neutron background in the experiment, which means any further effort aimed at better sensitivity for WIMP-nucleon interaction detection will require a new way of connecting the detectors to the front-end electronics.

Motivated by this necessity, this thesis is to a large part on developing a new cabling system for the low-temperature part of the EDELWEISS setup, which is right next to the detectors. In general, the cables need to be suitable for temperatures as low as 10mK with reliable connectors. They also should be low noise, contribute only a minimal material/space budget, and most importantly, not introduce much radioactive background from its own isotopes. Further, different parts of the system pose more specific requirements, which are not necessarily consistent with each other.

Taking these requirements into account, combined with realistic limits that could be achieved, the current design and shape of a laminate cabling system has been developed. Further, prototypes and final cables, equipping the EDELWEISS detectors, have been fabricated at Oxford University. Before delivering to EDELWEISS, early versions of prototypes were made to fit in the Oxford Instruments K400 dilution refrigerator. They were tested as a part of a prototype cryogenic detector module which is also developed at Oxford in the context of this thesis and will be discussed in Chapter 5 - 6.

In this chapter, the general cable construction and fabrication process are introduced. Then the most crucial aspects when designing the cabling system as well as their implications on various cable parameters are discussed. The final design, balancing different aspects, is described at the end of this chapter.

3.1 General Cable Construction and Fabrication Process

As mentioned before, there are many reasons why the current design is the way it is. Most of the physics aspects are presented by the experiment and consequently define the final design, which will be discussed in the following sections. Here, the discussion focuses mainly on the fabrication process and mechanical constraints.

The cables can be seen as an assembly composed of two parts: the cable part and the connector part. The fabrication of the cabling and the production of the connectors can be carried out concurrently, before fitting the connectors to the ends of the cables. These two items are explained separately in this section.

3.1.1 Laminated Cables

Based on the initial motivation of reducing neutron background in the experiment, the cable is constructed as a layered structure. This allows flexibility for changing material of certain layers to fit the radiopurity requirement and avoid potentially problematic chemical components.

Photolithography

The basic building block of this cabling system, signal tracks upon a polyimide substrate, is fabricated using a standard photolithographic process. This technique is widely used in the printed circuit board industry. At Oxford, this procedure is carried out at our Photofabrication Unit (PFU). Below is a brief description of how it is done.

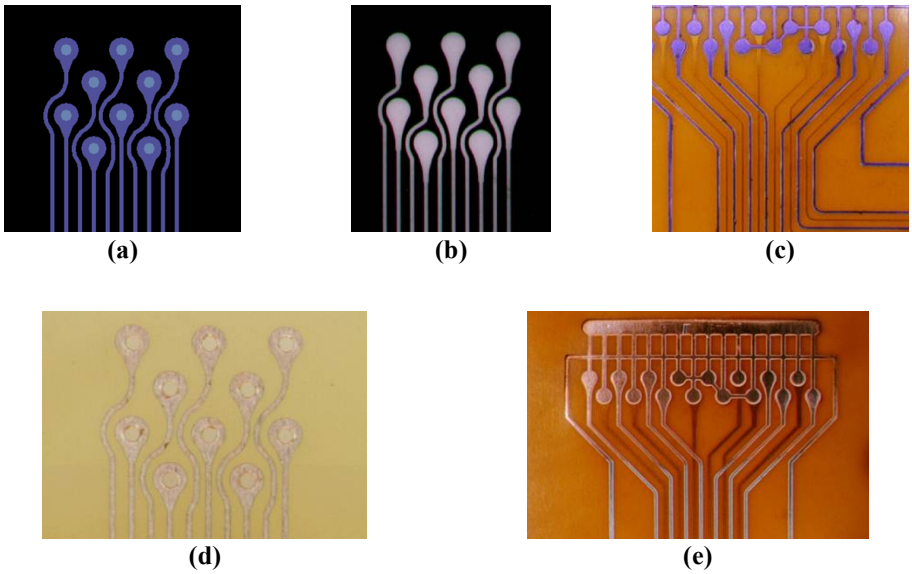


Figure 3.1: Selected stages in the photolithography process: (a) artwork, (b) photomask, (c) etched tracks with photoresist, (d) etched copper pads, (e) etched stainless steel tracks with copper plated pads.

First, the signal tracks are designed using a CAD software package. To transfer the pattern to the cable being produced, photomasks and layers of photoresist are required.

Photomask: The negative image of tracks is transferred onto a high-resolution polyester-based film with a dense photographic emulsion. This film is called phototool or photomask.

Photoresist: This is a type of materials that hardens when exposed to light (normally UV light). There are many different ways of applying photoresist onto the metal-polyimide base material. A dry lamination process and negative photoresist is used at the PFU.

Then the photomasks and metal-polyimide, laminated with photoresist, are aligned with each other and are, as a panel, exposed to UV light. Therefore, only the area with the desired pattern is exposed.

The unexposed photoresist is soluble in a special solution called “developer”. After using it to remove the photoresist on the unwanted area, the panel is sent

through an etching process where HCl and $FeCl_3$ are used. Subsequently, only the designed pattern protected by hardened photoresist remains on the polyimide substrate. The final step is applying a "photoresist stripper" solution to the panel to remove the remaining photoresist. Then the conductor part of this cabling system is ready.

Due to the need of keeping cable capacitance and heat conduction to a low value, which will be discussed in Section 3.2, the track width should be as small as possible. This can impose many challenges to the fabrication process, especially the etching.

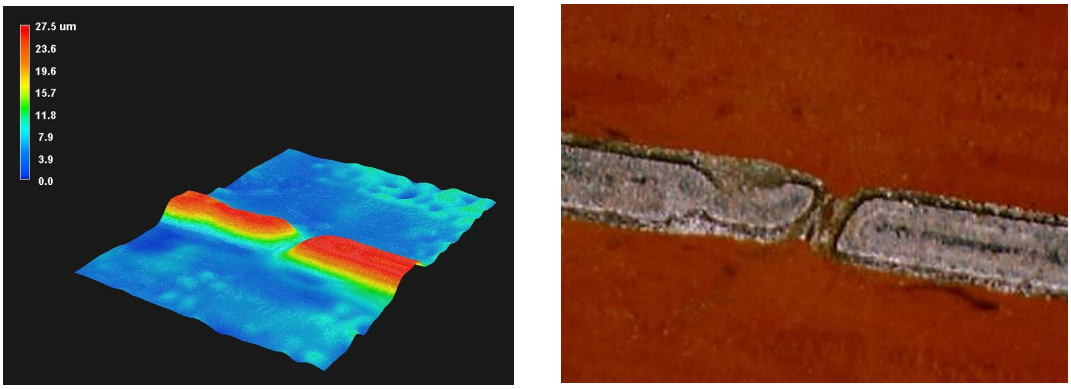


Figure 3.2: Example of a broken track after etching, under a microscope. The colour scale in the left figure indicates the height. The track shown here is designed as 125 µm wide (in artwork).

Any tiny breakage (Figure 3.2) in any of the metre-long tracks will result in an unusable, unrepairable cable. Faulty tracks due to breaks and short circuits can be caused by dust and dirt present while laminating photoresist onto the base material and exposing to UV light. Thus these processes require a very clean environment. The Oxford PFU runs a class 10,000 cleanroom and conducts the above-mentioned processes in it to minimise that risk. In addition, the panels are carefully inspected under a microscope to further increase the yield of good cables. If there are breaks or shorting of the remaining photoresist pattern detected, this step introduces an opportunity of repairing the cable before the etching step.

Copper Plating

Stainless steel cables (needed to bridge different temperature levels) require an additional step: the pads need to be copper plated for soldering the connectors.

It is possible to solder directly to stainless steel, but that requires aggressive flux and is strongly discouraged in the delicate environment of a dilution refrigerator (risk of latent leaks through slow corrosion). Experience shows this type of flux could cause the tracks to be slowly corroded or compromise the insulation between tracks. It is thus best avoided through using copper plating instead.

The application method used is brush electroplating, a process in which the pads are plated using a brush saturated with plating solution. The brush, a metal conductor wrapped with cloth holding the solution, and the tracks are connected to the opposite potential electrodes during plating. The brush is moved continually against the pads to achieve an evenly plated surface.

Direct application of copper would result in immersion deposit and poor adhesion. Thus, in addition to the normal pre-cleaning process, a nickel layer is also pre-plated to improve the quality of adhesion of the copper plating [71].

Shielding Coverlay

The tracks we obtained after etching are fragile, and sensitive to external noises. Also, the flexible cable will easily vibrate inside the cryostat and introduce extra noise to the signal.

Hence, two conducting layers are laminated on either side of the cable to protect the exposed tracks and to shield them against external interference. Further, this shielding provides mechanical strength to reduce vibration. Only the pads' areas for the connectors are left exposed.

Adding in these two shielding planes also means that the cable layer construction needs to be carefully designed to ensure minimal cable capacitance. Details will be discussed in Section 3.3. Its effect on fabrication is that extra dielectric layers are probably needed between the layer with tracks and the shielding layers to reduce the capacitance.

It has been noticed in earlier prototypes that if the thin bare tracks within those pad areas are exposed, especially for copper cables, they can be potentially vulnerable during soldering or later manipulation. Additionally, polyimide in the chosen metal-polyimide laminates can be quite fragile. In order to achieve maximum coverage so that signal tracks are better protected, the first dielectric cover-layers on the top and the bottom are extended to the whole cable and drilled to only expose the pads for assembling connectors.

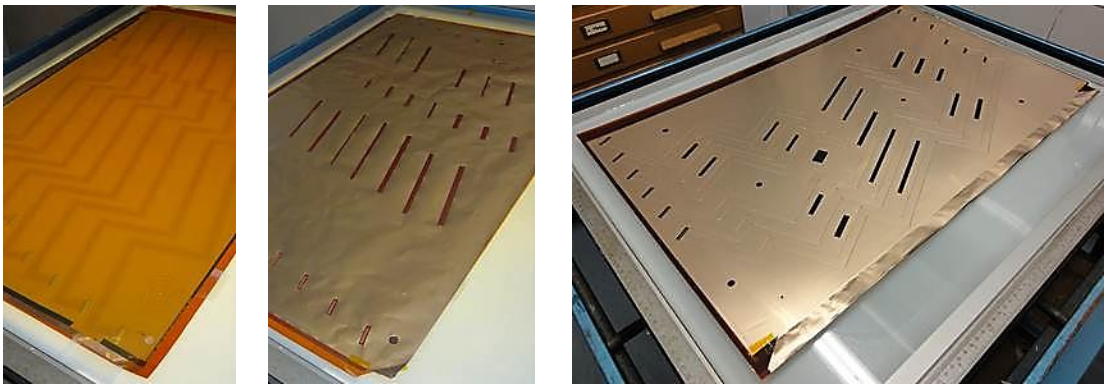


Figure 3.3: Selected steps of lamination. Tracks with first layer of dielectric (left); all layers aligned and ready for lamination (middle); pressed panel cut by a CNC cutting machine (right).

To increase the efficiency of production, several cables are arranged on one panel, being etched and laminated at the same time. After the lamination, a CNC cutting machine is used for routing the contours of individual cables.

After that is done, the body of the cable is basically finished.

3.1.2 Low-Radioactive Connectors

Another important part is the connector fitted onto this cabling system. Radioactivity test results of some commercially available connector options show that their levels of radioactive isotopes they contained are too high (details in Section 3.2). Especially the dyed plastic used in these connectors is suspected to be the main reason.

Therefore, the connectors used in our cabling system are designed and assembled in-house, with individual metal conductors and low radioactivity plastic bodies that provide mechanical stability. Details of material selection will be discussed in the following sections.

The individual metal conductors are chosen from the Mill-Max series, which is also used by the CDMS experiment [72]. Realistically, there is a limit for how radiopure the metal conductors can be. Therefore, keeping the material budget as small as possible can further ensure low radioactivity background. For that reason, the pins and receptacles chosen are the smallest options available that can still provide enough mechanical robustness to meet the experiment's needs – 3121 solder mount PCB pins and 2086 receptacles with a standard tail for the current design (see Figure 3.4).

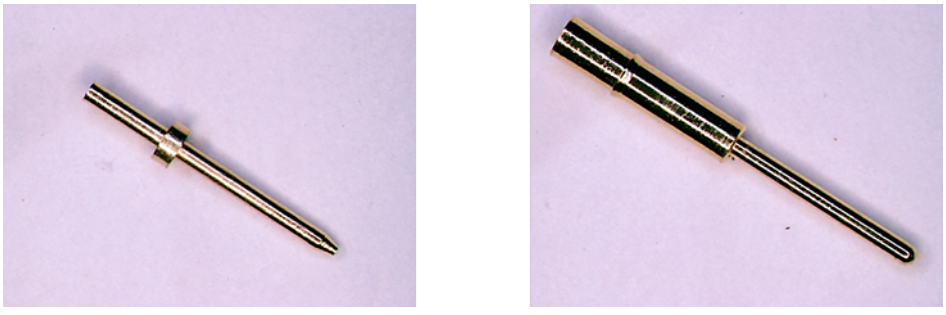


Figure 3.4: Mill-Max all metal individual conductors: (left) 3121 solder mount PCB pin; (right) 2086 receptacle with a standard tail.

The CAD software Autodesk Inventor is used for designing the connector bodies, which are then made in the Oxford Mechanical Workshop.

One of the critical points is where most of the shielding cover layers end to expose the pads for soldering. Because of the different mechanical strengths on two sides of this point, this area could be vulnerable to excessive bending and force application. This has happened to cables fitted with earlier versions of prototypes. One example is shown in Figure 3.5.

The solution for protecting this area is also shown in Figure 3.5. Some extra extended structures clamping farther on the more rigid cable part are added, circled by a green line in the drawing. These extra structures can prevent a sharp bend in this area. In addition, the 45 degree angle matching feature at the transition part also provides extra strength along the cable direction. So when the connector is accidentally pulled, the force will not be applied onto the fragile solder joints or damage tracks.

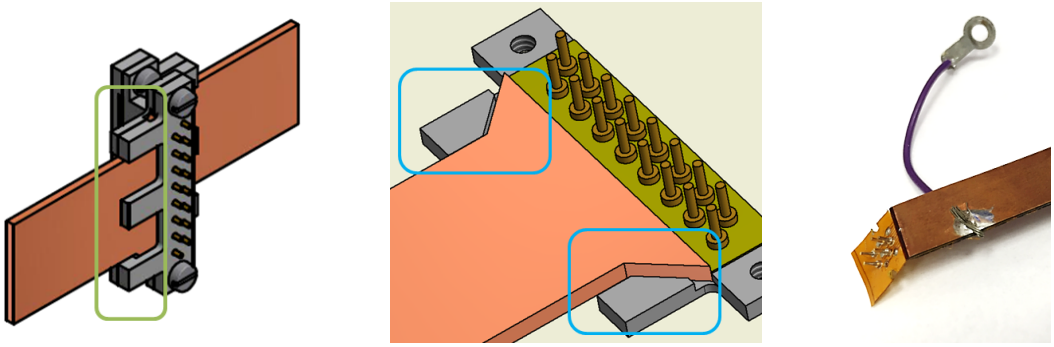


Figure 3.5: Examples of connector design and prototype: (left) One design of a connector set using Autodesk Inventor. The structure circled by a green line is added to protect against excessive bending at the interface between connector and body of the cable; (middle) Details of a 45 degree angle transition design to increase attaching strength; (right) An example of a broken prototype cable due to lack of the extra protective structures in its connector.

After preparing the two separate parts, we can then carefully solder the individual pins and sockets to the laminated cables and assemble the connector bodies. Although the tracks only run on a single side of the cables without any via, each pad has a corresponding backing on the other side. So when soldering the metal conductors into the pads' through holes, they can be soldered on both top and bottom sides, which

again gives more mechanical strength to the solder joints. Lastly, protectors made of FR4 are attached to the pin side, and kept on until cables are properly installed, so that the pins will not be bent during transportation or installation. Examples of finished 16-way cables and connectors are shown in Figure 3.6.

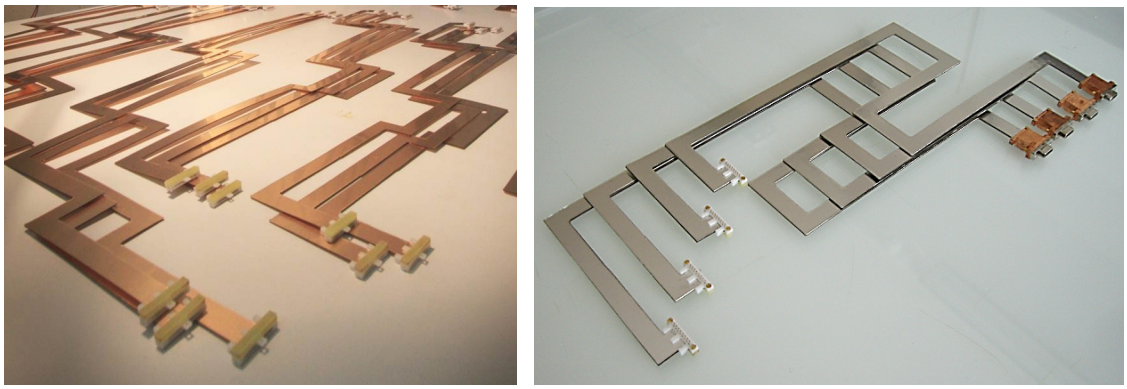


Figure 3.6: Examples of finished semi-flexible laminated copper and stainless steel cables with connectors attached.

3.2 Radioactive Background Control and Material screening

As the primary motivation of this cabling system, one of the most important and initial considerations is how to control the radioactive background it could induce.

As discussed in Chapter 2, among all the possible background, the neutron induced nuclear recoil is the most prominent problem in a WIMP direct search experiment, namely, EDELWEISS. The neutrons affecting detectors can come from various sources, and mainly two of them need to be considered when designing the cabling system. One neutron source is the decay of radioactive isotopes in the materials used, the other one is (α, n) reaction in the cables.

Further, the more material that is used in the cables, the more background they will introduce. So, the material budget also has to be controlled and the design should be as compact as possible.

Therefore, all the materials need to be screened and estimated carefully and should be as radiopure as possible. As this cabling system starts right next to the detectors, the specification for it, especially for the part that is in the vicinity of detectors, is most stringent.

Based on the two main sources, one step of material selection is testing the radioactivity level and choosing those with the least radioactive isotope contaminations. But even highly radiopure material could still induce a large neutron background if it contains elements that have a high (α, n) reaction cross section. Therefore, in addition to radioactivity tests, the chemical composition of possible materials needs to be checked.

3.2.1 Element Screening Based on (α, n) Reaction Cross-Section

The (α, n) reaction is normally initiated by the alphas generated by decays of uranium and thorium contaminations within the surroundings and the detector materials. The probability of such reactions normally depends on Q-value, energy threshold and height of the Coulomb barrier. [73]

Before the alpha particles can be close enough to interact with nuclei and produce neutrons, they need to penetrate the Coulomb barrier:

$$U_{coulomb} = \frac{Z_1 Z_2 e^2}{r}, \tag{3.1}$$

where e^2 is 1.44 MeV·fm, Z_i are the corresponding atomic numbers and r is the interaction radius. A common expression for interaction radius is $r = r_1 + r_2 = r_0({A_1}^{1/3} + {A_2}^{1/3})$, where r_0 is 1.2 fm, and A_i are the corresponding mass numbers. [73, 74]

This means the cross-section of (α, n) reactions will be suppressed for heavy elements which have higher atomic numbers Z. Thus in these high-Z materials, the

neutron production is dominated by spontaneous fission. And the neutron background induced by them depends more on the radioactive contamination levels instead of the cross-section of the (α, n) reaction.

Nucleus	Natural Abundance (%)	Q-Value (MeV)	Threshold Energy (MeV)	Coulomb Barrier (MeV)	Maximum Neutron Energy for 5.2 MeV Alpha
^{4}He	100	-18.99	38.0	1.5	
^{6}Li	7.5	-3.70	6.32	2.1	
^{7}Li	92.5	-2.79	4.38	2.1	1.2
^{9}Be	100	+5.70	0	2.6	10.8
^{10}B	19.8	+1.06	0	3.2	5.9
^{11}B	80.2	+0.16	0	3.2	5.0
^{12}C	98.9	-8.51	11.34	3.7	
^{13}C	1.11	+2.22	0	3.7	7.2
^{14}N	99.6	-4.73	6.09	4.1	
^{15}N	0.4	-6.42	8.13	4.1	
^{16}O	99.8	-12.14	15.2	4.7	
^{17}O	0.04	+0.59	0	4.6	5.5
^{18}O	0.2	-0.70	0.85	4.6	4.2
^{19}F	100	-1.95	2.36	5.1	2.9
^{20}Ne	90.9	-7.22	8.66	5.6	
^{21}Ne	0.3	+2.55	0	5.5	7.6
^{22}Ne	8.8	-0.48	0.57	5.5	4.5
^{23}Na	100	-2.96	3.49	6.0	1.8
^{24}Mg	79.0	-7.19	8.39	6.4	
^{25}Mg	10.0	+2.65	0	6.4	7.7
^{26}Mg	11.0	+0.03	0	6.3	5.0
^{27}Al	100	-2.64	3.03	6.8	2.2
^{29}Si	4.7	-1.53	1.74	7.2	3.4
^{30}Si	3.1	-3.49	3.96	7.2	1.4
^{37}Cl	24.2	-3.87	4.29	8.3	1.0

Table 3.1: Main properties of (α, n) reactions for light element isotopes. Values taken from [73].

For light elements, the Q-value becomes quite important for the probability of the (α, n) reaction. The Q-value is the difference between energies of initial particles and final products of the reaction. A reaction with a positive Q-value is exothermic. Otherwise, it is endothermic. For an endothermic reaction, the alpha particle needs to have at least that much energy in the centre-of-mass frame for the process to be possible. Transfer this value into laboratory frame, and there is the threshold energy:

$E_{threshold} = -Q(1 + 4/A)$ if Q is negative; $E_{threshold} = 0$, if Q is positive. Table 3.1 summarises the main relevant properties for isotopes of light elements.

Therefore, for a certain low-Z element, if one or more of its naturally abundant isotopes can interact with alpha particles and produce neutrons, as well as having a low energy threshold for such (α, n) reaction, then it can be extremely problematic for a low background experiment like EDELWEISS.

This explains why the coaxial cables are identified as one of the biggest contributions to the neutron background in EDELWEISS-II. In these cables, PTFE, consisting wholly of carbon and fluorine, is used as the insulator. Although PTFE has very good dielectric properties, the fluorine in it fits the criteria of "problematic" elements as described above. Only one isotope of fluorine occurs naturally, the stable ^{19}F, which can interact with alpha particles as follows:

$$\alpha + {}^{19}F \rightarrow {}^{22}Na + n\,.$$

It has a very low atomic number, nine. And its energy threshold for (α, n) reaction is also very low, which is only 2.36 MeV (Table 3.1), while the incident alphas usually have an energy of around 5 MeV. Therefore, the presence of fluorine, especially above the PE and lead shielding and near to the detectors like cold cabling, will result in a relatively large number of neutrons.

Similarly, some other light elements, such as beryllium, aluminium and silicon, can also induce a high neutron background and therefore need to be limited to a very small amount. Especially in the cold cabling system that is near to the detectors, they should be avoided if possible.

Figure removed due to copyright reasons.

Figure 3.7: Chemical structures of some material candidates: (left) Apical AV [75] / Kapton H [76]; (right) Delrin [77].

On the other hand, the naturally abundant isotopes of oxygen, nitrogen and carbon have energy thresholds higher than the typical alpha particles' energies. They are therefore much safer despite their low atomic numbers. This can be very reassuring since most of the candidates in the dielectric and connector housings are composed of these light elements. For our cabling system, the commonly used polyimide substrates in the flexible circuit are Kapton developed by DuPont or Apical developed by Kaneka. There are different types and variations with the product series. Two basic types, Kapton H and Apical AV, have the same chemical formula $(C_{22}H_{10}N_2O_5)_n$ [75, 76] and their chemical structure is shown in Figure 3.7. As they contain only carbon, hydrogen, nitrogen and oxygen, they could be suitable to be used. And similarly, one suggested option for making the plastic connector housings is Delrin, whose molecular formula is $(CH_2O)_n$ as shown in Figure 3.7.

Material	Total Neutron Yield $(g \cdot s \cdot ppb)^{-1}$	
	Uranium	Thorium
PTFE	8.851×10^{-10}	3.496×10^{-10}
Apical / Kapton	3.299×10^{-11}	8.297×10^{-12}
Delrin	2.437×10^{-11}	4.186×10^{-12}
Copper	1.384×10^{-11}	9.358×10^{-13}

Table 3.2: Total neutron yield in different materials (including spontaneous fission). The rates are given per gram of material per second per ppb of U / Th concentration. Values calculated by V.A. Kudryavtsev, using SOURCES4A.

For comparison, Table 3.2 shows the total neutron yield of several different materials. The values include contributions from (α, n) reactions and spontaneous fission.

Using the same principle, all the materials' chemical compositions are checked if possible before further radioactivity tests.

3.2.2 Radioactivity Contaminations Test Results

All the material candidates that pass the chemical composition check then need to go through tests of radioactivity levels. Raw materials, especially metal alloys, can have very different contamination levels depending on the manufacturers and the common industrial techniques. The production process, etching in particular, can also introduce extra radioactive isotopes. The etchants are not very easily precisely controlled or to test. So to see the total effect, we have also tested some samples that have been through the etching process.

The requirements on radiopurity for materials are usually based on the number of background events that the components can introduce. The general requirement for neutron background is that the total background event count should be at the order of around 1 in 10^4 kg·days. For gamma-ray, the goal was to control it to be well below EDELWEISS-II background [69].

Material	238U		232Th			40K	137Cs	60Co	Others
	226Ra	210Pb	234Th	228Ra	228Th				
Delrin	3.1 (1.3)	< 26	< 16	< 7.7	1.5 (1)	< 43	< 2	< 2.3	
Mil-Max pin 0508	31.5 (19.7)	11000 (1056)	< 225	< 144	< 53	675 (221)	< 47	< 36	
Mil-Max socket 8874	< 117	26076 (4042)	1638 (581)	< 284	< 174	< 2645	< 132	< 129	
OMNETICS NanoNSS SMT 11-pin connector	4100 (600)	6400 (800)	5300 (200)	4700 (500)	4000 (400)	5100 (1000)	< 150	< 150	
Samtek connector	4000 (1000)	18700 (3500)	< 6000	2700 (1000)	4400 (1100)	7900 (2900)	< 500	< 750	
ESPANEX SB adhesiveless, copper clad polyimide laminate, double side	< 3.5	< 109	< 14	< 9.5	< 3.3	< 55	< 1.8	1.4 (0.6)	
ESPANEX SB after etching	5 (3)	182 (94)	< 25	< 6	6.4 (1.6)	< 54	< 3	< 2.2	
GTS stainless steel apical laminate, double side	13 (5)	651 (241)			11 (4)	275 (63)			
GTS stainless steel apical laminate, after etching	20 (5)	< 120			33 (4)	175 (51)		4 (3)	
PEN with full steel foil	< 22	838 (89)		21 (12)	13 (7)	< 174	< 9		7Be: 201 (46)
Arlon 92ML ceramic filled epoxy laminate	7054 (1000)	5690 (230)	8500 (500)	4730 (120)	5240 (500)	2660 (200)	< 250	< 200	
GTS 387 apical tape, single side	11 (4)	< 71			5 (2)	< 113	< 7	5 (2)	
Dupont kapton tape	15 (5)	< 207	< 90	< 24	5 (4)	146 (91)	8 (4)	< 9	

Table 3.3: Selected radioactivity test results of materials chosen for cabling (mBq/kg).

The radioactivity contaminations in material samples have been measured at LSM using low-background gamma-ray spectrometry by P. Loaiza and M. De Jesus.

Selected test results are shown in Table 3.3. Around 20 further samples have been tested and most of the tested materials subsequently eliminated.

For connectors, two commercially available candidates are tested and found to exhibit comparable radioactivity contamination levels. They are both decided to be too radioactive for EDELWEISS-III. As for the in-house made connector, test results showed that Delrin is radiopure enough and mechanically robust, hence it is chosen for the connector housing material. And the radioactivity contamination levels of the Mill-Max all-metal pins and receptacles that are intended to be used for connectors are also validated by these tests.

It is noticed that the adhesives usually have a higher radioactivity level than polyimide and metal layers. And for different types, the value can vary drastically. So besides carefully choosing the adhesive material, the number of adhesive layers should also be minimised in the design. Based on the test results and material availability, the adhesiveless copper clad polyimide laminates from Nippon Steel Chemical ESPANEX series, the stainless steel-polyimide laminates and the Apical tapes manufactured by GTS Flexible Materials are chosen for producing the semi-flexible cables.

3.3 Capacitance

Besides background control, the effect cabling has on the electric detector signals is clearly an important factor that enters the final design.

NTD-Ge sensors used in EDELWEISS are read out by sending a modulated bias current through them and measuring the voltage drop across. Due to the RC time constant caused by the NTD-Ge resistance (typically a few mega-Ohms) and the parasitic capacitance of the detector / cabling / readout system, the modulation frequency will be limited. It is important to minimise this effect on the signal wave

form. The signal to be detected is mediated by phonons and thus has typical time constants of order milli-seconds. As a result, a modulation frequency around 1 kHz is desirable, which limits the cable capacitance to around several tens of pico-Farad.

For the ionisation channel on EDELWEISS detectors, the signal voltage presented to the readout electronics is the ionisation charge divided by the total capacitance of the detector / cabling / readout system, and thus, the cabling capacitance has to be small so that any ionisation signal voltage remains large compared to the dominant voltage noise of the input J-FET of the readout system.

In any case, minimizing cable capacitance is a priority for both signal channels.

3.3.1 Design Implications

The capacitance concerned here is mainly that between signal tracks and the electrical grounding planes. The two shielding (grounding) layers described in Section 3.1 are electrically connected and grounded by the cryostat infrastructure. Each of the signal tracks then forms a capacitor with this shielding. The final capacitance between a signal track and grounding is a combination of this series of capacitors and the parasitic capacitance between tracks (see Figure 3.8).

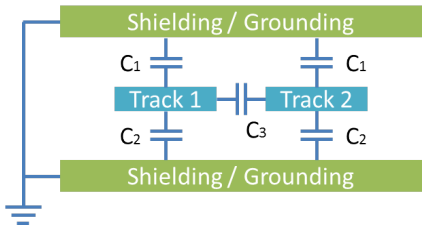


Figure 3.8: Schematic showing the cross-section of the simplest cable model with only two signal tracks. C_1 and C_2 are the capacitances between tracks and grounding; C_3 is the parasitic capacitance between adjacent tracks.

If taking the simplest model, in which the cable only has two tracks (Figure 3.8), then the capacitance C between Track 1 and Grounding is approximately:

$$C = C_1 + C_2 + \frac{C_3(C_1 + C_2)}{C_1 + C_2 + C_3}, \tag{3.2}$$

which indicates that the capacitance C_1, C_2, C_1/C_3, and C_2/C_3 are all important factors for controlling the capacitance C. This also shows that if more tracks are present, which is more realistic, the parasitic capacitances will add on to the total amount. But they get smaller when being further away and thus have smaller impact.

As the cable has a geometry that is very common in PCBs, extensive studies of the capacitance of this kind of setup has been done. Since the cross-section is uniform, the capacitance per unit length is calculated for many common cases. To get the precise value of capacitance, the best numerical tool is a 2D solver, which assumes a uniform cross-section of the cable and solves Maxwell's equation using the geometry with appropriate boundary conditions. However, many approximate analytical equations exist that can also be used for estimating values as well as informing the design of the cabling.

For C_1 and C_2, transmission line designs called microstrip and stripline (Figure 3.9) are most relevant to the estimation here.



(a) Microstrip **(b) Stripline**

Figure 3.9: Cross-sections of two common transmission line geometries.

Equation (3.3) is the capacitance per unit length of microstrip approximation recommended by IPC, a global trade association for the PCB industry [78].

$$C_{microstrip} = \frac{0.67(1.41+\varepsilon_r)}{ln\left\{\frac{5.98\times h}{0.8\times w+t}\right\}} \text{ pF/inch} = \frac{26.38(1.41+\varepsilon_r)}{ln\left\{\frac{5.98\times h}{0.8\times w+t}\right\}} \text{ pF/m}, \qquad \textbf{(3.3)}$$

where ε_r is the relative dielectric constant of insulation, h is the dielectric thickness, w is the track width and t is the track thickness.

C_3 can be estimated as two parallel wires:

$$C_{parallel\ wires} = \frac{\pi \varepsilon_0 \varepsilon_r l}{arcosh(p/w)}, \tag{3.4}$$

where ε_0 is the permittivity of free space, ε_r is again the relative dielectric constant of the insulation, and l, p and w are the length, pitch and width respectively of the tracks.

From Equation (3.2) - (3.4), several aspects in the cable construction should be adjusted carefully to minimise the capacitance:

- The thickness of dielectric materials should be reasonably thick. The limit comes from several aspects. First of all, the material budget is defined by the radiopurity requirements. Secondly, the cross-section area needs to be controlled by the heatload consideration, which will be discussed in Section 3.4. And thirdly, the mechanical pliability will be compromised as the thickness increase, so it cannot be too thick.
- The track width should be as small as the photolithography process allows.
- The track pitch should be reasonably big. As this essentially defines the total width of cable, it is also limited by the material budget and the heat conduction, as well as the available room for running the cables.
- The thickness of each track should be small, so laminate material with thinnest possible metal layer thickness should be used.
- Also, an insulator with low dielectric constant should be chosen. But this is largely limited by the available flexible materials that are both suitable for photolithography and approved as low-background material, following radiopurity assay. For example, PTFE has a rather low dielectric constant, but obviously cannot be used for its high (α, n) cross section (see previous section for further detail).

As discussed in Section 3.2, based on the availability of materials and the radioactivity background limits, the ESPANEX copper-polyimide laminate, the GTS stainless steel-polyimide laminate and the GTS apical tape are chosen as candidate materials. Hence the relative dielectric constant is confined to around 3.3 at 300 K.

The versions with thinnest metal layers of ESPANEX copper-polyimide laminate and GTS stainless steel-polyimide laminate are chosen to ensure smallest track thickness. The thickness of copper layer and stainless steel layer of the materials used are 18 μm and 25 μm respectively.

Realistically, to achieve a relatively reliable process, the track width of copper cables is defined to be 80 μm and the stainless steel cables 125 μm. Although the photolithography process at Oxford PFU is capable of producing thinner tracks on a small scale, however, pushing the track width to the capable limit for our typically 1 m cables can result in a very low yield due to track breakages (as shown in Figure 3.2).

Therefore, the two remaining factors in design that can be adjusted to get a smaller capacitance are the thickness of insulator and the pitch of tracks. The final values of these factors need to be compromises considering several physics aspects. As for how much each factor affects the final capacitance, we will use a 2D field solver to calculate the values. This will provide some guidelines and initial parameters for designing the prototypes.

3.3.2 Numerical Calculation and Measurements

Using finite element method, the capacitance between signal tracks and grounding of realistic cable geometry can be numerically calculated. The 2D field solver used here is Finite Element Method Magnetics (FEMM) by David Meeker [79].

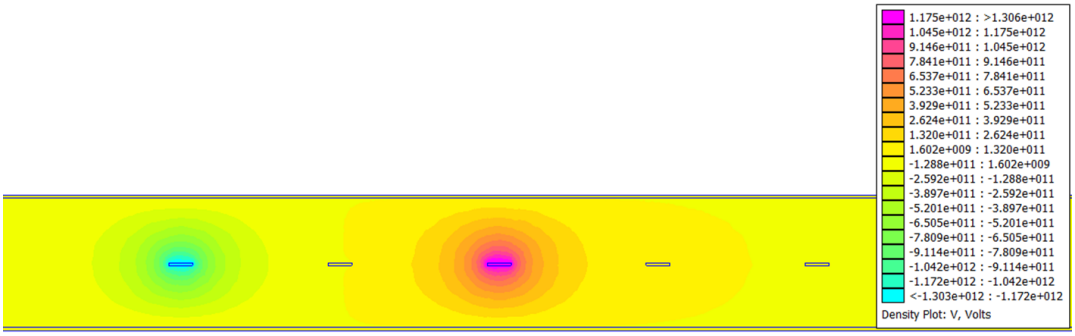


Figure 3.10: One example of capacitance calculation. Here is the partial cross-section of a cable. The planes on top and bottom are grounding metal layers and the small rectangles are signal tracks. The space between top and bottom ground planes is filled with dielectric material. In this plot, the track on the left and the track in the middle are defined to have equal and opposite charge. The corresponding electrical potential distribution is calculated and shown.

One example of the result is shown in Figure 3.10. The 2D solver has been verified by calculating some geometry that has analytical solutions. The accuracy varies with different boundary conditions settings, mesh sizes, etc. But the agreement is generally better than 5% given appropriate boundary conditions, which is good enough to give estimations of different constructions' cable capacitance and implications for the final cable design.

Several variations of cable construction are calculated using FEMM and the results are shown in Figure 3.11. The results' accuracy is mainly affected by how close the relative dielectric constant is to 3.3.

From the calculated results we can see that, the thickness of dielectric has a big effect on the capacitance. However, the capacitance does not change much even when the pitch of tracks is doubled. Therefore, the cable should be as thick as allowed by radiopurity and heatload requirements (Section 3.2 and 3.4), but the tracks can be more compact so that the cable cross-section and material budget can be smaller.

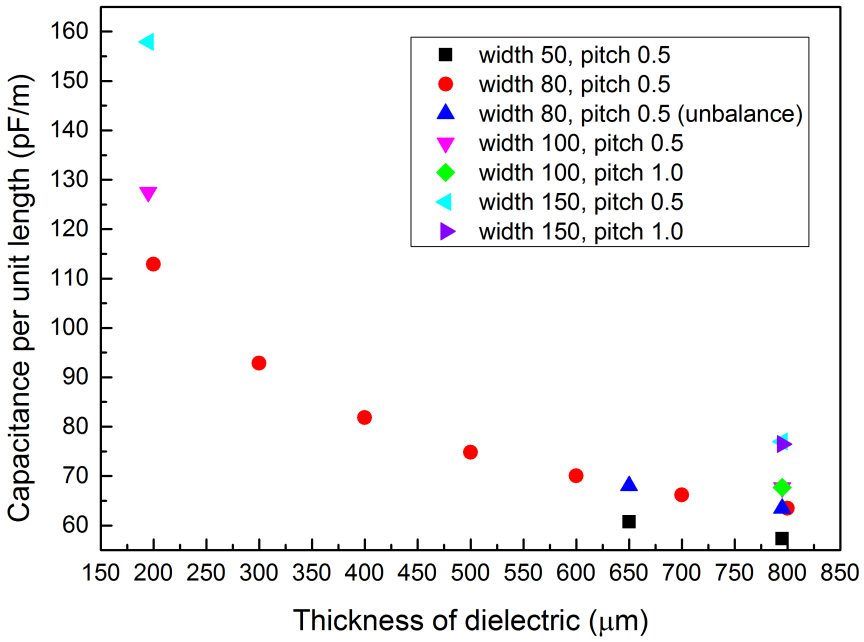


Figure 3.11: Calculated capacitance per unit length between signal track and grounding of different cable geometries using FEMM. The track thickness used here is 18 μm. The track widths are in micrometres and the track pitches are in millimetres.

The actual capacitance of finished cable will also be affected by the pads and attached connectors. In addition, its track width will be different from the artwork and varies at places due to the cable geometry and the etching process. For a 16-way copper cable sample with 18 μm thick, 80 μm wide tracks, and 725 μm (350 μm + 375 μm) thick dielectric layer, the observed capacitance at 300 K is 66.8 pF/m, which falls in the indicated range from the numerical calculation.

It is also noticed that the cable capacitance decreases when cooled to 4 K, which is in favour of operation at cryogenic temperatures. The observed capacitance between signal track and grounding of the prototype cable falls to approximately 75% of its 300 K value when tested in liquid helium. This can be attributed to the temperature dependence of the polyimide/epoxy insulator dielectric constant. Similar effect has also been observed in works done by others. For example, Murphy et al. constructed

capacitors using kapton, epoxy and copper that also showed similar temperature dependence [80].

3.4 Heatload

The cryogenic detectors for WIMP searches are normally operated in the milli-Kelvin temperature range. In EDELWEISS, the germanium detectors are operated at around 18 mK. Based on the radiopurity consideration, the laminated cold cabling system should be suitable for bridging at least from the detectors at milli-Kelvin levels to the cold electronics at 100 K. If the heat conduction due to this cold cabling system is too large, then this will prevent the cryostat from reaching its base temperature or affect the stability of operating temperature. Therefore, the heatload from cabling needs to be carefully assessed and controlled.

3.4.1 Temperature Stages in Dilution Refrigerator

EDELWEISS, CRESST and CDMS all use ^{3}He - ^{4}He dilution refrigerators to achieve their milli-Kelvin operating temperature. The prototype cryogenic detectors and etched metal foil cabling are also tested inside a Kelvinox 400 dilution refrigerator (K400). This kind of cryostat is cooled down in stages.

To explain the principle of how dilution refrigerator works and consequently generates different temperature levels inside, we take the K400 dilution refrigerator as an example. A schematic diagram of its Inner Vacuum Chamber (IVC) is shown in Figure 3.12. For cooling it down to base temperature, first liquid nitrogen is filled into the main bath while helium exchange gas is present in the IVC to precool the cryostat to 77 K. Then the liquid nitrogen is blown out and the main bath is filled with liquid helium, cooling the IVC to 4.2 K. Next, the IVC is pumped to a good vacuum (normally better than 10^{-6} mbar), and at this point, the 1K pot can be started. The 1K

pot is continuously filled with liquid helium from the main bath. By pumping on it, the 1K pot, and subsequently the cryostat, can be cooled down to about 1.5 K.

Lower temperature is achieved by circulating a mixture of two isotopes of helium, ^{3}He and ^{4}He, in the dilution circuit. The ^{3}He exiting from a pump at room temperature is first precooled by the 4.2 K main bath and then condensed by the 1K pot. Through a series of further precooling heat exchangers, the ^{3}He enters the mixing chamber where the ^{3}He - ^{4}He mixture separates into a ^{3}He concentrated phase and a ^{3}He dilute phase.

In the mixing chamber, the dilute phase is pumped via the still. The cooling occurs when ^{3}He atoms cross the phase boundary from the concentrated phase to the dilute phase, which is an endothermic process and eventually allows the mixing chamber to reach the cryostat's base temperature below 10 mK. The ^{3}He is then driven up by osmotic pressure. It passes through the heat exchangers to precool the incoming ^{3}He and enters the dilute liquid phase in the still, which is heated and has a temperature of around 600 mK. Since the vapour pressure of ^{3}He at this temperature is much larger than that of ^{4}He, the vapour above the dilute liquid phase typically has a ^{3}He concentration of about 90%. This vapour is constantly pumped away, leaving typically less than 1% ^{3}He concentration in the dilute liquid phase in the still. As a result, the osmotic pressure difference mentioned before that drives the cold ^{3}He up from the mixing chamber is created. The concentrated vapour pumped away is then resupplied to the condenser line continuously, completing the cycle.

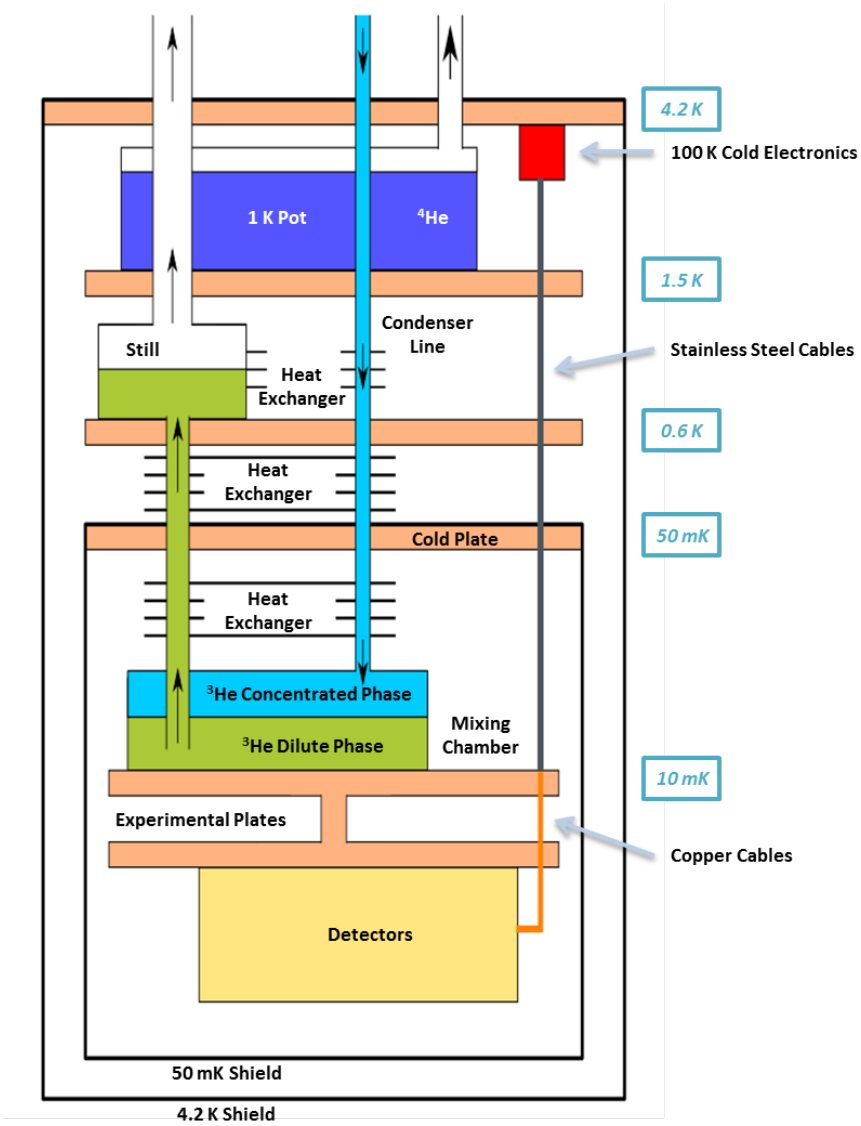


Figure 3.12: Schematic diagram of Kelvinox 400 dilution refrigerator Inner Vacuum Chamber, which is immersed in liquid helium at 4.2 K. The values in blue boxes are indications of the rough temperature ranges instead of the accurate numbers.

The copper experimental plates and detectors are cooled to operating temperature by connecting to the mixing chamber. The cold electronics is attached to the 4.2 K plate and kept at around 100 - 120 K by its own heating while its housing should be at 4.2 K. At each temperature level in between, a copper plate is attached to prevent thermal radiation from reaching lower levels, which is also used for heat anchoring of cabling in stages. In the prototype cabling system installed in K400 at Oxford, the cabling is heatsunk at 4.2 K (through cold electronic housing), 1.5 K, 0.6 K, 50 mK

and 10 mK. For the cabling in EDELWEISS, due to different cryostat geometry, the heatsinks can be distributed at 4.2 K, 1.5 K, 0.7 K, 100 mK (intermediate temperature level) and 10 mK if necessary.

Cooling power at different temperatures stages depends on the individual design of the cryostat. Typically the cooling powers of the mixing chamber and the still are in the microwatt range and milliwatt range, respectively. Again, take the K400 as an example, its cooling powers at the mixing chamber and the still are tested during commissioning and listed in Table 3.4.

M/C Temperature (mK)	M/C Cooling power (μW)	Still Cooling power (mW)
4.8	Base temperature	8.0
11.2	2.0	20.0
16.0	5.0	20.0
42.0	50.0	20.0
98.0	350	30.0

Table 3.4: K400 cooling power measurement results. Values from [81].

The heatload introduced by cabling at each heaksink should not be significant compared to the cooling power. Otherwise it will raise the temperature at parts of the cryostat which could prevent cooling down to the desired low temperature.

3.4.2 Thermal Conductivity

The heat conduction by a material of cross-section A and length L with a thermal conductivity coefficient κ is given by:

$$\dot{Q} = \frac{A}{L}\int_{T_1}^{T_2} \kappa(T)dT. \tag{3.5}$$

Heat can be transferred through solids by two kinds of carriers – conduction electrons and lattice vibrations (phonons). The thermal conductivity coefficient κ of these carriers is determined by specific heat C, velocity v and mean free path λ. The cabling consists of metal conducting tracks and shielding planes as well as dielectric

insulators. In practice most metals and alloys tend to be dominated by electron heat conduction and insulators by phonon heat conduction.

At the low temperature range, where the cold cabling is more of a concern, velocities of both electrons and phonons are independent of temperature. The mean free path is limited by the scattering processes of heat carriers. At low temperatures, as there are only a small number of thermally excited phonons, the scattering of electrons and heat carrying phonons from crystal defects or boundaries, which are temperature independent, dominates. Thus the mean free path for both electrons and phonons at this kind of temperatures is also temperature independent. Therefore, the temperature dependence of thermal conductivity at low temperatures is given by its temperature dependence of specific heat. In general, it is $\kappa \propto T$ for electrons and $\kappa \propto T^3$ for phonons [82, 83].

3.4.3 Heatload Calculation

The heatload calculation of cabling depends largely on the specific setup – temperature stages, lengths between them, cable cross-sections and so on. So here, the calculation will use the setup of K400 dilution refrigerator at Oxford. The number of tracks on one cable is flexible according to the requirements of different experiments, so the heat conduction of material possessed by each track is calculated here. Namely, the calculation is based on a "cable" with one signal track and its cable width is the track pitch. The track thickness for stainless steel and copper cables are 25 μm and 18 μm respectively. The insulator thickness depends on the cable stack-up construction.

We can estimate the heatload with general tabulations of the thermal conductivity. Very often, the tabulated values are given as thermal conductivity integral, $\int \kappa(T)dT$.

From Equation (3.5), we have:

$$\dot{Q} = \frac{A}{L}\int_{T_1}^{T_2}\kappa(T)dT = \frac{A}{L}\left[\int_{T_0}^{T_2}\kappa(T)dT - \int_{T_0}^{T_1}\kappa(T)dT\right]. \quad \textbf{(3.6)}$$

Therefore, the heat conduction between T_1 and T_2 can be calculated using the thermal conductivity integrals with reference to the same temperature T_0.

For most materials, the values do not vary a lot between different samples, but for pure metal, the thermal conductivity depends largely on its impurity and crystal dislocations. As a result, while general values can be used to properly estimate the heatload of the insulator and stainless steel parts of the cables, heatload estimation using general values for the copper parts can be off by a few orders of magnitude.

Fortunately, the thermal conductivity of pure metal can be calculated using its electrical conductivity, which is much easier to measure. This relation is given by the Wiedemann – Franz law:

$$\frac{\kappa}{\sigma} = L_0 T\,, \quad \textbf{(3.7)}$$

where κ is thermal conductivity, σ is electrical conductivity and L_0 is the Lorenz number, which is a universal constant 2.45×10^{-8} W·Ω/K^2. [82, 83]

100 K – 4.2 K

The heatload from cold electronics around 100 K to 4.2 K heatsink is relatively complicated to calculate for several reasons. First of all, $\kappa(T)$ varies considerably over the large temperature range and the temperature dependence can be quite complicated. In addition, the actual temperature of cold electronics depends on the optimal operating temperature of the FET preamplifiers, which normally can vary from 100 K to 120 K. But it is still possible to estimate the heatload.

Since the calculation is based on the prototype system in K400, the cold electronics temperature is assumed to be 120 K – the optimal operating temperature for it. From Table A2.1 in [83], we have $\int_{4K}^{120K}\kappa(T)dT = 0.726$ kW/m for type 316

stainless steel. For polyimide and epoxy, the thermal conductivity of kapton can be a good representation for estimation. As measured by Rule et al. and fitted by Lawrence et al., $\kappa(T) = 2.996\times10^{-5}T^{0.9794}$ W/cm·K, for temperature between 4.2 K and 300 K [84, 88].

For stainless steel cable, assuming the length is 100 mm, then

$$\dot{Q}_{total} = [0.1815wt + (0.363 + 197.252d)pt]\ \text{W}, \tag{3.8}$$

where *wt* is the track width, *pt* is the track pitch, and *d* is the insulator thickness, all in m. As discussed in previous chapters, the stainless steel signal track is about 125 μm wide.

From Equation (3.8), since the full cable thickness is normally a few hundred micrometres, the track pitch has a much larger effect on the heat conduction comparing to the insulator thickness in the 4.2 – 120 K range. This is actually opposite to their effects on cable capacitance.

Taking a cable with 0.5 mm track pitch and 880 μm insulator thickness, the heatload to the 4.2 K level from each track is 0.29 mW. Considering the 4.2 K level is maintained by liquid helium bath, and its latent heat of vaporisation is 2.589 J/mL, even 1000 such tracks will only boil off 0.4 L helium every hour.

For copper cables, Figure 3.13 shows the measured electrical resistivity ρ of the copper material used for fabrication. The electrical conduction process of metal is rather similar to the thermal conduction process, which also mainly depends on the scattering processes of electron-electron ($\rho \propto T^2$), electron-phonon ($\rho \propto T^{n(T)}$) and electron-impurity / dislocation. Over the large span of 4.2 K – 300 K, fitting the temperature dependence of electrical resistivity from measured data is very complex and beyond the scope of this work. Here the data is fitted with an empirical curve based on the work of A Bergmann et al [85] and E Borchi et al [86] as:

$$\rho(\mathrm{T}) = \frac{1}{\sigma} = (5.52354\times10^{-9} + 3.66968\times10^{-13}T^2 - 1.80583\times10^{-18}T^4)\ \Omega\cdot\mathrm{m}\,. \tag{3.9}$$

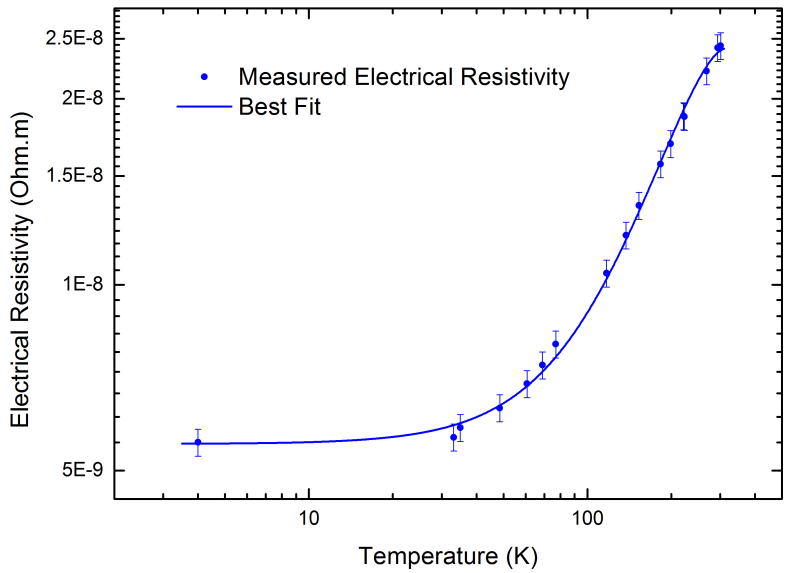


Figure 3.13: Electrical resistivity of the copper material used for fabricating etched metal foil cables over temperature range 4.2 K to 300 K.

From Equation (3.9) and the Wiedemann – Franz law (3.7), for the copper material used here, $\int_{4K}^{120K} \kappa(T)dT = 22.633$ kW/m. That is about 30 times of the thermal conductivity integral of stainless steel, which means that copper cables will conduct too much heat if used for crossing different temperature levels.

Consequently, combining the radiopurity requirement, a two-section cable design is adopted: the radiopure copper cable section is used near detectors at 10 mK level; another stainless steel cable section, less radiopure but also less heat-conducting, is used further away behind lead and PE shielding to bridge 10 mK to higher temperature levels (Figure 3.12).

Below 4.2 K

With the two-section design, the copper cable does not cross different temperature levels, so the estimation of heat conduction afterwards is only for the stainless steel

cable. The thermal conductivity of stainless steel between 45 mK to 4.3 K measured by the CUORE experiment is $\kappa(T) = 0.0556T^{1.15}$ W/m·K [87]. For kapton, the thermal conductivity reported by Lawrence et al. is $\kappa(T) = 4.638\times 10^{-5}T^{0.5678}$ W/cm·K between 0.5 K – 5 K, while in Radebaugh et al.'s work, $\kappa(T) = 1.273\times10^{-5}T^{0.9817}$ W/cm·K between 0.02 K – 4 K (as quoted and fitted by Lawrence et al.) [88, 89]. Although Radebaugh et al.'s result covers a larger range, but to do a more conservative estimation, Lawrence et al.'s result is adopted and extrapolated here.

Similarly to previous calculation, the heat conductions of stainless steel cable with one track, between different temperature stages below 4.2 K, are calculated and listed in Table 3.5.

Temperature Stage	Heat conduction $\dot{Q}_{total}$
4.2 K – 1.5 K	$[0.126wt + (0.252 + 224.791d)pt]$ mW
1.5 K – 0.6 K	$[15.651wt + (31.302 + 50095.412d)pt]$ μW
0.6 K – 50 mK	$[2.043wt + (4.086 + 12391.333d)pt]$ μW
50 mK – 10 mK	$[4.994wt + (9.988 + 124151d)pt]$ nW

Table 3.5: Heat conduction per track of stainless steel cable. wt is the track width, pt is the track pitch and d is the insulator thickness, all in m. The lengths between levels are taken from the K400 cryostat.

Again, if the signal track is 125 μm with 0.5 mm pitch and the insulator is 880 μm thick, then the heatload from each stainless steel track to the 1.5 K, 0.6 K, 50 mK and 10 mK levels are estimated to be 0.24 μW, 39.65 nW, 7.75 nW, 60.24 pW, respectively. They are well within the typical cooling power of various levels.

3.4.4 Heat Anchoring Quality

The estimation in Section 3.4.3 is based on the assumption that the heatsink at each stage is perfectly effective and the cable has a uniform temperature along the cross-section. In reality, the inner signal tracks will have a slightly higher temperature

than the outer shielding due to the relatively low thermal conductivity of dielectric layers. Besides, the outer shielding may also be at a higher temperature than the solid structure it is attached to depending on factors like pressure, thermal contraction, interface mismatch, etc.

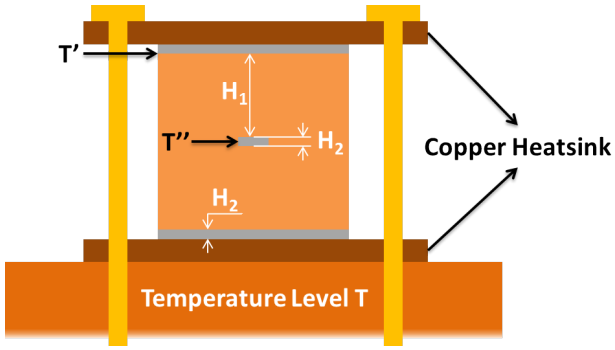


Figure 3.14: Schematic of heat anchoring. It also provides mechanical stabilisation to cables.

For most of the stages, heat anchoring is done by several high purity copper pieces clamping the cables together and then firmly attached to the desired temperature stages as shown in Figure 3.14. These heatsink pieces also provide mechanical stabilisation to cables to protect against vibration. Because of the flat cable geometry and the similar thermal expansion coefficients of polyimide and copper [83], given enough pressure (and a small amount of grease or epoxy if necessary), the shielding is generally sufficiently heatsunk.

As for the temperature difference between inner wires and outer surfaces, we can do a conservative estimation to see if this will be problematic.

Assuming the copper heatsink pieces are all uniformly at the same temperature T as the level they are attached to (Figure 3.14) and the cable is symmetrical. Then across one shielding stainless steel layer,

$$\frac{\dot{Q}_{wire} + \dot{Q}_{dielectric} + \dot{Q}_{shield}}{2} = \dot{Q}_{cond,1} = \frac{A}{H_2}\int_{T}^{T'} \kappa_{stainless\ steel}(T)dT\ .$$

For $\Delta T_1 = T' - T \ll T$,

$$\frac{\dot{Q}_{wire} + \dot{Q}_{dielectric} + \dot{Q}_{shield}}{2} = \frac{A}{H_2} \cdot \kappa_{stainless\ steel}(T) \cdot \Delta T_1 \ .^{1}$$

Similarly, across the insulator layers, $\Delta T_2 = T'' - T' \ll T$,

$$\frac{\dot{Q}_{wire} + \dot{Q}_{dielectric}}{2} = \frac{A}{H_1} \cdot \kappa_{polyimide}(T) \cdot \Delta T_2 \ .$$

H_1 and H_2 are taken as 440 μm and 25 μm respectively. Take the 4.2 K and the 50 mK level as examples, if the track is 125 μm wide with 0.5 mm pitch, and the copper heatsink is 20 mm long, then the results are listed in Table 3.6.

Level	ΔT_1	ΔT_2	Difference
4.2 K	1.3 mK	196.3 mK	4.7%
50 mK	5.5 μK	148.4 μK	0.3%

Table 3.6: Conservative estimations of temperature difference between the inner track and the outer shielding of a stainless steel cable using the heat anchoring scheme described in text.

The estimated values show that the temperature differences are relatively small. Therefore, the calculations in Section 3.4.3 should still hold under more realistic conditions.

3.5 Final Design

Considering aspects discussed in the previous sections and the material availability, we can see that within the radiopurity limit:

- The thickness of signal tracks and shielding / grounding should be small, so the ESPANEX adhesiveless copper-polyimide laminates with 18 μm copper from Nippon Steel Chemical series and the stainless steel-polyimide laminates with 25 μm stainless steel manufactured by GTS Flexible Materials are used to produce the tracks and the shielding layers for the copper and stainless steel sections respectively.

[1] Actually for the shielding layer itself, the mean heat conduction length is half the thickness. But for a conservative estimation, full thickness is used as the other components.

- The dielectric layer can be reasonably thick as long as the cables are mechanical pliable. In the final construction, the GTS apical-adhesive layers are used to build up the dielectric in both sections.
- The track width should be as small as possible. The limit mainly comes from the yield of photolithography process. After batches of prototypes, the tracks on artwork are set to be 80 µm and 125 µm wide for copper and stainless steel respectively.
- The track pitch can be small. For both sections, the pitch is set to be 0.5 mm.

The cable construction has been finalised accordingly. Figure 3.15 shows the final layer stack-up of the two sections.

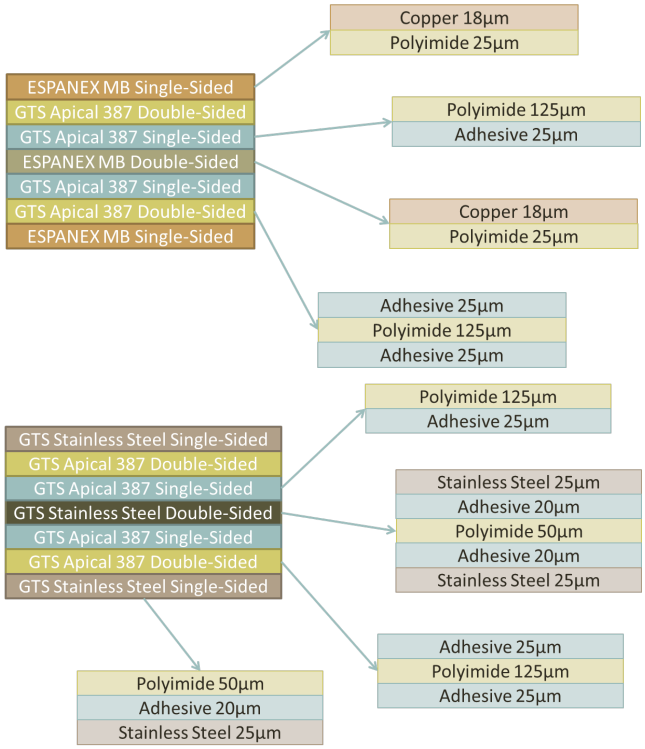
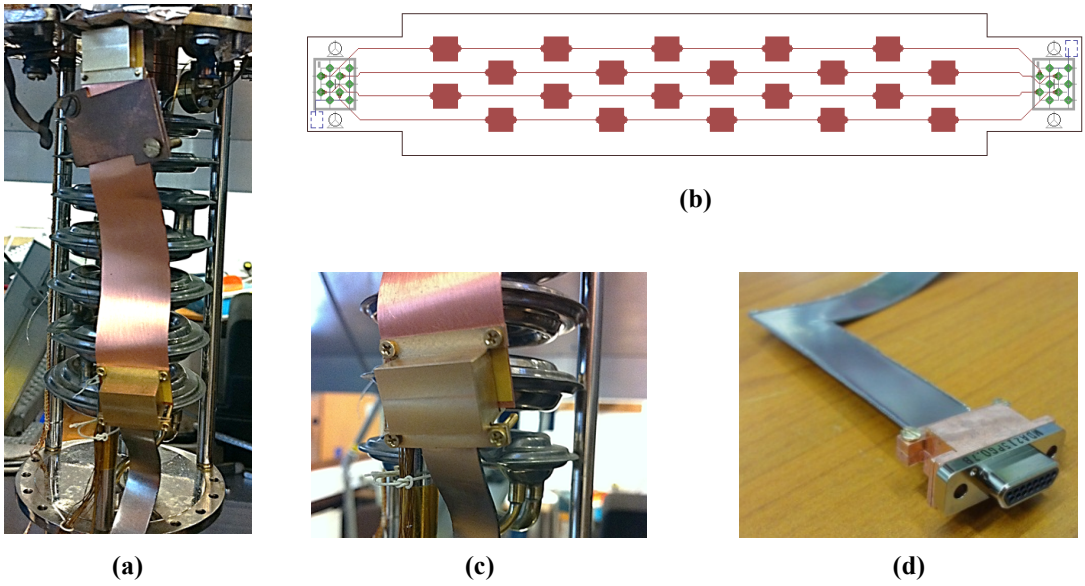


Figure 3.15: Cable stack-up of the final design: (top) copper section; (bottom) stainless steel section.

As for the connectors, they are constructed with metal pins / sockets from Mill-Max as conductors and Delrin from PDS-ARDEN as connector bodies as mentioned before.

Besides all these major considerations, there are also some practical optimisations in the final design. Following are some examples.

If the thin tracks connect directly to the much more sturdy round pads, the connections are very easily broken during or after soldering the metal conductor on. This is mainly due to the abrupt change in mechanical strength of different parts. To avoid this, the pads should slowly transit to the corresponding tracks when designing artworks, which results in a "raindrop" shape (can be seen in Figure 3.1). Also, sharp corners should be avoided in artworks and use round corners instead. Otherwise, acid could be trapped in the sharp corners during etching, which then leads to over-etching and leaves undesired weak points or breakages in cables.



(a) **(b)** **(c)** **(d)**

Figure 3.16: Example accessory parts of the cabling system: (a) extra 50 mK heatsink pieces installed in the K400; (b) circuit diagram of the 50 mK heatsink track layer; (c) metal box designed around the Delrin connector for more mechanical strength and better EM shielding; (d) metal box designed for the interface between laminated cable and other type of connector, providing similar functions as the box in (c).

Besides simply clamping cables for heat anchoring, extra heat-sinking sections can be added in the readout chain if necessary. A prototype heat-sinking piece is installed at the 50 mK level in K400 at Oxford as shown in Figure 3.16. The conducting lines contain a number of copper pads, separated by thin copper tracks (50

μm here), to provide better heat transfer in stages. This circuit is sandwiched between two copper layers heatsunk to 50 mK. However, this could increase the overall cable capacitance so its application needs to be carefully controlled.

The cable can also be made compatible with other kinds of connectors. Metal boxes can be designed around the connections to provide more mechanical strength and better EM shielding. Examples can also be seen in Figure 3.16.

4 Cabling Applications and Performance

After developing the cabling solution and deciding the cable stack-up as described in the last chapter, the following tasks would be defining a detailed plan for applying this system in specific cryostat setups as well as designing, fabricating, installing and testing the cables.

After batches of prototypes having shown satisfactory performance at Oxford and the LSM, a batch of final cables were produced here at Oxford and installed in the EDELWEISS setup.

The designed cold cabling setup and application in the EDELWEISS-III cryostat is introduced in this chapter first. Next, the performance of this cabling system during prototype tests and EDELWEISS runs is discussed. In addition, the future possibility of applying it to new generations of direct dark matter searches is also introduced here.

4.1 Application in EDELWEISS-III

For EDELWEISS-III, the cabling system is constructed as several sections with the first two sections close to the detectors being the semi-flexible laminated cabling and the farther away sections being the coaxial cabling. The radiopure copper cables are installed immediately after the detectors on the base temperature level of the EDELWEISS cryostat. As discussed previously, the copper section extends beyond the lead shielding (visible near the top) and the polyethylene (PE) that protects the detectors from background radiation (Figure 4.1). After passing through these shielding layers, a transition is made to the less radiopure stainless steel section that

conducts heat far less than copper as shown in Section 3.4. It then runs across the typical temperature levels of 100 mK, 700 mK and 1.5 K. At 1.5 K, this cabling section reaches the bottom of the cryostat inner layer and stops here. From this point up to room temperature, the signals are then transferred by sections of coaxial cables. This combination of the first two cabling sections allows satisfying the requirements of ultra-low background close to the detectors and also the maximum heat conductance that can be tolerated on detectors operated at milli-Kelvin temperatures.

In addition, to retain flexibility, one or more stainless steel cables can be replaced by coaxial cables using laminated cabling adapters (examples can be seen in Figure 4.1). It is not possible to similarly replace the copper cables as the coaxial cables will already cause the radioactive background to increase at positions beyond the shielding layer, let alone exposing them directly to the detectors.

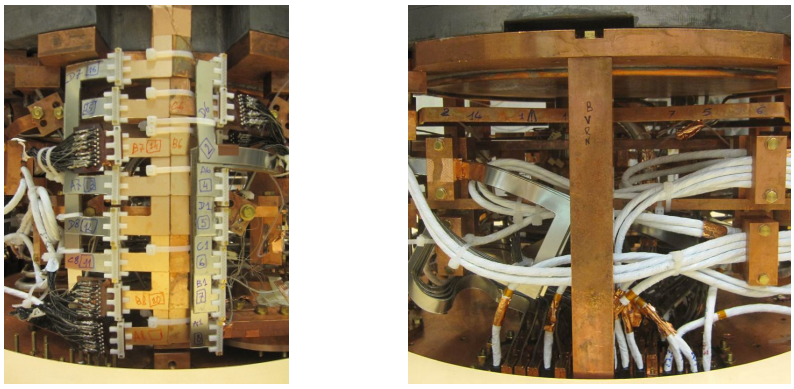


Figure 4.1: Selected cable connections inside the EDELWEISS-III cryostat: (left) the radio-pure copper cables join onto the stainless steel cables; (right) the stainless steel cables stops at 1.5 K. Coaxial cables (white) for the LUMINEU 0νββ-decay experiment and for certain FID detectors are also visible.

Based on such overall cabling arrangement, these two laminated cold cabling sections for EDELWEISS-III were then designed and produced at Oxford.

Because of the semi-flexible nature of the laminated cables, they can be fabricated as flat cables and then folded into different shapes. The cold cabling for EDELWEISS-III is first designed using CAD software (e.g. Autodesk Inventor

Professional) fitting to the 3D model of the EDELWEISS cryostat (Figure 4.2). In addition, the dimensions are also measured directly off the real cryostat where the 3D model is not representing reality well enough.

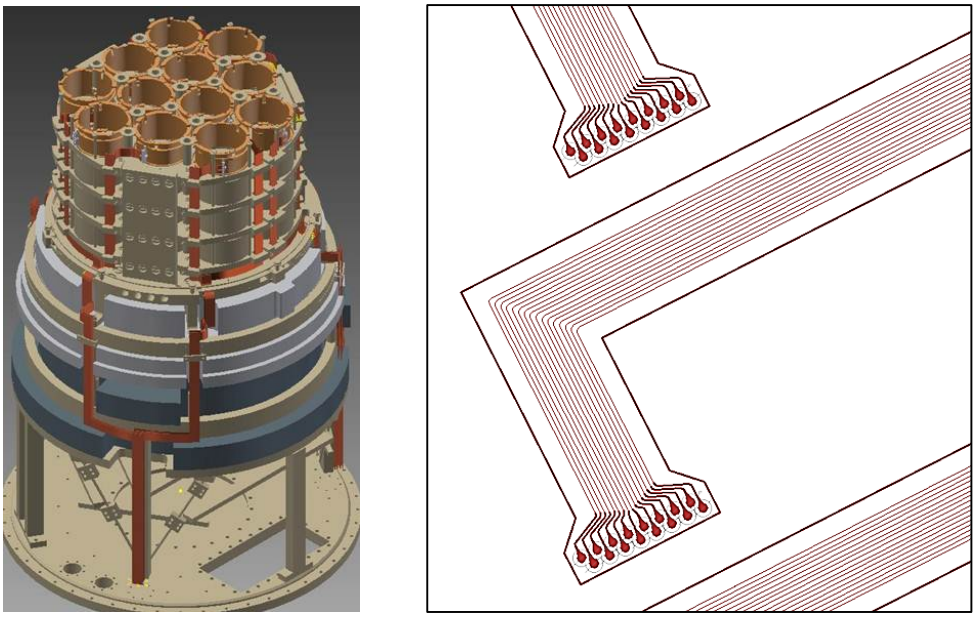


Figure 4.2: EDELWEISS copper cable CAD design: (left) 3D model in Autodesk Inventor Professional showing the cable shape and pathway design (orange) along with the inner EDELWEISS-III cryostat; (right) example of cable track design in EAGLE. The cable width is designed as 12 mm.

The corresponding dimensions of the flat shape for each position are then deduced using this 3D design. With these cable outline shapes, tracks are designed in a PCB layout design software (e.g. EAGLE) like in the example shown in Figure 4.2. After the flat cables are fabricated at Oxford as described in Section 3.1, they are delivered to LSM, folded as designed and installed onto the cryostat. Using this method, each position has its custom-made cable, which greatly reduces the material budget of the cabling and the time for its installation on site.

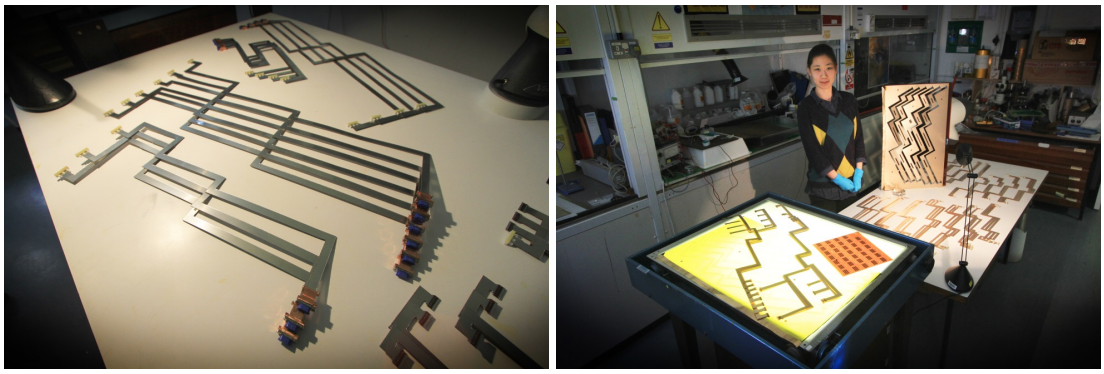


Figure 4.3: Finished cables before being delivered to EDELWEISS: (left) stainless steel cabling to span temperature stages from 1.5 K to 10 mK; (right) radio-pure copper cables near the detectors with low-background connectors. Overall, 48 copper cables (for all possible detector positions) and 28 stainless steel cables were delivered for installation on the EDELWEISS-III cryostat so far. In addition, one spare for each of the 16 shapes of copper cables were delivered and a few stainless steel cables.

Additional components designed for shielding connectors, adapting the Delrin connector to coaxial cables, heat-sinking the laminated cables, etc. are also produced and delivered.



Figure 4.4: EDELWEISS-III cryostat with detectors and the laminated semi-flexible cold cabling system installed.

After several prototype tests, the cabling solution was successfully delivered and installed on the EDELWEISS cryostat in early 2014. While the copper cabling is a success, there was an unexpected problem with the stainless steel cables during the first cryogenic run after the installation. This was surprising and disappointing, given that several earlier versions of stainless steel cable prototypes had been successfully operated in previous cryogenic runs in the Oxford cryostat as well as in the

EDELWEISS cryostat. As illustrated in Figure 4.5, it was established that the outer stainless steel layer of some cables delaminated in several places during the first cryogenic run with all cabling installed. This was traced to being caused by inferior properties of a new batch of what was supposed to be exactly the same material as was delivered for fabrication of the prototype cables. The lesson learnt from this is that for future batches of cables, additional test procedures will have to be implemented, as variation in quality of some raw material appears to be greater than suggested by the available documentation and certification papers.

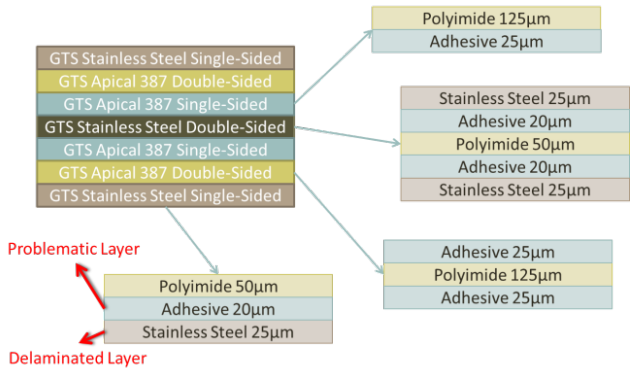


Figure 4.5: Illustration of which layer of the composite cabling delaminated during the first cooldown of the EDELWEISS cryostat.

Additionally, it was also suggested by the manufacturer that the moisture absorbed by the polyimide materials (typically about 1.5 % under normal room conditions) could also have evaporated into the adhesive layers and trapped there, which then make the peeling strength even worse. As no other adhesive layers (in all previous prototypes, final copper cables and the rest of the adhesive layers within the final stainless steel cables) have delaminated, this means the water vapour may weaken the bonding, but not enough to cause delamination if the raw material starts with a proper peeling strength. Nevertheless, this suggests that in the future, pre-drying the raw material before lamination should be considered.

After finding the problem, a solution was identified as shown in Figure 4.6. This method avoids the problematic interface within the commercially sourced material, and instead relies more on glue interfaces produced in-house at Oxford. Extensive tests of the repaired cabling, involving repeated temperature-cycling between room temperature and liquid nitrogen temperature, demonstrated the success of the repair. While all this was not the most desirable situation, it was very useful in confirming the advantages of having full control over the cable production procedures and that the features of the core of the cabling are robust enough to withstand even a repair (stripping down outer layers, re-gluing and re-heating in the process) as invasive as the one carried out by us.

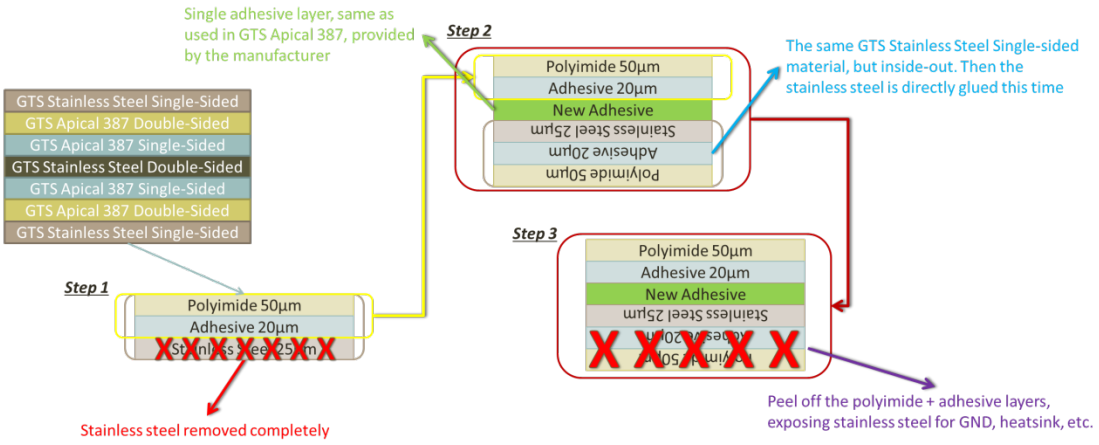


Figure 4.6: Illustration of cabling repair procedure.

4.2 Performance

As part of the readout system, the ultimate test of this laminated cabling system's performance is the quality of the final signal and the physics results. Although disentangling effects contributed by each aspect involved in the whole setup is difficult, it is possible to assess the performance of this semi-flexible laminated cold cabling system by comparing the results obtained with slightly different setups. In this section, the cabling performance will be demonstrated by referring to the noise

spectra and the detector baseline resolutions measured using readout systems equipped with the laminated cabling. The radioactive background induced by this cabling system in EDELWEISS-III will also be discussed.

4.2.1 Microphonic Noise and Noise Spectra

Being part of the readout system, the cabling should not introduce or pick up too much noise which could result in a worse energy resolution. As mentioned previously, the cabling system is laminated with two grounding metal layers on the outside to prevent electromagnetic noise from coupling to the signal tracks and to protect the cable from too much physical vibration which could introduce microphonic noise.

As mentioned previously, to test the cabling performance, several early batches of prototype cables produced in this work have been installed in the K400 cryostat at Oxford. They also contributed as part of the readout system development effort for prototype NTD-Ge based detectors. These prototypes all had both the copper and the stainless steel sections, transferring signals from the detectors up to the 120 K FET input stage of the readout electronics.

Figure 7 shows the noise spectra of such a system in one of the prototype runs. It is observed that excessive high frequency noise peaks between 1 kHz to 10 kHz appear when filling the cryostat's 1K pot in this run (Figure 7 (a)). These noise contributions are therefore associated with the vibrations caused by the filling of the 1K pot, which is actually a well-known source of microphonic noise in dilution refrigerators [90, 91, 92].

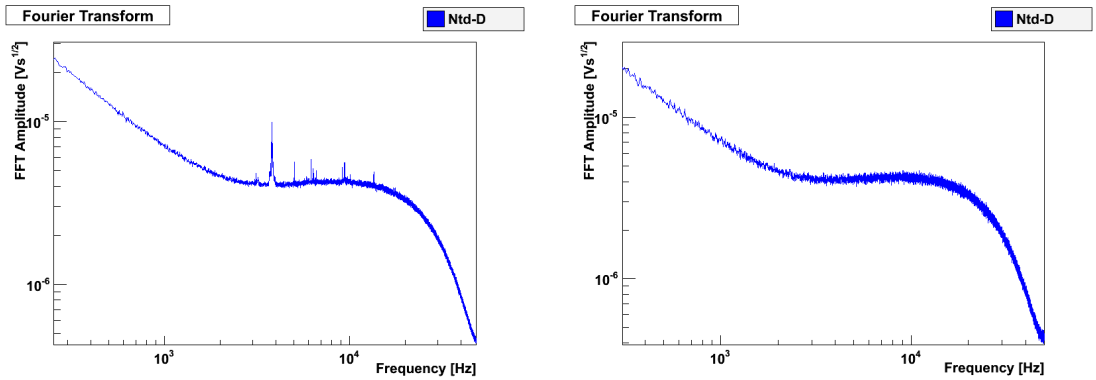


Figure 4.7: Noise spectra of a NTD-Ge phonon detector with the prototype cold cabling system in the K400 cryostat at Oxford: (a) 1K pot filling; (b) 1K pot not filling[2]. Both copper and stainless steel sections were installed.

As the Fourier spectrum represents the whole readout system, this noise could be picked up at the cold cabling system as well as any other point in the readout chain. One main suspect besides the cabling is the gold bond wires connecting the NTD-Ge sensor electrically to the laminated cabling and thermally to the heat bath. This hypothesis is tested by installing a 1 MΩ fixed resistor at the same level as the phonon detector and reading it out directly using another cabling channel in the same setup. In this way, the gold bond wires are eliminated while the rest of the readout chain remains the same. Figure 4.8 shows the noise spectrum for this 1 MΩ resistor with 1K pot filling. Apparently, the microphonic noise from 1K pot is not picked up for this setup. This indicates that the noise entered via the thin gold bond wires while the tracks in the laminated cabling system are well protected against it.

[2] Fourier transform for Figure 4.7 and Figure 4.8 was done by P. Coulter as part of his D.Phil thesis.

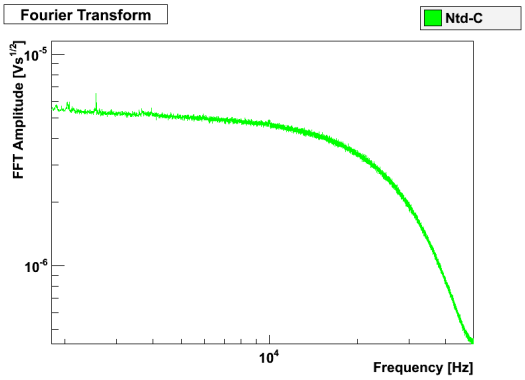


Figure 4.8: Noise spectrum of the 1 MΩ resistor read out via the prototype cabling system developed and installed in this work, while the 1K pot is filling.

Later batches of prototype were then designed for the EDELWEISS-III cryostat and tested in it. Three types of cold cabling configurations were installed at the same time in one commissioning run to compare their performances. These configurations are listed in Table 4.1.

Configuration	Temperature Level	Cabling Type
1	10 mK – 10 mK	Laminated semi-flexible copper cables
	10 mK – 1.5 K	Laminated semi-flexible stainless steel cables
2	10 mK – 10 mK	Laminated semi-flexible copper cables
	10 mK – 1.5 K	Coaxial cables
3	10 mK – 10 mK	Coaxial cables
	10 mK – 1.5 K	

Table 4.1: Three different cold cabling configurations installed in one commissioning run in the EDELWEISS-III cryostat.

Noise spectra of three FID detectors with these three different cabling configurations respectively are shown in Figure 4.9. The noise of all three configurations is at comparable levels, showing that no extra excess microphonic or external electromagnetic noise will be coupled into detector signals by using this two-section laminated semi-flexible cabling solution instead of the coaxial cables.

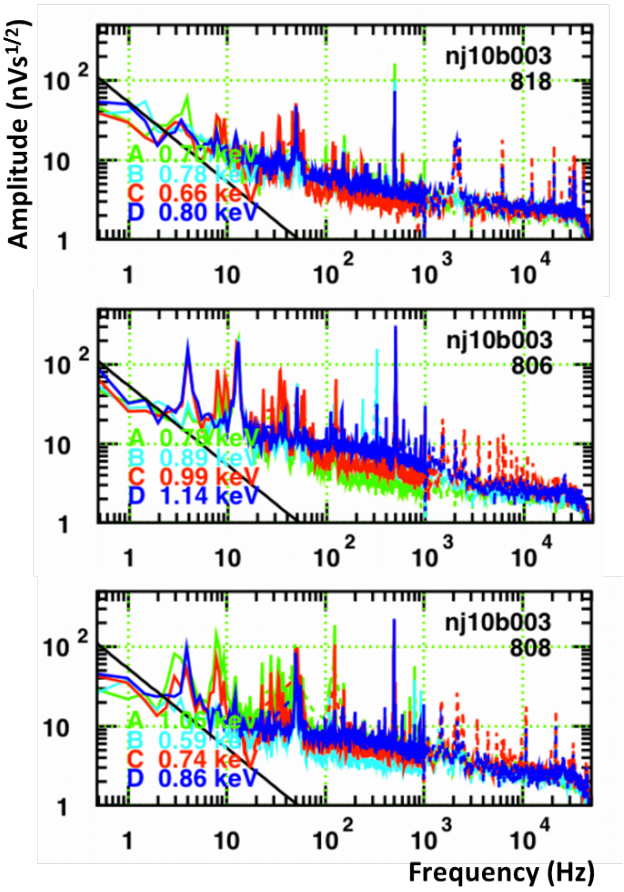


Figure 4.9: Noise spectra of three FID detector ionisation channels with different cold cabling configurations (Table 4.1) in one EDELWEISS commissioning run[3]: (top) laminated semi-flexible copper cable and stainless steel cable; (middle) laminated semi-flexible copper cable and coaxial cable; (bottom) coaxial cable only. The detectors were operated at 19 mK with fiducial electrode rings biased at ± 4 V.

4.2.2 Resolution with Different Cabling Setups

The detector resolution is limited by two factors: the statistical deviations of the detector signals for a given energy absorption, and the baseline fluctuation. The former only depends on the type of detector used while the latter is affected by the detector and read-out system setup. As the cabling configuration is one of the contributions to the baseline resolution, it can also be used to characterise the laminated cables' performance. With the same detector type, electronics and operating conditions, the baseline resolution of FID detectors equipped with the

[3] EDELWEISS collaboration meeting. Plots produced by J. Gascon.

laminated cabling system should at least be roughly the same as the ones equipped with coaxial cables.

Table 4.2 lists an example of three FID detectors' baseline resolutions in an EDELWEISS commissioning run. These detectors were read out by the three different cold cabling setups between 10 mK to 1.5 K as listed in Table 4.1.

Configuration	Baseline Resolution (keV)							
	Heat Channels			Ionisation Channels				
	A	B	Total	A	B	C	D	Total
1	0.71	1.1	0.68	1.0	0.89	1.2	1.0	1.0
2	0.55	0.90	0.50	0.87	1.2	1.6	1.4	1.1
3	1.0	1.7	0.89	1.6	0.78	1.2	0.85	1.0

Table 4.2: Baseline resolutions of three FID detector examples equipped with three different cold cabling configurations in one EDELWEISS commissioning run[4]. Detailed cabling setup of each configuration is listed in Table 4.1. The detectors were operated at 19 mK with fiducial electrode rings biased at ± 4 V.

In fact, the overall data from the EDELWEISS runs show no obvious differences in detector baseline resolutions caused by using different cold cabling configurations, which means using this laminated cabling solution does not degrade the detector performance.

4.2.3 Estimated Background in EDELWEISS-III Induced by Cold Cabling

With the radioactivity test results of selected materials, discussed in Section 3.2, simulations of gamma-rays and neutrons were carried out for the EDELWEISS-III setup. This is still an on-going study within the collaboration. Some preliminary results are shown here.

[4] EDELWEISS collaboration meeting. Presented by J. Gascon.

Table 4.3 shows the results of initial simulations assuming the section above shielding, which the crystals are directly exposed to, is equipped with the laminated semi-flexible copper cables.

Component	Material	Mass (kg)	Radioactivity in materials (mBq/kg)					Gammas (kg × days)$^{-1}$	Neutrons Events/year
			^{226}Ra	^{228}Th	^{210}Pb	^{40}K	^{60}Co		
Cables	Apical, Cu	0.2	26 ± 15	<50	346 ± 110	167 ± 126	<25	5–11	0.03–0.07
Connectors	Delrin, brass	0.056	32 ± 20	<53	11,000 ± 1000	680 ± 220	<36	1–8	0.02–0.06
Screws	Brass	0.1	4.9 ± 1.3	<3	<100	<40	<3	<1	<0.003
Screens, support	Cu	~500	<0.016	<0.012	–	<0.11	<0.018	<7	<0.01
Shielding	CH_2	~90	0.65 ± 0.08	0.30 ± 0.07	<3	<1	<0.06	7–14	0.03–0.06
Connectors	Al, resin	1.6	80 ± 9	158 ± 6	743 ± 48	129 ± 33	<4	0.2–0.3	0.3–0.5
Cables	PTFE	~1	<35	<28	190 ± 40	440 ± 110	<19	<1	<0.1
Cold electronics	PCB	0.23	7800 ± 500	12600 ± 1200	4500 ± 400	6500 ± 1200	<120	1–2	0.04–0.06
Warm electronics[a]	PCB	-	26,500 ± 1500	19,300 ± 1100	82,000 ± 5000	27,000 ± 3000	-	<1	0.3–0.5
Total								14–44	0.7–1.4

[a] Decay rates for warm electronics are given for the whole set (not in mBq/kg).

Table 4.3: Radioactive contaminations in materials of the EDELWEISS-III setup and their induced background estimation. The last two columns give the expected gamma-induced background in events/kg/day for 20 – 200keV and neutron-induced background in a year of running with 24kg of fiducial mass. The first five lines show materials placed close to crystals. The next three lines show those below the lead and polyethylene beneath the detectors. Taken from [69] (with permission from Elsevier).

In addition to the entries listed in Table 4.3, another less than 0.3 neutrons per year contribution is expected from components already present in EDELWEISS-II, such as lead shielding, stainless steel support structure, etc [69]. This makes the total expected neutron rate about 0.7 – 1.7 events per year of running.

In later studies, it is also noticed that the metal contacts in the sockets made of beryllium copper contribute more to the conductors' radioactive contamination level than the brass shells. Therefore, while the neutron background contribution from shells of Mill-Max pins and sockets is basically negligible, the contacts have a larger contribution than the previous estimation despite their tiny mass. This is mainly due to the (α, n) reaction of beryllium. The current simulation result is that for a setup with 42 detectors present and 17 (36) of them being active, the beryllium copper

contacts can contribute around 0.3 (0.5) out of the 0.73 (1.5) background neutron events[5] for one year of running.

The use of beryllium copper as socket contacts is motivated by its elasticity. This ensures the reliability of connections at the cryogenic temperatures where the connectors are located, which then in turn guarantees not losing detectors during a run because of the connectors.

Nevertheless, the overall radioactive background contribution of our cold cabling and connectors is compatible with the physics goals for EDELWEISS-III. As part of the new screening and material selection efforts of EDELWEISS-III, the contribution of radiogenic neutrons from materials inside the shielding has been lowered by an order of magnitude comparing to EDELWEISS-II.

Note that in the simulation, the coaxial cables containing fluorine are present only below the lead and polyethylene shielding, where the background contribution is largely suppressed. Even so, the expected neutron background upper limit induced by them is 0.1 events every year, which is potentially 1.4 – 3.3 times the contribution from the copper laminated cables positioned in vicinity of crystals.

This also indicates that the background in EDELWEISS can be further suppressed by extending our cabling system to the section below the PE and lead shielding, that is, using the stainless steel laminated cables to bridge between 10 mK and 1.5 K instead of the coaxial cables. Since the materials' radioactive contamination results are reported as upper limits, these levels are assumed to be the same for the coaxial cables and the stainless steel laminated cables when comparing the two. The main difference comes from the (α, n) reaction cross-sections, which is much higher for PTFE as discussed in Section 3.2.1. Using the same contamination levels in materials,

[5] Internal correspondence with M. De Jesus. The numbers are calculated with a cut of 20 – 200 keV recoil energy.

the neutron background contribution from 10 mK – 1.5 K stainless steel laminated cables is estimated to be about 50 times smaller than the contribution from equivalent coaxial cables[6].

4.3 Future Applications in EURECA and Other Rare Event Searches

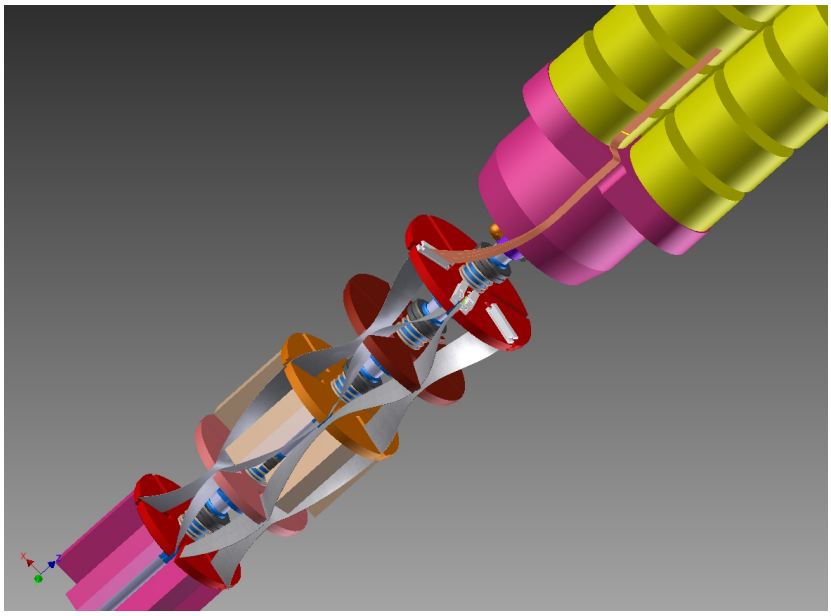


Figure 4.10: One preliminary two-section laminated semi-flexible cryogenic cabling arrangement suggestion for a EURECA detector tower.

As the future joint European effort to directly detect dark matter, the EURECA experiment has similar requirements discussed previously for its cabling system. In particular, with proposed 1 tonne target mass and 10^{-11} pb sensitivity, the cabling system for EURECA should be a negligible source of radioactive background. Also, the detector arrangement will be rather compact, thus the cables should have a small space budget. These are both the strong suits of the laminated cabling. The laminated semi-flexible cabling solution in EDELWEISS-III was intended as a prototype for EURECA. It is considered as one of the two cryogenic cabling solution candidates.

[6] Internal correspondence with V.A. Kudryavtsev and M. De Jesus.

Figure 4.10 shows an example of the preliminary cold cabling arrangement suggestion using the laminated copper and stainless steel cables.

Details of how to incorporate the laminated cabling system into the EURECA cryostat can be found in the EURECA Conceptual Design Report [70].

Besides reading out detector signals, this cabling system could also be used for infrastructure monitoring readout in other low-background experiments. For example, prototype cables with thermometers soldered onto it have been produced at Oxford for the LUX-ZEPLIN (LZ) experiment – another dark matter experiment using a liquid noble gas detector [35]. The prototype is a thermometer ladder, intended for installation along the height of the central cryostat, containing the xenon TPC. It is fabricated using the stainless steel laminate as raw material (Figure 4.11) since it will be in touch with multiple temperature levels and measure the temperature at these different points on the surface of the cryostat. Combined with the possibility of pre-defining the cable shape and its very low space budget, this solution (multiple thermometers on a laminated semi-flexible stainless steel cable) is ideal for when temperatures at multiple points have to be measured in a well-defined geometry.

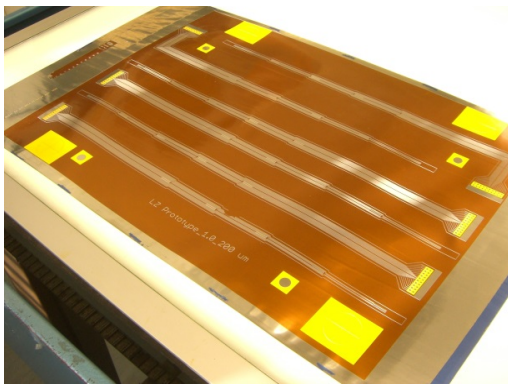


Figure 4.11: A signal track layer containing six LZ thermometer ladder prototypes.

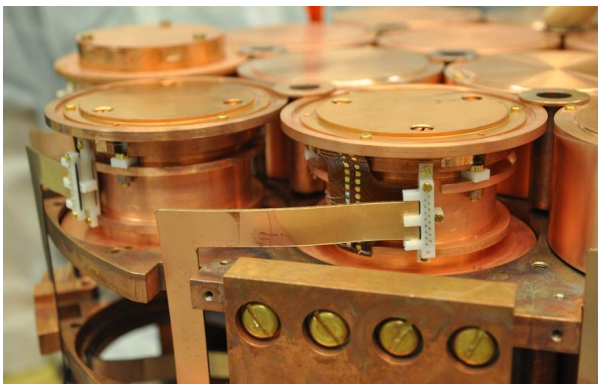


Figure 4.12: LUMINEU detectors equipped with the laminated semi-flexible copper cables.

In addition to dark matter direct detection experiments, this cabling solution is actually suitable for many other rare event searches such as neutrinoless double beta

decay experiments. Another example is the Luminescent Underground Molybdenum Investigation for NEUtrino mass and nature (LUMINEU) experiment [93], which is currently situated inside the EDELWEISS cryostat using a similar cold cabling configuration as the FID detectors. Figure 4.12 shows LUMINEU detectors read out with copper laminate cables supplied as part of this thesis.

5 Cryogenic Phonon-Scintillation Detector Development

As described in Chapter 1, one technique for direct mark matter detection is using cryogenic detectors that measure phonon and scintillation signals. One successful example is the CRESST experiment, using transition edge sensors (TES) as the sensing devices on their calorimeters. A large (300 g) calcium tungstate crystal is equipped with a TES to work as the phonon detector, measuring the energy deposited by particle interactions. For detecting scintillation, a similar calorimeter, modified for detecting the small energy carried by the scintillation light, is used. Such a detector gives excellent resolution. However, it also requires to be stabilised at a specific operating temperature which normally varies across different detector modules. Further, it appears that reliable and stable production of a large quantity of such detectors is a challenge. But this is required by the next generation of dark matter direct detection experiments. Motivated by this, a series of efforts have been put into developing an alternative solution of light detectors for the next generation of dark matter direct detection and other low background rare event searches.

This chapter will first describe the general setup of prototype detector modules developed as part of this thesis. It will then move on to discussing configurations and properties of individual components in detail. Here, the components are separated into three major parts – the target crystal, the phonon detector and the light detector. They will be discussed in sections 5.2, 5.3 and 5.4 respectively.

5.1 Detector Setup

To give a complete overview on how the detector modules are constructed, this section mainly focuses on the overall detector layout and the involved infrastructure.

5.1.1 Detector Module Layout

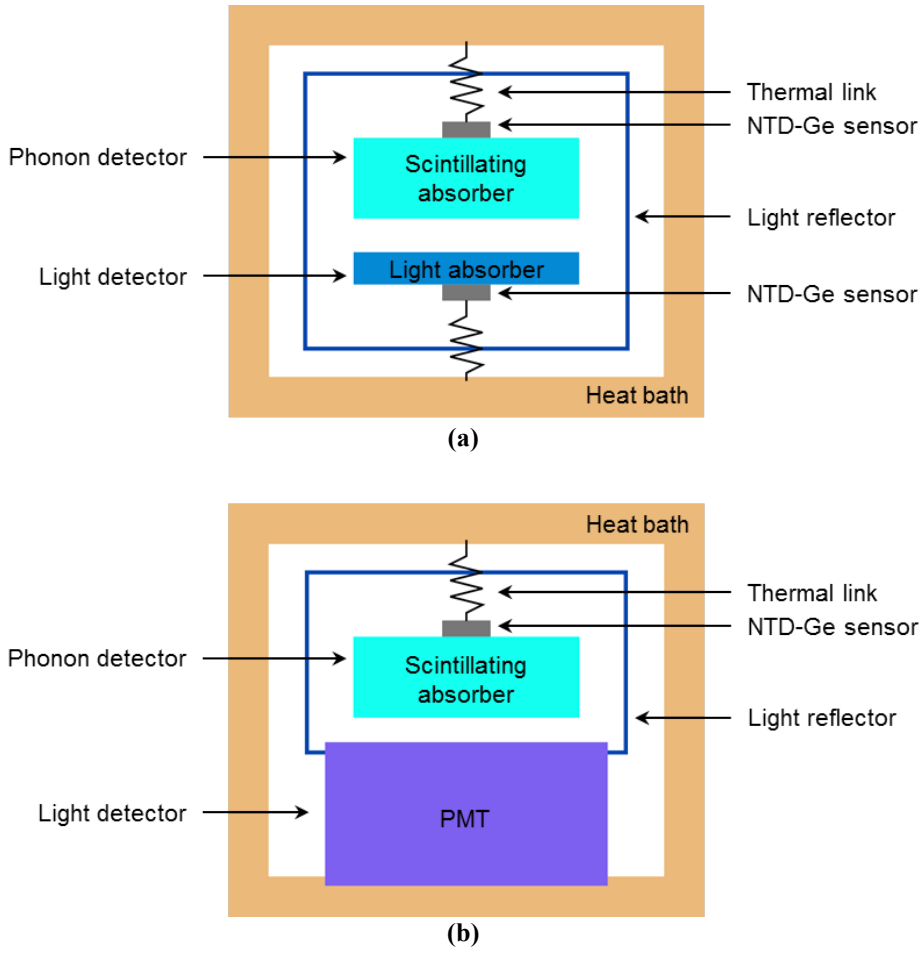


Figure 5.1: Schematic views of two different detector module configurations: (a) previous design where the light detector is made of a light absorber and a NTD-Ge thermometer; (b) current version (this thesis) using a cryogenic PMT as the light detector.

Simultaneously measuring phonon and light signals, the module comprises two separate cryogenic detectors (Figure 5.1). The primary phonon detector is a NTD-Ge sensor glued to a scintillating crystal target. When an incident particle deposits energy in the target crystal, it will have a small temperature rise, which is measured by the

NTD-Ge sensor. Concurrently, the crystal will give out scintillation light, which is confined by highly reflecting foils around the detectors and eventually will be absorbed by the light detector.

Two different designs of a light detector have been developed. The first one was based on a similar setup as the phonon detector – a crystal is used as absorber with an NTD-Ge sensor glued on top of it as shown in Figure 5.1 (a). After a series of tests with such a light detector, the results suggested that the sensitivity of this kind of detector will be severely limited by its heat capacity, with the NTD-Ge sensor actually being the dominant contributor [94] of it.

Consequently, the NTD-Ge based light detector is replaced by a low-temperature photomultiplier tube (PMT) as shown in Figure 5.1 (b). The advantage of using a low-temperature PMT as the cryogenic light detector and its performance will be discussed in Section 5.4 and the following chapter.

Phonon Detector

The layout of the phonon detector is shown in Figure 5.2. For the phonon detector, the absorber used is a calcium molybdate crystal. Limited by the small space in the available K400 cryostat and the high radioactive background in the laboratory above ground, this crystal is relatively small with dimensions 10 mm × 10 mm × 5 mm.

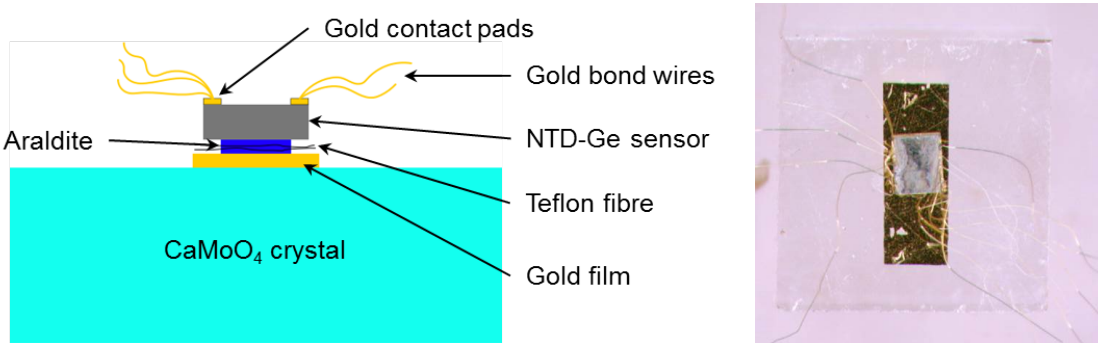


Figure 5.2: Phonon detector layout: schematic of the side view (left) and microscope photo of the top view (right). The dimensions of different components are described in text as well as listed in Table 5.1.

A 250 nm thick gold film with an area of 2.2 mm × 6.2 mm is evaporated onto the top of the crystal to help collect phonons and thermalise them. The NTD-Ge sensor is then glued onto this gold film with a small amount of Araldite adhesive. A Teflon fibre is placed in the adhesive between the NTD-Ge sensor and the gold film. This is to prevent the NTD-Ge sensor from making direct contact with the gold film, which would electrically short the NTD-Ge sensor.

After a particle interaction depositing energy in the target crystal, this energy is converted to athermal phonons initially. Most of them will then down-convert to thermal phonons [95, 96], and eventually cause a temperature rise of the crystal, the gold film and the NTD-Ge sensor glued to it. This temperature rise is measured as a change of resistance of the sensor.

On top of the sensor are two gold contact pads on the two opposite edges, with a couple of gold bond wires attached to them. A small printed circuit board (PCB) close to the target crystal provides landing pads for the gold bond wires, connecting them to a connector for the resistance readout cable (visible in Figure 5.4). From here, the signal is carried by laminated semi-flexible cabling to the front-end readout electronics (Figure 3.12). These gold bond wires also act as the thermal link as shown in Figure 5.1. They connect the phonon detector and the detector holder via the PCB. Since the copper detector holder is also the heat bath (Section 5.1.2), the absorber and the sensor can then return to their operating temperature after an energy deposition.

Light Detector

In the current setup, a Hamamatsu R8520-06-PT-UK 10-stage Bialkali low temperature PMT is used as the light detector. It faces the scintillating calcium molybdate crystal without any contact and is powered by a Cockcroft-Walton high

voltage generator (CWG) thermalised to the Still (~700 mK) of the K400 dilution refrigerator. The setup is shown in Figure 5.3.

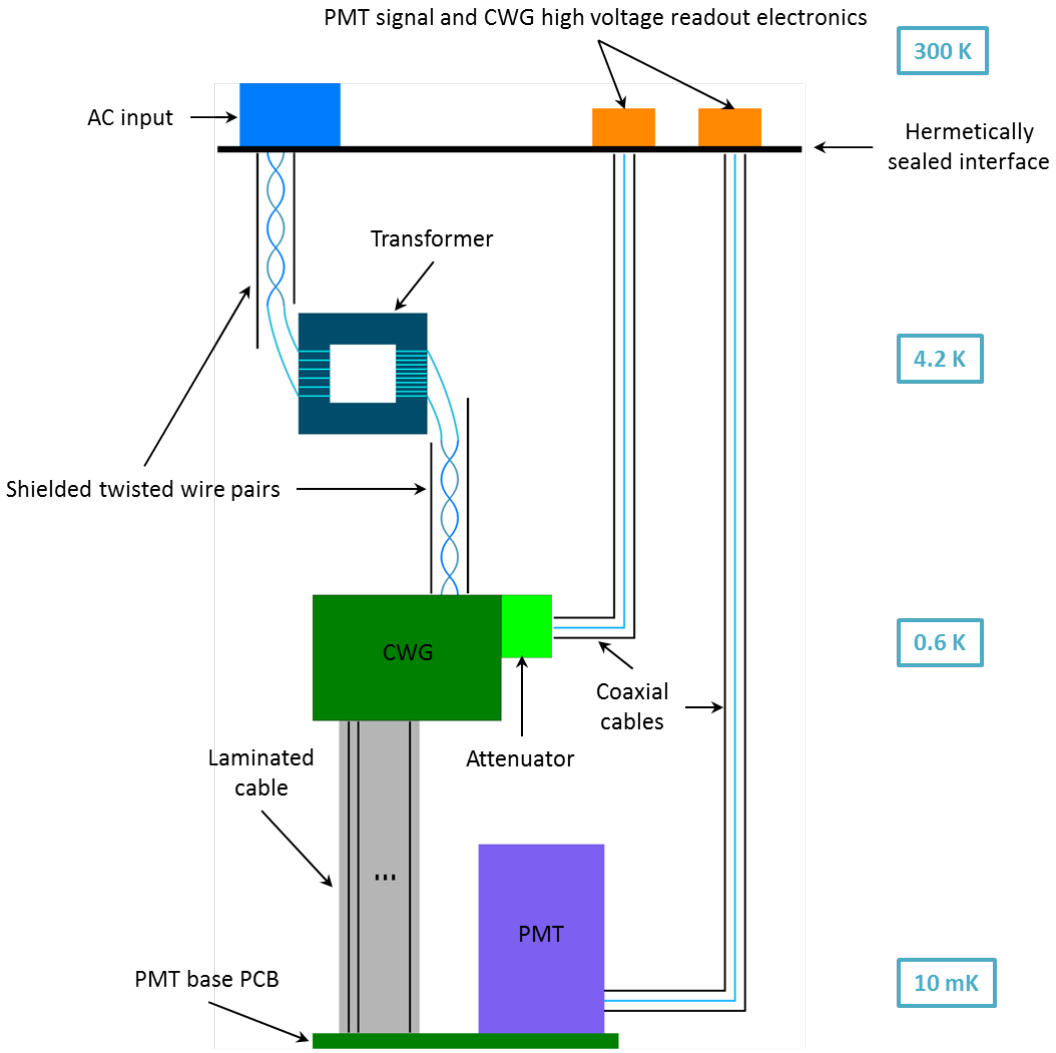


Figure 5.3: Schematic of the light detector setup. The temperatures given in the blue boxes on the right are indications of the different temperature levels that relevant components are heat anchored to. They are only indicative and do not represent exact, measured values. A detailed discussion of the typical temperature levels in a dilution refrigerator can be found in Section 3.4.1.

The PMT is plugged into metal sockets mounted on a base PCB. Its cathode, dynodes and anode are then individually connected to different stages of the CWG through the PCB and a stainless steel laminated semi-flexible cable. The PMT signal is carried by a coaxial cable all the way up to the readout electronics outside the cryostat.

To drive the CWG, a function generator positioned outside the cryostat provides a small AC driving voltage. This voltage is then amplified by a transformer at 4.2 K and fed to the CWG through twisted wire pairs inside ground shielding. Additionally, to monitor the generated high voltage, it is recorded by electronics at room temperature in parallel. An attenuator, consisting of a 1 MΩ and a 1 GΩ (room temperature values) resistor, is mounted on the CWG PCB between the highest voltage stage and monitoring cable.

By using the capacitive CWG to deliver the various voltages directly to the cathode, anode and dynodes, instead of the resistive voltage divider, the heat dissipation from the high voltage generation is thus minimised, allowing the cryostat to be cooled down. Meanwhile, the high voltage only appears in the region between the CWG and the PMT in this setup, so no special high voltage measurement equipment is required and the possibility of sparking between the high voltage monitoring wire and the grounding can also be largely avoided.

5.1.2 Detector Housing

The detector housing is made of copper since it can be manufactured with very high purity, making it relatively radiopure. Copper also conducts heat very well, resulting in the temperature across the detector housing being relatively uniform. However, one caveat is that at temperatures below 20 mK copper could have heat leaks, which prevents cooling down to the base temperature, unless NOSV copper or other specially treated (annealed) copper is used. This is caused by the ortho-para conversion of hydrogen precipitated into bubbles in copper, which happens at a rate of about 2% / h, and releases heat [97]. NOSV copper is of a very high purity degree and low hydrogen concentration. The heat leak can be thus prevented by using NOSV copper for the detector housing.

The basic function of the detector housing is to provide mechanical support of the detectors. In addition, the housing of our cryogenic detector module is actually designed to also provide several other functions that contribute to a better detector performance. Its functions and design considerations are discussed below and then the final design incorporating these considerations is presented.

Mechanical Support

As mentioned earlier, the first function of the detector housing is to physically hold the detectors in place. To achieve this properly, the following requirements need to be considered:

- The holding mechanism should be firm enough to avoid extra noise introduced by vibration. But it cannot be too tight either. For example, the scintillating crystal could suffer from cracks or defects otherwise. Thermal contraction rates of different materials during cooling should also be considered.
- For the phonon detector, another important requirement is that the target crystal holding structures need to be thermally insulating so that the gold bond wires will be the only thermal link.
- For the light detector, electrical insulations between the electrically grounded housing and the pins connecting dynodes and anode should be carefully arranged to avoid any high voltage breakdown.

Figure 5.4 shows the holding mechanism of the phonon detector. To reduce the risk of introducing noise induced by the relative vibration between the crystal and its holding structures or damaging the crystal, loops of soft material are used in the final design instead of solid clamps. In the current setup, the $CaMoO_4$ crystal is suspended

within the housing by two nylon fibres at either end as shown in Figure 5.4. The tension of each fibre is kept and adjusted by a pair of screws.

Nylon is also a good thermal insulator as required by the phonon detector.

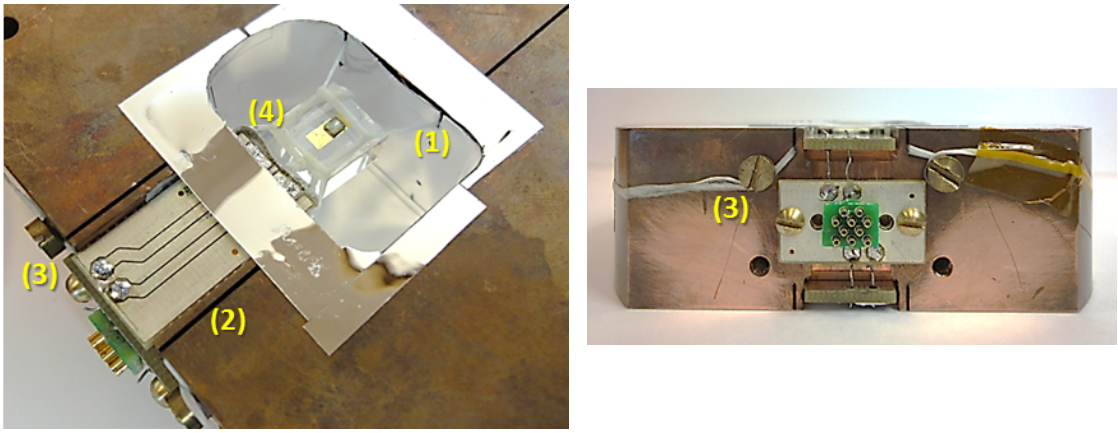


Figure 5.4: Holding mechanism of the phonon detector: top view (left) and side view (right). The target crystal is suspended by two nylon fibres (1) looped around the two sides. The fibres are then fitted into four groves (2) and wrapped around four screws (3). The tension of these two fibres can be adjusted by turning the screws. As the width of the crystal is smaller than the separation of the groves, two extra nylon rings (4) are used to keep (1) from sliding off.

As for the PMT, it is installed on top of the base PCB with its photocathode facing up while the PCB is firmly clamped to the housing by four screws, as shown in Figure 5.5.

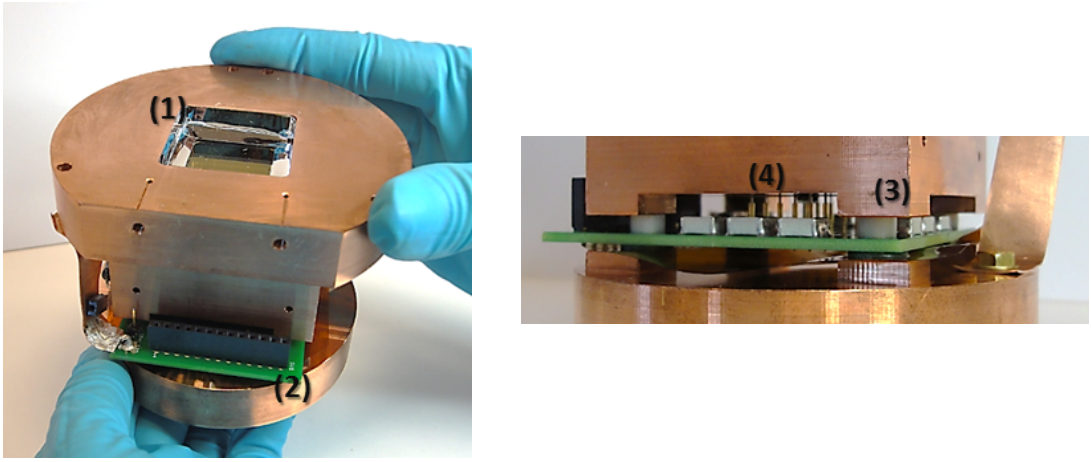


Figure 5.5: The light detector holding mechanism: (left) the complete light detector with PMT (1) and its PCB base (2); (right) details of the bottom part. The PCB is sandwiched between two copper pieces, which is fixed by four screws on the corners (3). The PMT is fitted to the PCB using Mill-Max sockets (4), which provide grip strong enough to keep the PMT in place.

To prevent the PMT wall being squeezed by the copper housing at low temperature, there is a ~2 mm gap left in between. The total linear contraction from

room temperature is defined as $\Delta L/L \equiv (L_{293K} - L_T)/L_{293K}$, and for copper, $\Delta L/L$ at 4 K is 0.324% [83]. Estimating using these numbers, the 2 mm gap is a very safe value.

To address the last requirement concerning insulation, the copper top and bottom pieces are separated from the PCB by PTFE spacers to make sure that nothing with non-zero voltage is in the vicinity of electrical grounding. Further, a kapton sheet is added below the PCB to further ensure optimum insulation.

Light Reflector

In Figure 5.4 and Figure 5.5, several patches of reflecting foil can be seen at places like around the target crystal and on top of the PMT window. The reflecting foils are attached to the detector housing and form a cavity that contains most of the scintillation light until it reaches the PMT window to be detected. The foil used is VM2000 radiant light film manufactured by 3M [98]. It has > 98% reflectivity for light of wavelength between 400 nm and 700 nm, which matches the scintillation light produced by $CaMoO_4$ quite well.

Shielding

At Oxford, this prototype detector module is operated in a laboratory above ground instead of in an underground laboratory with sufficient shielding as is the case for real dark matter detection experiments. Proper shielding against natural radioactive background then becomes even more important. Even though the prototype is only being tested using a radioactive source, the natural radioactivity could still contribute a large background count. This will cause pile-ups with particles that are actually from the test source, compromising the signal quality since it is very difficult to extract the energy of each pulse accurately. Too much natural radioactivity

also means the NTD-Ge sensor's temperature changes a lot, making it even more difficult to stabilise the phonon detector.

The layer structure of cryostats can shield some of the external background. But some background radiation can also come from sources closer to the detectors. To sufficiently attenuate the excessive background, internal shielding just around the detectors is necessary. Considering the limited space, the detector housing is also designed to be the inner layer of shielding.

Alpha and beta particles will not contribute much cause for concern since they will lose their kinetic energy and eventually come to rest relatively quickly while traveling in a medium. Figure 5.6 shows the ranges of alpha and beta particles in aluminium (some cryostat walls), and copper (some cryostat walls and the detector housing).

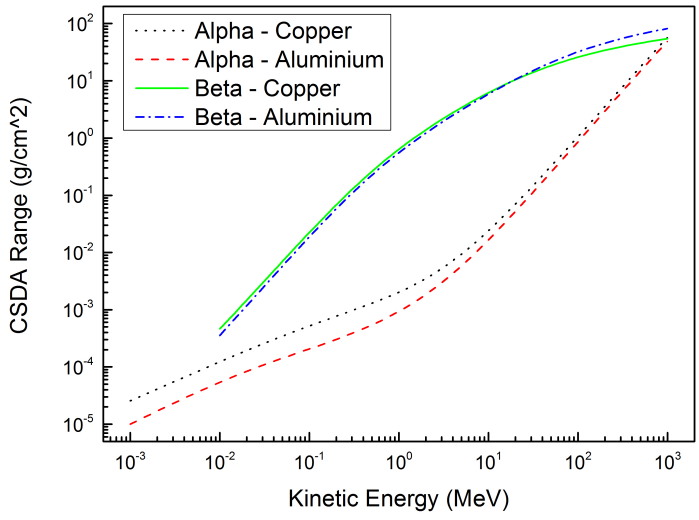


Figure 5.6: The continuous slowing down approximation (CSDA) ranges of alpha and beta particles in copper and aluminium respectively. The data are taken from NIST ASTAR and ESTAR database [99].

Here the particle range is defined as the distance of material traversed multiplied by the density of material. If using densities of 8.96 g/cm^3 and 2.70 g/cm^3 for copper and aluminium respectively (20 °C, 1 atm), 5 MeV alphas can be stopped within a

few tens of micrometre metal, and 0.7 mm copper or 2.1 mm aluminium is enough for stopping even 1 MeV betas.

Therefore, for the detector housing, the attenuation of gamma particles is the main consideration as they are more penetrating. Gamma rays interact with matter in three primary ways:

a) By the photoelectric effect – a photon interacts with an atom resulting in an electron ejected as photoelectron.
b) By the Compton scattering – photons scattered by electrons transferring a portion of energy in the process.
c) By pair production – a high energy photon transforms into an electron-positron pair.

Attenuation by the photoelectric effect is the most effective of these three processes as the full energy of photon will be absorbed in it. Combining the three, the total effect can be described using a linear attenuation coefficient μ. When gamma-rays of intensity I_0 are incident on a material of thickness L, the intensity I transmitted is given by an exponential relation:

$$I = I_0 e^{-\mu L} . \quad \textbf{(5.1)}$$

μ depends on the gamma-ray energy and the atomic number Z and density ρ of the absorbing material. Due to its dependence of density ρ, the linear attenuation coefficient will be different for different forms of the same material. Therefore, it can be converted to the more commonly used mass attenuation coefficient, μ/ρ. Figure 5.7 shows the mass attenuation coefficient of copper.

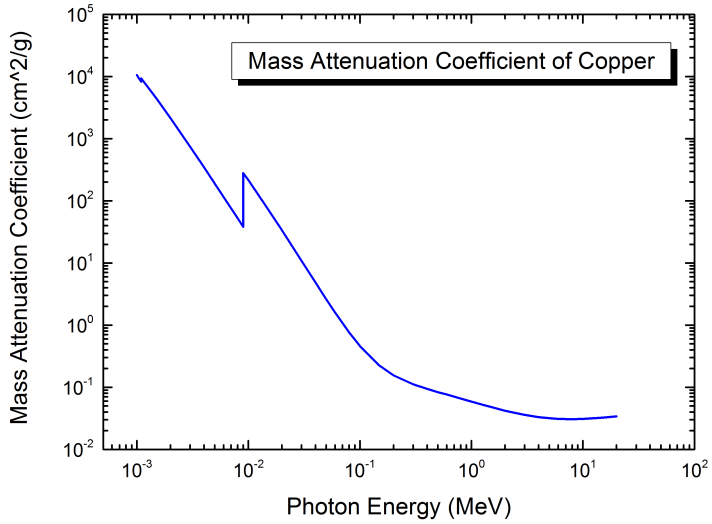


Figure 5.7: The mass attenuation coefficient of copper. The discontinuity is due to the absorption edge of copper, which happens when the gamma-ray energy is just above the binding energy of electron of a certain shell. Data are taken from NIST X-ray Attenuation Database [100].

According to these data, to reduce the intensity of a 200 keV gamma-ray beam to 10% of its incident intensity requires about 1.65 cm copper.

Considering the attenuation effect and the available space, the detector housing wall thickness is kept as 15 mm or more in the final design where necessary and possible.

To further improve the shielding, extra external shielding outside the cryostat can be added. In fact, the attenuation is more efficient for high-Z materials as the possibilities of scattering the photons tend to increase. For example, if using lead (Z = 82) as the absorber, to reduce the intensity of a 200 keV gamma-ray beam to 10% of its incident intensity requires only about 0.203 cm thickness (data from [100]). Hence, although lead is not suitable for making the detector housing, it is a very good material for the external shielding.

Heat Bath

The detector housing also acts as the heat bath to allow the temperature of the detector module to return to the set operating temperature after a particle interaction. Therefore, it is crucial that the detector housing has a stable temperature itself. Assuming the heat capacity and temperature of the heat bath is C_{bath} and T_{bath} respectively, the thermal conductivity between the heat bath and upper level (e.g. mixing chamber) is K_{ub} and the temperature of the upper level is T_{upp}, then the heat flow can be described as:

$$C_{bath}\frac{dT_{bath}}{dt} + K_{ub}\left(T_{bath} - T_{upp}\right) = 0\,. \tag{5.2}$$

Therefore,

$$T_{bath} = \left(T_{bath0} - T_{upp}\right)\cdot e^{-t\cdot K_{ub}/C_{bath}} + T_{upp}\,, \tag{5.3}$$

where T_{bath0} is the original temperature of the heat bath.

Equation (5.3) shows that the temperature response of the heat bath to the fluctuation from other components is exponential with a time constant C_{bath}/K_{ub}. Thus, to keep this response slow, a large heat capacity of the detector housing is required, which means its mass should also be large.

Since the thickness of the detector housing walls is decided to be mostly larger than 15 mm to give enough shielding, its mass is already large enough to provide a relatively stable baseline temperature.

Final Design

Taking all these aspects into consideration, the final version of the detector housing comprises four copper parts as shown in Figure 5.8.

The part holding the target crystal and NTD-Ge sensor is roughly a cylinder (diameter = 86 mm; height = 25 mm) with a square cavity in the centre (20 mm × 30

mm) to place the phonon detector. One side of the round surface is machined away to accommodate a PCB and connectors to the readout cabling, while the opposite side has a 5 mm × 10 mm opening for the radiation from the test source to pass through. There are also several holes and grooves for pumping, bolting the PCBs, holding the nylon strings, etc.

Below this is the part shielding the PMT. The diameter of the cylinder part is also 86 mm. To prevent the detector module from being too heavy for the cryostat or the brass rods holding it, only the upper 15 mm of the cylinder is kept with one side machined flat allowing cables to pass. The lower 25 mm is machined into a rectangular cuboid with a cross-section of 50 mm × 50 mm. In the centre, there is a 30 mm × 30 mm cavity to place the PMT. Again, holes and opening are added for pumping, bolting, etc.

The housing is completed with a 10 mm top plate (diameter = 86 mm) and a 15 mm bottom plate (diameter = 74 mm) for shielding. The top plate is thinner because there is the whole cryostat above acting as extra shielding. The bottom plate has a smaller diameter but enough for preventing any direct path into the detector cavity.

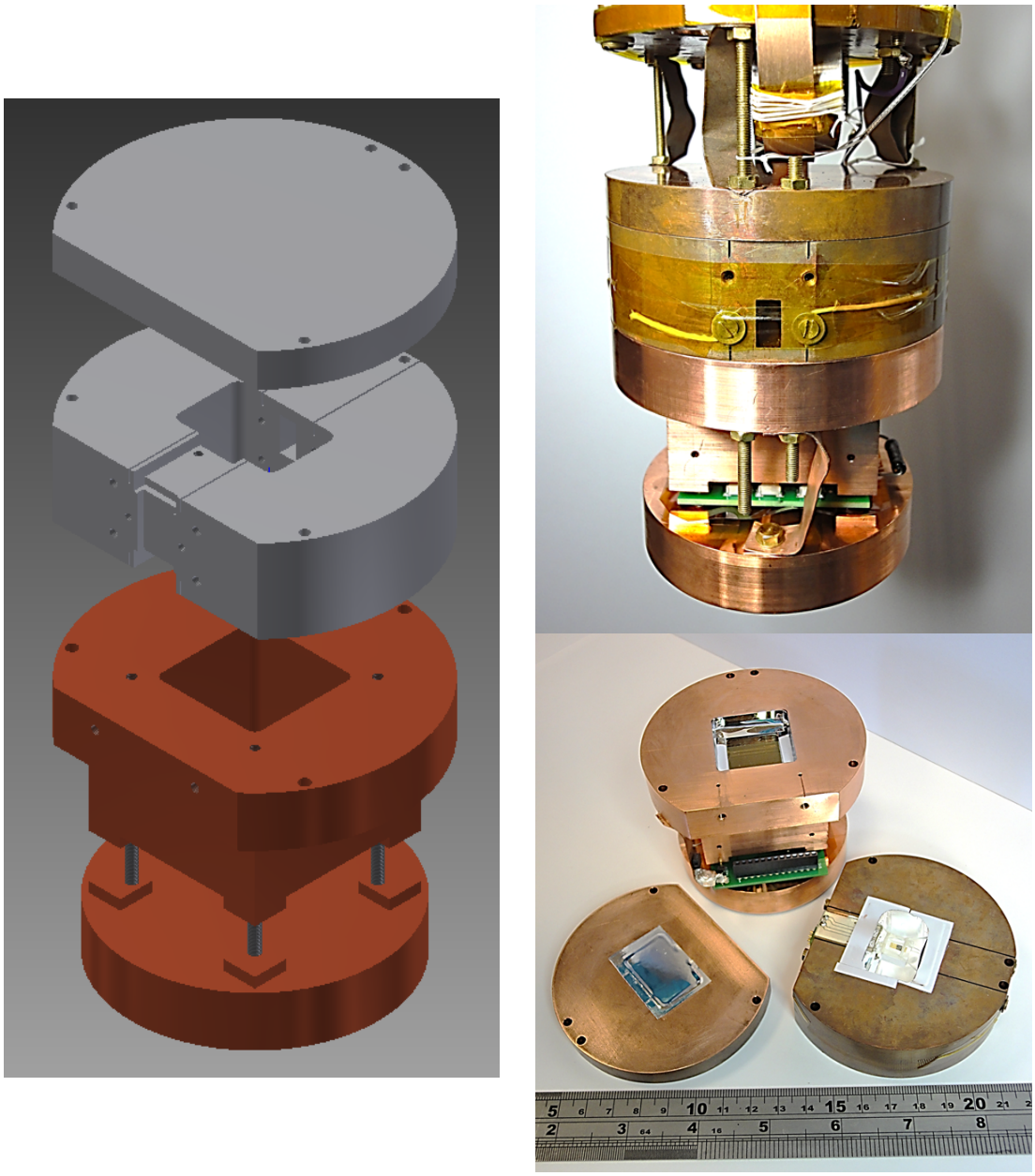


Figure 5.8: Final detector housing design: (left) CAD drawing of the detector housing; (top right) complete detector module mounted in the K400 cryostat; (bottom right) detector housing separated into three parts with phonon and light detectors installed.

After assembling, the prototype detectors are mounted and tested in an Oxford Instrument Kelvinox 400 dilution refrigerator as described in Section 3.4.1.

5.2 Target Crystal – Scintillator

As discussed in Section 1.4.1, for the purpose of dark matter direct detection, the scintillator chosen should have nuclei of a high atomic mass. For example, the molybdenum nuclei in the calcium molybdate ($CaMoO_4$) crystal make it suitable for

dark matter detection detectors. And to keep the radioactive background low, the crystal itself should have a low radioactivity level and not contain nuclei with high (alpha, n) cross-section.

As the scintillation light input to the light detector is produced by the target crystal, high light yield at cryogenic temperature is another obvious requirement. The scintillation properties of $CaMoO_4$ (as well as many other scintillators from the tungstate and molybdate family) have been studied over a range of temperatures above 7 K.

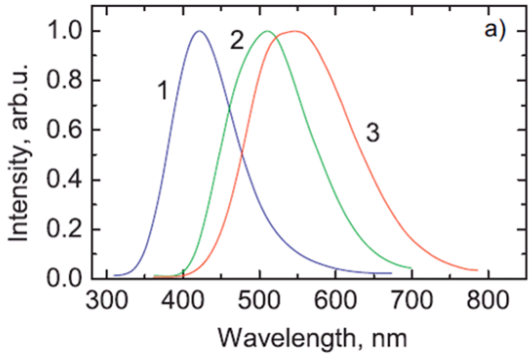


Figure 5.9: Luminescence spectra of some crystal materials potentially suitable for cryogenic phonon-scintillation detectors, including $CaWO_4$ (1), $ZnWO_4$ (2) and $CaMoO_4$ (3) measured at T = 8 K for excitation with 31 eV VUV photons. Plots taken from [101] (with permission from John Wiley and Sons).

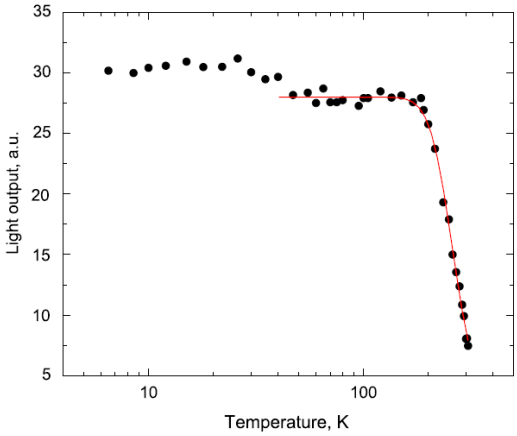


Figure 5.10: Temperature dependence of the $CaMoO_4$ scintillation light yield measured with α-particles from ^{241}Am. Plot taken from [102] (with permission from Elsevier).

At 8 K, $CaMoO_4$ gives a broad band emission with a peak at around 540 nm as shown in Figure 5.9. It is estimated that the room temperature light yield of $CaMoO_4$ is about 8900 ± 3500 ph/MeV [102, 103]. The light output first increases rapidly when the temperature decreases, and then it stays relatively stable at temperatures below 100 K (Figure 5.10). At 9K, the light yield of $CaMoO_4$ is around 3 times that of the room temperature value [101], which makes it more suitable for cryogenic applications. Apparently our prototype detector is operated at a much lower temperature, but these results could still be applied since there is no evidence showing

the light output will change significantly at low temperatures [101, 102]. These values are useful for estimating the light collection efficiency and the resolution of the light detector in later sections.

At room temperature, the principal scintillation decay time of calcium molybdate is about 16 μs. This value increases under cooling. As an example, at 9 K, the principal decay time of $CaMoO_4$ becomes about 380 μs [101]. This may be too slow for some applications, but it will not be a problem for rare event searches like dark matter detection. Figure 5.11 shows some scintillation decay curves of $CaMoO_4$ at different temperatures. The decay curve typically has a fast component and a principal slow component. The temperature dependence of these two components down to ~7 K is also shown in Figure 5.11.

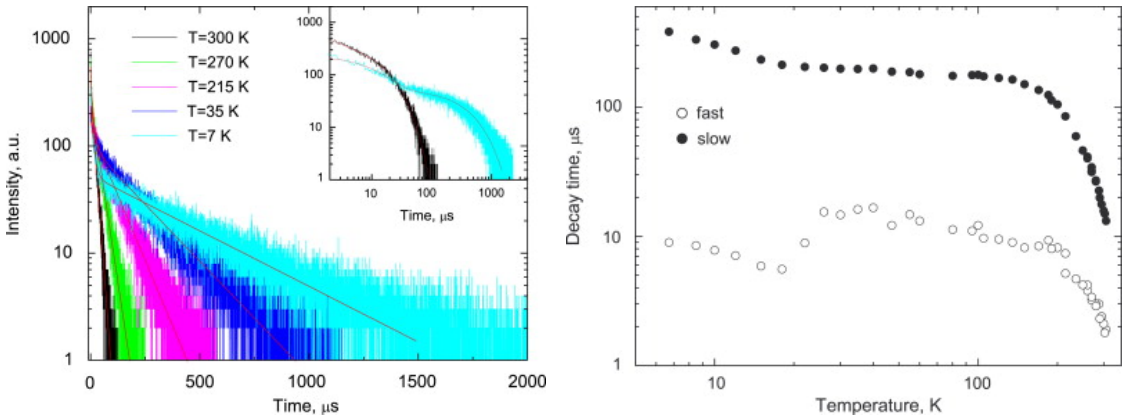


Figure 5.11: Decay time of $CaMoO_4$: (left) Scintillation decay curves measured at different temperatures. Decay curves at 7 and 300 K in log–log scale are shown in the upper right corner; (right) Temperature dependence of the scintillation decay time constants excited by α-particles from ^{241}Am. Open and solid dots represent the fast and the slow component, respectively. Plots taken from [102] (with permission from Elsevier).

According to these data points, the decay constant still has a tendency of increasing at lower temperatures, so the value measured at 7 K cannot be applied to our operating temperature. In fact, the test of our detector module also provides an excellent opportunity to study the decay time of $CaMoO_4$ at milli-Kelvin temperatures and one of the results from our tests is the temperature dependence of the decay time constant below 7 K, which will be discussed in the next chapter.

The $CaMoO_4$ crystal used here was produced using the Chochralski technique at the Institute of Materials SRC "Carat", Ukraine from $CaCO_3$ (99.998%) and MoO_3 (99.995%) raw materials [104, 102].

5.3 Heat Channel – NTD-Ge Sensor

As mentioned before, the phonon / heat detector is realised by using a sensor made of neutron-transmutation-doped (NTD) germanium. Its resistance increases as it is cooled, making it suitable to be used as a thermometer for cryogenic detectors. Like many other thermometers, a NTD-Ge sensor is operated at a stabilised base temperature. But because its temperature dependence is continuous, this operating temperature can be chosen over a relatively large range, allowing it to be more reliable and flexible in applications.

This section will mainly focus on properties of the phonon / heat detector and its major components.

5.3.1 Resistance of the NTD-Ge Sensor

NTD germanium is produced by irradiating germanium with a flux of thermal neutrons in a nuclear reactor. Germanium isotopes produced after capturing neutrons will then decay into gallium (major impurities), arsenic, and selenium, making the germanium p-type. The impurity distribution from neutron transmutation doping has a high homogeneity because the neutron capture cross section is rather small. The doping can also be precisely controlled as the concentration of impurities is proportional to the exposure time given a constant neutron flux [105, 106].

In lightly-doped germanium, shallow impurities have typical binding energies of tens of milli-electron volts and are almost completely ionised at room temperature. The ionised fraction drops when the material is cooled and thus the resistance

increases. At cryogenic temperatures where the detectors are operated, this thermal ionisation of impurities is negligible. The dominant conduction mechanism is called variable range hopping. If the doping is below a critical density below which the conductivity goes to zero at zero temperature (found by Anderson [107], Mott and Twose [108]), charge transport takes place by phonon-assisted tunnelling between impurity sites. The energy difference required by the "hop" is made up by absorption or emission of a phonon of the required energy. At lower temperatures, longer hops are favoured to find an unoccupied site with a sufficiently close energy to the original site due to the lack of high energy phonons [109]. For variable range hopping, the resistance is expected to be

$$R(T) = R_0 \exp\left(\frac{T_0}{T}\right)^p, \tag{5.4}$$

where R_0, T_0 and p are constant.

In the theory by Mott, p is 1/4. Later, Efros and Shklovskii introduced the effect of Coulomb gap (a gap in the density of states near the Fermi level created by the Coulomb interaction between localized electrons), which modified the result to make p become 1/2 [110]. R_0 and T_0 depend on the intrinsic properties of the crystal and the doping level.



Figure 5.12: NTD-Ge sensor used in the phonon detector.

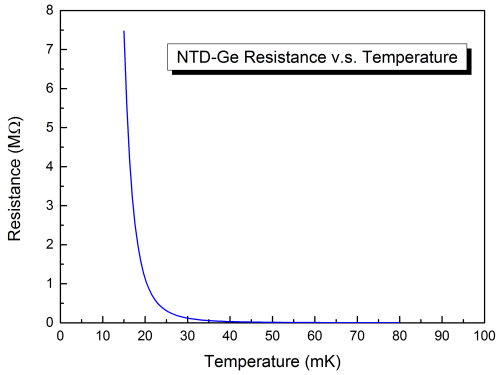


Figure 5.13: Resistance v.s. temperature curve of NTD K.

For the current phonon detector setup, NTD K (Figure 5.12) with dimensions 1.5mm × 1.5mm × 0.5mm is used. A generic calibration gives T_0 = 2.99 K, and R_0 = 5.52 Ω for this sensor. Its resistance against temperature curve is shown in Figure 5.13.

5.3.2 Sensitivity of the NTD-Ge Sensor

To achieve the best detector resolution, the detector should be operated at an optimum point where it has the biggest signal to noise ratio. One important part of this process is to understand the sensitivity of the NTD-Ge sensor to the changes in temperature.

When a particle hits the target crystal, the voltage signal change caused by the resistance change of NTD-Ge sensor is:

$$\Delta V = I \cdot \Delta R = I \frac{dR}{dT} \Delta T \,. \tag{5.5}$$

Considering the naïve case, the temperature rise is:

$$\Delta T = \frac{E}{C}, \tag{5.6}$$

where E is the deposited energy and C is the heat capacity of detector.

From the discussion in Section 5.3.1,

$$\frac{dR}{dT} = -\frac{R_0}{2T_0}\left(\frac{T_0}{T}\right)^{\frac{3}{2}} exp\left(\frac{T_0}{T}\right)^{\frac{1}{2}} = -\frac{1}{2T_0}\left(\frac{T_0}{T}\right)^{\frac{3}{2}} R \,. \tag{5.7}$$

Thus,

$$\Delta V = -\frac{R_0 E}{2T_0 C} I \left(\frac{T_0}{T}\right)^{\frac{3}{2}} exp\left(\frac{T_0}{T}\right)^{\frac{1}{2}}, \tag{5.8}$$

and

$$\frac{dR}{dE} = \frac{dR}{dT}\frac{dT}{dE} = -\frac{R_0}{2T_0 C}\left(\frac{T_0}{T}\right)^{\frac{3}{2}} exp\left(\frac{T_0}{T}\right)^{\frac{1}{2}} \tag{5.9}$$

Equation (5.9) shows the sensitivity of the NTD-Ge sensor will increase with lower operating temperature. For a given energy, a higher excitation is also desired to get the signal larger, as shown by Equation (5.8). However, the operating temperature rises with the excitation due to Joule heating. Therefore, the detector module is cooled to the lowest possible temperature during detector testing, and then the excitation is carefully increased to the point where the pulse height is the largest and kept there.

5.3.3 Heat Capacity

Equation (5.8) and (5.9) also show the importance of the detector heat capacity for its sensitivity as it determines how much the temperature will change given a certain energy deposit. Here, contributions to the heat capacity from the NTD-Ge sensor, absorbing crystal, gold film and Araldite are estimated, which gives good indications for optimising the phonon detector design.

Crystal

For non-magnetic, crystalline insulators, the heat capacity is dominated by crystal-lattice vibrations – the phonons. At low temperatures, this contribution can be estimated using the Debye model:

$$C_{ph} = \frac{12}{3}\pi^4 N_0 k_B \left(\frac{T}{\theta_D}\right)^3 = 1944 \left(\frac{T}{\theta_D}\right)^3 J/(mol \cdot K)\,, \qquad \textbf{(5.10)}$$

where N_0 is the number of atoms per mole, k_B is the Boltzmann constant, and θ_D is the Debye temperature. The Debye temperature θ_D is a characteristic of material and a measure of temperature at which the highest-frequency mode, hence every mode, is excited.

For the target crystal, $CaMoO_4$, the Debye temperature was estimated to be 395 K (thermal) or 438 K (elastic), depending on the measurement methods [111]. The latter

was found to be more realistic in a test done by S. J. Lee et al. [112], thus is used for our estimation.

Metal

In addition to lattice vibrations, the free electrons in metal can also be thermally excited and contribute to the heat capacity.

With a spin of 1/2, electrons are fermions and obey the Pauli principle, so each energy state can be occupied by at most two electrons with antiparallel spins. Putting all the electrons into energy states, they will fill them up to a maximum limit known as the Fermi energy:

$$E_F = k_B T_F = \frac{h^2}{8\pi^2 m}\left(\frac{3\pi^2 N}{V}\right)^{\frac{2}{3}}, \tag{5.11}$$

where T_F is the Fermi temperature.

Using the free electron model which assumes the electrons are completely detached from their ions and do not interact with each other, the density of energy states is given by:

$$g_e(E) = \frac{V}{2\pi^2}\left(\frac{8\pi^2 m}{h^2}\right)^{\frac{3}{2}} E^{\frac{1}{2}} \tag{5.12}$$

Also, taking into account the Fermi-Dirac distribution function for the occupancy of energy states, the electronic heat capacity can be calculated as:

$$C_e = \frac{\pi^2}{2} N k_B \frac{T}{T_F} = \gamma T\,. \tag{5.13}$$

γ is known as the Sommerfeld constant.

Adding in the contribution from lattice vibrations, the total heat capacity of a metal at low temperature is

$$C = \gamma T + \beta T^3\,. \tag{5.14}$$

Since the lattice vibration contribution has a T^3 dependence, the heat capacitance of the metal components at the operating temperature will be dominated by the electronic contribution.

For the gold film between the NTD-Ge sensor and $CaMoO_4$ crystal, and the gold pads on top of the sensor, the Sommerfeld constant is γ_{Au} = 0.689 mJ/(mol·K^2) and the Debye temperature θ_D = 162 K [82].

The heat capacity of the NTD-Ge sensor also has both lattice and electronic contributions as described by Equation (5.14) and dominated by the latter at low temperature. The Debye temperature θ_D for germanium is 370 K [113]. Between different NTD-Ge sensors, the Sommerfeld constant may vary due to the effect of neutron doping and metallisation. For the NTD K, used in our experiment, γ_{Ge} = 2×10^{-6} J/(K^2·cm^3) according to the provider of the sensor.

Non-Crystalline Solid

In disordered non-crystalline solids like epoxy, due to the tunnelling transitions or structural relaxations, there is an additional contribution to the heat capacity besides the Debye modes [82]. At low temperatures, along with the T^3 term, there will be an extra linear term in the heat capacity [114, 115]:

$$C_a = AT + BT^3 \tag{5.15}$$

Although the specific Araldite used in our experiment is not tested, 5.55 J/(K^2·m^3) and 23.92 J/(K^4·m^3) are used as the values of A and B respectively for estimation, based on similar samples [115].

To control this part of the contribution, the Araldite is first spread out into a 100 micron thick layer. A metal rod (0.66 mm radius) is then used as a stamp and transfers a small amount of the epoxy onto the gold film. It is assumed that the final Araldite

thickness is about 25 micron by this stamping method. The total adhesive area is twice the rod's cross-section since the stamping process is repeated twice.

The contributions from individual components of the phonon detector are calculated and listed in Table 5.1.

Component	Dimensions (mm^3)	Heat capacity at 20 mK (pJ/K)	Heat capacity at 15 mK (pJ/K)
NTD-Ge sensor	1.5 × 1.5 × 0.5	45.0	33.8
Araldite	$\pi \times 0.66^2 \times 0.025 \times 2$	7.6	5.7
Gold film on crystal	2.2 × 6.2 × 0.00025	4.6	3.5
$CaMoO_4$ crystal	10 × 10 × 5	2.0	0.8
NTD-Ge gold pads	Negligible		
Total heat capacity of phonon detector (pJ/K)		**59.2**	**43.8**

Table 5.1: Heat capacity of the phonon detector with current setup.

As shown in Table 5.1, the contribution from the NTD-Ge sensor dominants the phonon detector heat capacity. This indicates the sensor volume needs to be carefully controlled while the target crystal size can be significantly larger to achieve a greater target mass necessary in a dark matter detection experiment. At 20 mK, the $CaMoO_4$ crystal size can be increased by a factor of 20 before its heat capacity contribution equals the contribution from the NTD-Ge sensor in our setup.

The second largest contribution comes from Araldite. This can be further reduced in the future by using a stamp with smaller cross-section or reduce the initial 100 micron Araldite thickness. The area of the gold film can be limited to roughly 1.6 mm × 1.6 mm in the future, which is still enough for covering the NTD-Ge cross-section. This will reduce its heat capacity by about a factor of 5.

5.3.4 Linearity of Response

As discussed above, when an incident particle deposits its energy in the crystal, the temperature change caused by this is observed as a resistance change of the NTD-

Ge sensor. For small signals, this response can be shown as linear for a stabilised detector, despite the exponential relationship shown in Equation (5.4).

If the detector operating temperature is T, and the change in temperature ΔT causes a change in resistance ΔR, then for $\Delta T \ll T$,

$$\begin{aligned}\Delta R = R(T+\Delta T) - R(T) &= R_0 exp\left(\frac{T_0}{T+\Delta T}\right)^{\frac{1}{2}} - R_0 exp\left(\frac{T_0}{T}\right)^{\frac{1}{2}} \\ &= R_0 exp\left[\frac{T}{T_0}\left(1+\frac{\Delta T}{T}\right)\right]^{-\frac{1}{2}} - R(T) \\ &\approx R_0 exp\left[\left(\frac{T}{T_0}\right)^{-\frac{1}{2}}\left(1-\frac{1}{2}\frac{\Delta T}{T}\right)\right] - R(T) \\ &= R(T)\left[exp\left[\left(\frac{T}{T_0}\right)^{-\frac{1}{2}}\left(-\frac{1}{2}\frac{\Delta T}{T}\right)\right] - 1\right] \\ &\approx R(T)\left[-\frac{1}{2}\frac{\Delta T}{T}\left(\frac{T_0}{T}\right)^{\frac{1}{2}}\right].\end{aligned} \tag{5.16}$$

From the previous discussion, a 1 keV energy deposition will result in a temperature rise of a few micro-Kelvins for the phonon detector operating at around 15 mK, which means the $\Delta T \ll T$ limit is valid. Therefore, this linear approximation is applicable to the phonon detector signals.

5.3.5 Data Acquisition for Phonon Detector

The resistance of the NTD-Ge sensor is read out by passing a modulated bias current through and measuring the voltage across it.

Here, a modulated signal is used because the readout system usually has a DC offset caused by any active electronics components or thermoelectric effect from the cabling system. This offset is also usually time-dependent due to the temperature changes of electronics and level changes of helium. It can be challenging to decouple

this time-dependent offset from the real voltage changes across the NTD-Ge sensor, if using a DC input signal. By using a modulated signal, the effect of this inevitable zero point offset can be eliminated, allowing a direct measurement of an absolute value of the voltage difference.

To provide the modulation signal, a 10 V reference and an inverter are used to provide +10 V and −10 V input to a fast switch. It is controlled by an input from an FPGA to create a 10 V modulated voltage. By sending commands to the FPGA, the frequency of this modulation can be selected in the range from 40 Hz to 1 kHz. This modulation is then used as reference by a set of digital-to-analogue converters (DAC), creating different components of the input modulated bias current. Their amplitudes are again adjusted by inputs from the FPGA to the DACs.

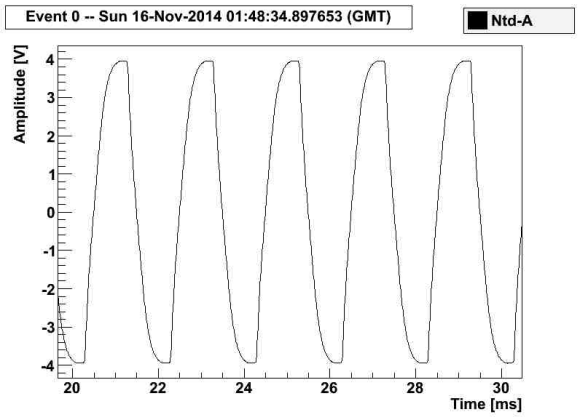


Figure 5.14: NTD-Ge sensor signal and rise time of the modulation.

The modulation is not a perfect square wave but exhibits an obvious rise time. The RC time constant is mainly caused by the mega-ohm resistance of the NTD-Ge sensor and the parasitic capacitance of the readout system, e.g. cabling. This then poses an upper limit to the modulation frequency as shown in Figure 5.14. Therefore, besides the square wave component, an exponential (triangle) component is added. By adjusting the ratio between these two components, this extra triangle contribution

could help by reducing the rise time. However, the extra Joule heating caused by this current is undesirable, so this triangle component is used with caution.

The voltage across the NTD-Ge sensor is then read out through a differential amplifier stage after the laminated semi-flexible cabling system. Each branch of this amplifier is a cascode circuit constructed with a cold FET at ~120 K and a FET at room temperature. To keep the front-end cold stage FET at around 120 K, two PT100 thermometers and two heater resistors are added to the board next to the FET while the board is weakly thermally linked to the 4 K level in K400.

Following this two stage amplifier, there is a summing amplifier stage combing the previous outputs to give the voltage difference across the NTD-Ge sensor. A compensation voltage could be added so when no pulses appear, a null output signal can be produced. Normally the resistance of the NTD-Ge sensor is a few mega-Ohms at its operating temperature, while the change of its resistance is only a few kilo-Ohms. Since the aim is to measure the resistance change instead of the absolute resistance, adding an AC compensation voltage at this stage, which subtracts the nominal operating voltage drop from the output modulation signal, produces a small signal only representing the voltage changes. This small signal can then be easily further amplified without saturating the amplifier or the later readout stages. Additionally, another gain (7 pre-defined values from 1 to 100) can be applied to further improve the resolution.

The amplified signal goes to a 4-pole LTC1563 low-pass Bessel filter with a cut off frequency of 25.6 kHz for anti-aliasing. The filtered signal is then fed to a 16-bit analogue-to-digital converter (ADC) to be digitised and the digitised signal is eventually sent to the computer via the FPGA through optical fibres. The data is stored continuously with a sampling time base that can be as small as 10 μs. The

records are separated into events of up to 32768 data points without any dead time in between.

5.4 Light Channel - Low Temperature PMT

Major research efforts have been carried out in the last decade aiming to improve the performance of PMTs and widening the temperature range of their operation. Low-temperature PMTs have been proven suitable for operation at temperatures of liquid noble gases and recently it has been demonstrated that the low-temperature version of such a PMT can be used for detection of single photons when cooled to 1 K [116, 121]. Further, thanks to effort driven by liquid noble gas dark matter searches and neutrinoless double beta decay experiments in producing ultra-low-background PMTs, they are now also suitable for low-background experiments.

This section will mainly focus on the PMT, its high voltage supply and signal readout system.

5.4.1 PMT Cryogenic Light Detector

There are many advantages of using PMT as the scintillation detector in dark matter experiments. As a standard technology, its excellent sensitivity for single photon detection, low noise and robustness remain compelling reasons for preferring PMTs for the detection of scintillation.

If feasible, using low-temperature PMT as the cryogenic light detector will be far less complex than traditional cryogenic detectors. As mentioned previously, the currently most successful phonon-scintillation detectors for dark matter detection are operated by the CRESST experiment using TES sensors. But the main drawback is that each individual detector requires individual tuning and attention. Also, while some TES-based detectors have exceptionally good performance, the spread in

performance is far too large to build a credible 1-tonne experiment with thousands of detectors. On the other hand, commercially available low-temperature PMTs can be operated using a common high voltage supply distribution, and purchased for a fixed price and guaranteed performance. This makes them a very attractive alternative option for large-scale cryogenic dark matter or double beta decay experiments.

Motivated by these reasons, the feasibility of using low-temperature PMT as part of a phonon-scintillation cryogenic detector operating in the milli-Kelvin temperature range is explored in this study.

The PMT used here is a Hamamatsu R8520-06-PT-UK 10-stage bialkali low radioactivity PMT with platinum underlay for low temperature operation. Its reference specifications are listed in Table 5.2.

PMT	Parameter	Description / Value
	Spectral response	200 mm – 650 mm
	Window material	Synthetic silica
	Photocathode	Bialkali with Pt underlay, 20.5 mm × 20.5 mm
	Dynode	10-stage metal channel dynode
	Maximum supply voltage	900 V (between anode and cathode)
	Average anode current	0.1 mA
	Gain (at 25 °C)	1.0×10^6

Table 5.2: Specifications of the Hamamatsu R8520-06 PMT [117]. Note that the PMT is made to order, therefore some of the listed values are only for reference.

5.4.2 High Voltage Power Supply

As introduced previously, the PMT is positioned in the vicinity of the phonon detector, which is operated at milli-Kelvin temperatures and sensitive enough to pick up micro-Kelvin temperature changes. Therefore, the power supply system that provides the kilovolt high voltage to the PMT should not prevent the phonon detector reaching its operating temperature or introduce noise to the heat channel signal.

In this study, a high voltage system is built based on a Cockcroft-Walton generator (CWG) installed at the Still level (~0.7 K) as shown in Figure 5.3.

CWG Operation Mechanism

The Cockcroft–Walton generator is a circuit design that uses a ladder of capacitors and diodes to generate a high DC voltage from a low AC voltage input. It was named after J. D. Cockcroft and E. T. S. Walton, who performed the first artificial nuclear disintegration in 1932, using this circuit design to power their particle accelerator. Actually the mechanism was first discovered by Heinrich Greinacher in 1919, so it is sometimes also referred to as the Greinacher multiplier. A schematic of a simple three stage CWG is shown in Figure 5.15.

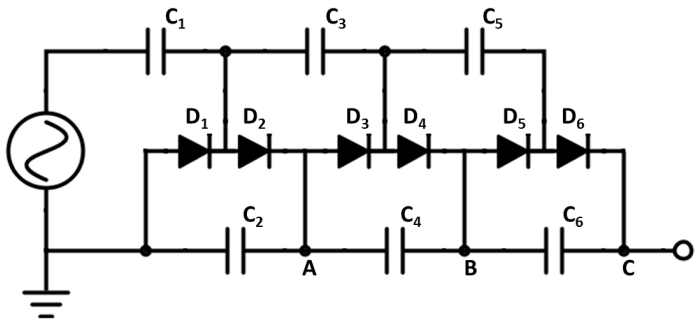


Figure 5.15: Schematic of a three stage Cockcroft-Walton generator with AC input.

Taking this simple example, assuming ideal components with no loses, the multiplier works as follows:

1. When AC input reaches its negative peak, D_1 allows current to flow from the ground into C_1, filling it up to V_p;
2. When the AC input reverses polarity, the positive end from the AC input adds to the C_1 potential. Thus, current flows through D_2, charging C_2 to $2V_p$;
3. Then the AC input reverses polarity again. C_3 is charged to $2V_p$ through D_3 as the AC input adds to the potential of C_1 and C_2;
4. Next C_4 is charged to $2V_p$ through D_4 similar to the process in step 2.

5. Similarly, C_5 and C_6 will be charged to $2V_p$ later when the AC input changes polarity.

Therefore, the output voltage between ground and point A, V_{GA}, is $2V_p$; V_{GB} and V_{GC} are $4V_p$ and $6V_p$ respectively. More stages can be added to the ladder and this process will continue, charging all the capacitors. The highest output voltage will then be twice the peak input voltage multiplied by the number of stages in the multiplier.

If a load is attached, the voltage drop and the ripple voltage can be calculated as [118, 119]:

$$V_{drop} = \frac{I_{load}}{6fC} \cdot (4n^3 + 3n^2 - n)\,, \tag{5.17}$$

and

$$V_{ripple} = \frac{I_{load}}{2fC} \cdot n \cdot (n+1)\,, \tag{5.18}$$

where I_{load} is the load current, C is the stage capacitance, f is the AC frequency and n is the number of stages.

CWG Design

The suggested voltage distribution ratio of the PMT power supply is shown in Figure 5.16. Based on this, the CWG used in this study is designed to be 25-stage.

Voltage Distribution Ratio and Supply Voltage

K	G	Dy1	Dy2	Dy3	Dy4	Dy5	Dy6	Dy7	Dy8	Dy9	Dy10	P
0.5	1.5	2	1	1	1	1	1	1	1	1	0.5	

Supply Voltage : 800 V K : Cathode G : Grid Dy : Dynode P : Anode

Figure 5.16: Suggested distribution ratio of the PMT supply voltage from Hamamatsu [117].

The schematic is shown in Figure 5.17. The CWG is driven by a small AC voltage source kept at room temperature and a transformer located at 4 K. Different dynodes of the PMT are tapped at various stages according to the voltage distribution shown in

Figure 5.16. R_3 and C_2 are installed to ensure that the DC high voltage goes to the anode while the PMT high frequency signal goes to the readout system.

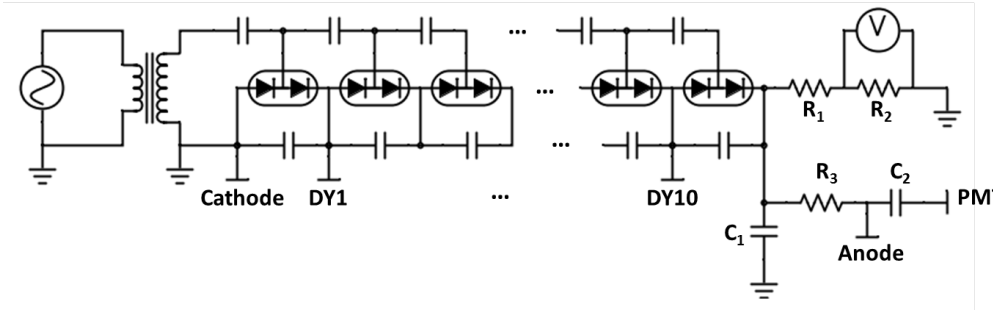


Figure 5.17: Schematic of the high voltage power supply based on a 25-stage CWG design and its connections to the PMT. Only the first and the last few stages of the CWG are shown for simplicity. An attenuator consisting of two resistors, R_1 and R_2, for high voltage monitoring is also shown here (top right corner).

The generated high voltage is measured after attenuation, which is done by the combination of R_1 and R_2.

Component Selection

One advantage of the CWG is that the capacitors and the diodes only need to withstand $2V_p$ instead of the full high voltage. This makes it possible to build the CWG as a relatively compact surface mount PCB instead of using bulky high voltage rated components. It should be noted that a few components still need to be high voltage rated, such as R_1, C_1 and C_2. In practice, the components with a minimum voltage rating of twice the actual applied voltage are chosen if possible.

Besides voltage rating, since the CWG is operated at a temperature below 1 K, the components should also be suitable for the low-temperature environment. Generally speaking, NPO (negative-positive-zero) ceramic capacitors are preferable for low-temperature application [120]. For resistors, metal film, thin film and thick film resistors could behave well at low temperatures, but ultimately it depends on the specific type used. For diodes, low leakage current is desired to maintain the voltages;

and forward voltage should not increase too much at low temperature to prevent significant heat dissipation.

Several candidates were tested at 4.2 K (liquid helium) and the final components were chosen based on these results. In general, NPO ceramic capacitors hold their values very well down to 4.2 K. However, most resistors' values rise to 1.5 – 2 times of the nominal value at 4.2 K, despite their types. Thus an extra set of resistors from the same batches are installed in K400 as reference. Their resistances can be monitored during the cool-down. For the chosen diode, its forward voltage drop under a 1 mA load increases to 2.7 V when cooled down to 4.2 K. More detailed test results and specifications can be found in the Appendix.

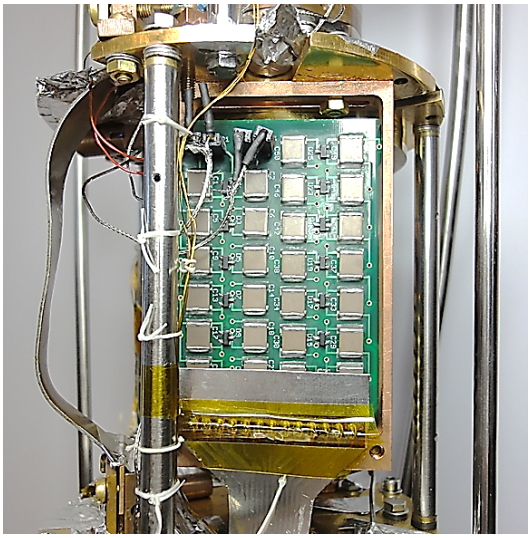


Figure 5.18: Final CWG board (PCB dimensions: 72 mm × 48 mm) installed inside the K400 cryostat.

The finished CWG board in the K400 cryostat is shown in Figure 5.18. The specifications of major components chosen for the CWG/PMT circuit are listed in Table 5.3.

CWG series capacitor	470 nF, NPO ceramic
Diode	MMBD1503A low leakage
Attenuator	1GΩ : 1MΩ, thick film
Signal isolating capacitor	1.2 nF, NPO ceramic
Signal isolating resistor	0.67 MΩ, metal film
Transformer[7] winding ratio [121]	25 : 600

Table 5.3: Specifications (nominal) of selected components used in the 25-stage CWG / PMT circuit.

CWG Position in K400

One of the primary considerations when deciding where to install the CWG in the K400 cryostat is heat dissipation. It needs to be positioned at an appropriate temperature level so it does not prevent the detector from cooling. The heat dissipation of the CWG mainly comes from the diodes, and the attenuator resistors. When the CWG is at a steady operating state, the diode current is the same as the load current. For a conservative estimation, it is assumed that the diode forward voltage drop rises to 5 V and the attenuator resistance becomes 2 GΩ at low temperature. Then for supplying 2 kV high voltage, the power dissipation of a 25-stage CWG is:

$$P_{diss} = 5V \times \frac{2\ kV}{2\ G\Omega} \times 50 + \frac{(2\ kV)^2}{2\ G\Omega} = 2.25\ mW\ . \quad \textbf{(5.19)}$$

As shown in Section 3.4, when the mixing chamber is at 16.0 mK, the K400 can provide 5.0 μW cooling power at the mixing chamber level and 20.0 mW cooling power at the still level. Obviously, the multiplier dissipates too much heat to be installed in the vicinity of PMT. Therefore, the CWG is thermalised to the still level, where the cooling power is comfortably above its heat dissipation.

[7] The transformer was tested and used in a separate experiment previously. It uses molypermalloy powder (MPP) cores, which exhibited stable permittivity under cooling to 4.2 K [121].

5.4.3 Light Detector Readout System

The PMT pulse signal is readout by a 14-bit ADC board. Before digitizing, the signal is amplified 10 times by a differential amplifier. The signal then goes to an FPGA and sent to a computer through optical fibres to be stored. The record length can be as long as 131072, and the time base could vary between 5 ns and 40 ns.

Usually in room temperature measurements, a level trigger is set. If the average of 8 consecutive points is above this value, then the following set amount of data points are continuously recorded, including both single photons and empty baseline. However, the decay time constant of the scintillator used in this detector module is relatively long as introduced in Section 5.2. It is already above 350 μs at 6.7 K and expected to be larger during cooling. Limited by the available memory resource in the FPGA, the full scintillation events will eventually be longer than the longest continuous recording length and thus only partial events can be recorded as shown in Figure 5.19.

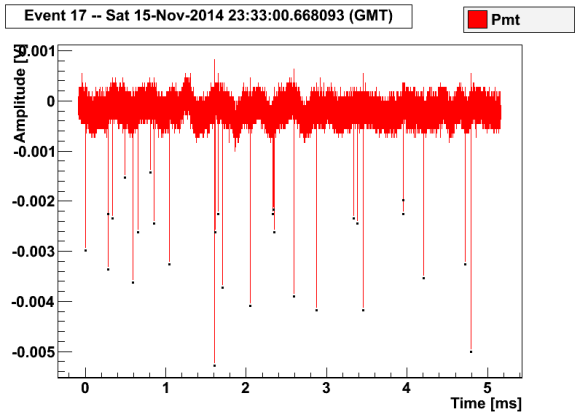


Figure 5.19: A scintillation event recorded in the continuous mode. The record length is 131072 with a 40 ns time base. Since the full event is much longer than 5 ms, only a partial event can be recorded.

To solve this problem, another recording method is developed so that only single photons are recorded while the empty baseline is not. The signal is recorded as a series of single photon records as shown in Figure 5.20.

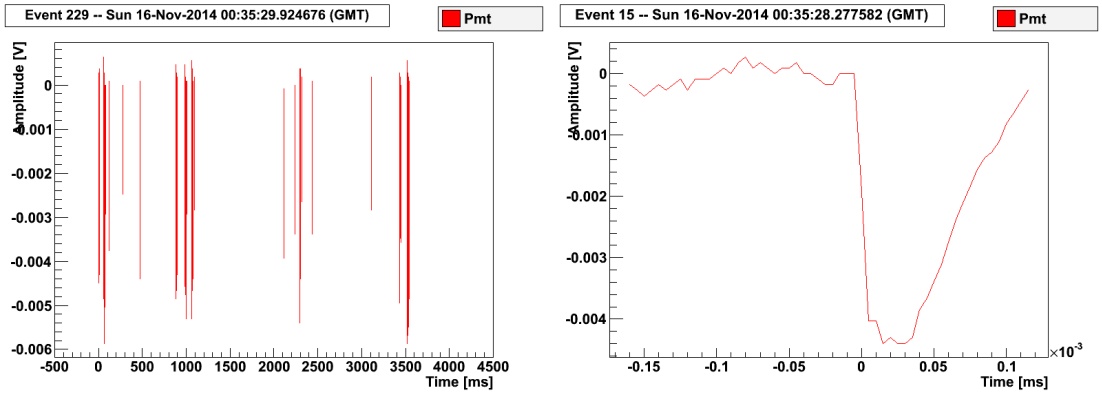


Figure 5.20: Scintillation events recorded in single photon mode: (left) photons recorded within 5000 ms; (right) zoom in of one single photon record.

When the decay constant increases, it is the time interval between two photons that increases. Therefore, by this way, the increasing decay constant does not necessarily require longer record length. Assuming each single photon record is roughly 280 ns long, and the time base is chosen to be 5 ns, then a scintillation event with 60 photons only requires 3420 data sample points. Comparing to the previous continuous recording method, in which 131072 samples with 40 ns time base still cannot account for one full event, the single photon recording method has a huge advantage in saving storage space, and therefore continuous recording capability.

Besides the main readout system for the PMT signal, another ADC board is used for monitoring the DC high voltage output of the CWG. The attenuated high voltage signal is first picked up by a high impedance buffer, which is followed by a differential amplification stage. The amplified signal is then fed through a 4-pole Bessel filter for anti-aliasing and digitised by the ADC. It is then sent to a computer via an FPGA and recorded continuously.

6 Phonon-Scintillation Detector Tests and Data Analysis

The infrastructure and the phonon-scintillation detector setup as well as the properties of major components were discussed in the previous chapter. The feasibility and performance of this phonon-scintillation prototype detector is tested in the K400 cryostat at Oxford. The results obtained in these tests are discussed here.

In this study, several novel aspects have been explored, tested and verified: the possibility of operating a PMT at milli-Kelvin temperatures, the effects on the phonon detector from the operation of a PMT and its high voltage power supply, and the overall performance of this phonon-scintillation detector module. In addition, the scintillation decay time of the absorber crystal used, $CaMoO_4$, below 7 K down to milli-Kelvin temperatures was studied to complement the previously published data measured at higher temperatures.

This chapter starts with a discussion of the light detector operation and its response when the cryostat is cooled down to a steady running state. Then the gamma source for detector module testing and calibration, cobalt-57, is introduced. Following this, the data analysis process and the obtained spectrum are discussed. Finally the scintillation decay time of $CaMoO_4$ at cryogenic temperatures observed in this study are presented.

6.1 Light Detector Operation and PMT response

This section mainly focuses on the operation of the PMT high voltage supply, the effects of turning on this power supply and the response of the PMT at low temperatures.

6.1.1 HV Supply Frequency Response

The high voltage supply system can be seen as a RLC circuit consisting of the transformer inductance, the CWG and cabling capacitance, the wiring resistance, etc. To minimise heat generation, a frequency for the input AC power should be used that is close to or at the resonance frequency of this system so that the overall efficiency of the transformer and the CWG is optimised.

Since the inductance, capacitance and resistance could all be affected by temperature, the frequency response of this high voltage supply system varies with its operating temperature. Figure 6.1 shows the observed frequency response at room temperature before cooling and at low temperature when the K400 is in a steady-operation state.

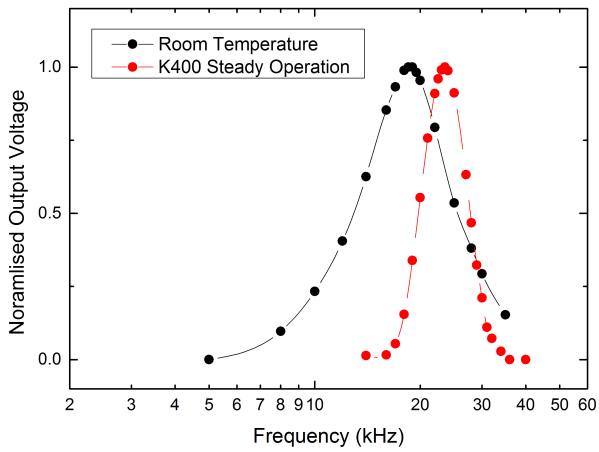


Figure 6.1: Frequency response of the high voltage power supply.

Based on this, the AC input frequency is chosen to be 23 kHz during detector operation.

Figure 6.1 also shows that, at low temperature, the resonant frequency increases, and the peak is also narrower compared to the frequency response curve at room temperature. If approximating this complex circuit as a series RLC circuit made of the transformer inductance, wiring resistance, cable capacitance and a mainly capacitive load of CWG, then the resonant frequency is given as $\omega_r = \omega_0\sqrt{1-2\zeta^2} = \sqrt{1/LC - R^2/2L^2}$ (where ζ is the damping factor), and its quality factor Q is given as $Q = \omega_0 L/R = \sqrt{L/CR^2}$. While the transformer inductance and the CWG capacitance should remain roughly constant (Section 5.4.2), the cable capacitance and the resistance of various metal wiring are expected to drop during cooling. Therefore, a larger resonant frequency and a larger quality factor (narrow peak) would be expected at lower temperatures. This is consistent with the curves shown in Figure 6.1.

6.1.2 Effects on Phonon Channel Signal from PMT HV Supply

When the experimental plates reach base temperature, the AC input signal from a function generator, positioned at the cryostat top, at room temperature is applied. It is gradually increased from zero to the appropriate value that gives a proper pulse height from the PMT. This extra high voltage power supply could cause a temperature rise at the various places it is heat anchored to or introduce electromagnetic interferences compromising the signal of the phonon detector. The observed changes caused by it are discussed in this section.

Thermal Effect

When a 2.2 V peak-to-peak input voltage from the function generator is applied, the value changes of selected monitors relevant to the still operation are listed in Table 6.1.

	Without High Voltage	With High Voltage
2200 Ω RuO_2 Still Thermometer	4.823 kΩ	4.582 kΩ
1K Pot Temperature	1.384 K	1.389 K
Condenser Line Pressure	67.9 mbar	69.5 mbar
Pressure behind He-3 Pump	103.4 mbar	108.0 mbar

Table 6.1: Values of selected K400 monitors before and after turning on the high voltage supply.

These changes are all indicative of a small temperature rise due to the operation of this high voltage supply system. However, they are within the range of expected variation during normal cryostat operation. When running the K400, the adjustment of the 1K pot filling rate can cause larger changes. Additionally, for keeping the mixture circulation rate high enough to provide sufficient cooling power, a heating power of a few milli-watts is normally applied to the still, also causing the listed values to change.

This is consistent with the estimation of CWG heat dissipation in Section 5.4.2, which is at the level of a few milli-watts. Beneficially, the heat production of the CWG can be used as part of the still heating power, and the still heater power can be reduced accordingly.

As for the mixing chamber level, when the high voltage is supplied to power the PMT, there is no noticeable change in the NTD-Ge sensor resistance, meaning a relatively stable detector module temperature despite the high voltage.

It shows that, with proper arrangement and heatsinking, the heat dissipation from the high voltage supply does not affect the performance of the cryogenic phonon detector.

Electrical Effect

With the CWG positioned at the still level, 13 high voltage wires running between the still level and the experimental plate are required to deliver the various required voltages (see Figure 5.16 and Figure 5.17) to PMT dynodes and anodes. Their shielding is in contact with the grounded cryostat structure for heatsinking. To prevent potential sparking between high voltage wires and electrical ground, as well as reducing electromagnetic interference, the insulation should be carefully arranged. Additionally, heat transfer through the wiring also needs to be controlled. Based on these considerations, the stainless steel semi-flexible laminated cable as described in previous chapters is actually a suitable solution and it is chosen to link the CWG and the PMT in this setup.

The CWG and sections of the high voltage supply cabling are located in the close proximity of the NTD-Ge sensor signal readout line as shown in Figure 6.2.

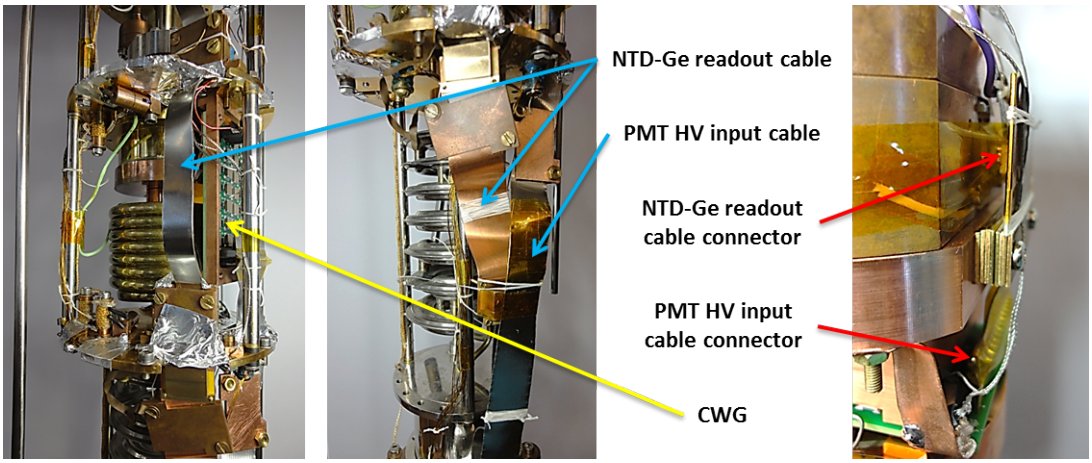


Figure 6.2: Arrangement of the CWG, PMT high voltage supply cable, NTD-Ge readout cable and their connectors in the K400 setup (partial).

This means the electromagnetic interference introduced by the AC signal driving the CWG or the ripple voltage as described by Equation (5.18) could be picked up by the phonon channel readout system and compromise the signal. To minimise this effect, all the cables are shielded wherever possible. Additionally, an extra brass

shielding plate is placed between the NTD-Ge sensor readout cable connector and the PMT HV input cable, which can be seen in Figure 6.2 (right).

Comparing the frequency spectra for the phonon channel baseline before and after applying the AC input voltage to the CWG, it shows an extra single peak at 23 kHz when the high voltage is on (Figure 6.3). This is exactly the frequency of the AC input voltage. Because it is way beyond the frequency region of the phonon channel signal, which is below 1 kHz, this extra noise contribution can be filtered out in the analysis. Besides this peak, the AC signal has no obvious influence on the phonon channel in the current setup as shown in Figure 6.3.

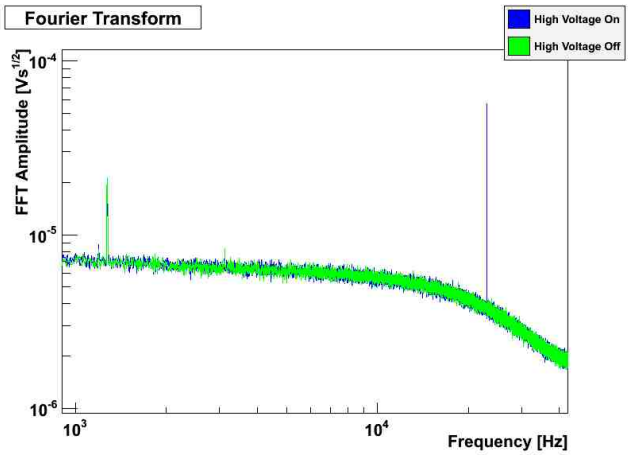


Figure 6.3: Section of noise spectra for the phonon channel baseline with or without the high voltage / AC input voltage. The only difference, a peak at 23 kHz, can be seen when the high voltage is on.

Therefore, with proper shielding and high resonant frequency, the high voltage supply system can be installed very close to the phonon channel readout system. This is particularly important for building large dark matter experiments, which usually have limited space budget for cold electronics and cabling.

6.1.3 PMT Response at Low Temperature

Since the high voltage supply system does not prevent the detector module from cooling as shown above, the PMT was successfully cooled down to base temperature

of the K400 cryostat to test the possibility of operating it at milli-Kelvin temperatures. The PMT response at various low temperatures is presented below.

Figure 6.4 shows examples of scintillation events recorded when testing the PMT at different temperatures. Clearly, this proves that the low-temperature, low-radioactivity PMT used here can be successfully operated at milli-Kelvin temperature range where the NTD-Ge sensor has enough resistance to be applicable simultaneously.

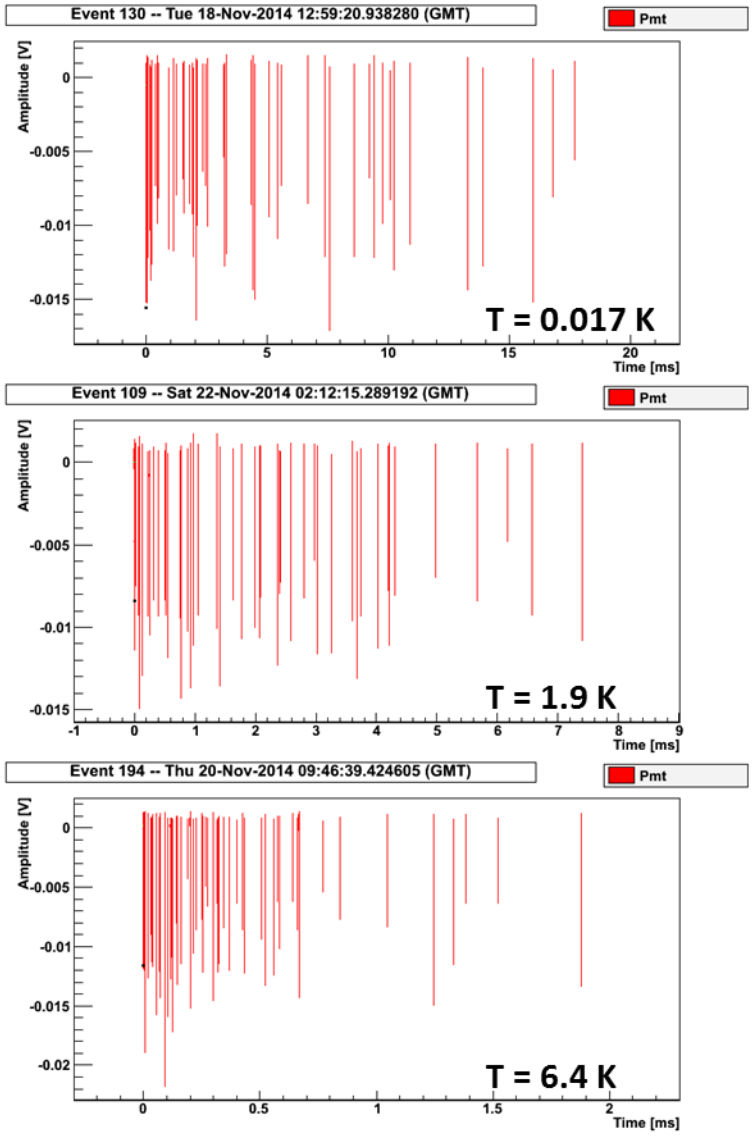


Figure 6.4: Scintillation event records of the light channel when operated at various low temperatures using a cobalt-57 gamma source.

The recorded scintillation events at different temperatures are similar except for their decay time. This is consistent with our previous discussion about the scintillating property of the target crystal, $CaMoO_4$. More details will be discussed in Section 6.5.

Besides scintillation events caused by gammas from the test source, there are also background events. For example, Figure 6.5 shows a scintillation event caused by a cosmic muon interaction in the detector target crystal.

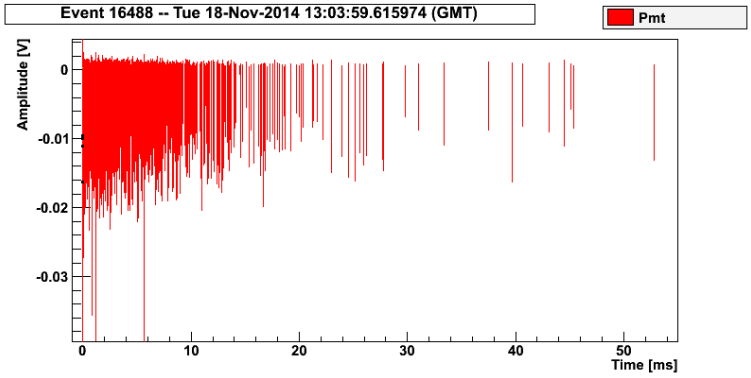


Figure 6.5: Example of a scintillation event caused by a muon when the PMT is at 17 mK.

While testing the PMT at various temperatures below 10 K, it is also noticed that to get similar single photon signal heights, the high voltage applied to the PMT dynodes and anode need to be higher at lower temperature. Figure 6.6 shows the applied high voltages for PMT tests at different temperatures. Admittedly, the "similar photon signal height" is determined by eye, and thus very subjective. Also, as mentioned in Section 5.4.2, the resistance of the attenuator resistors changes under cooling, which means the dividing ratio may also change. Thus a reference attenuator using resistors from the same batches was installed next to the CWG board. Wires attached to the terminals of the reference attenuator were routed outside the cryostat and hence the dividing ratio could be measured while the resistors were cold. The high voltages are deduced using the dividing ratio values of this reference divider, which can introduce further error. However, the broad tendency can be seen here.

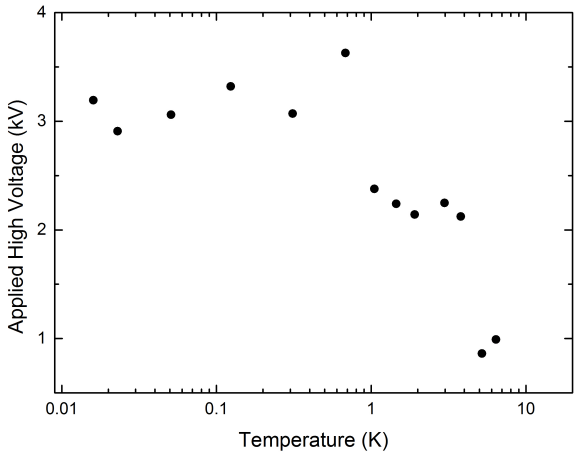


Figure 6.6: High voltages supplied to PMT anode while testing the PMT at various temperatures.

This suggests that the efficiency for secondary electron emission of the metal dynodes used in this Hamamatsu R8520-06-PT-UK 10-stage PMT decreases during cooling. As a result, to operate the detector module in the milli-Kelvin temperature range, the actual applied high voltage is much higher than the maximum rating suggested by data sheet.

As the possibility of operating a commercially available PMT at milli-Kelvin temperatures has been demonstrated, the performance of the whole phonon-scintillation detector module in test runs using a cobalt-57 gamma source will be discussed in the following sections.

6.2 Test Source – Cobalt-57

For detector tests and calibrations, a Cobalt-57 source is placed outside the K400 cryostat. ^{57}Co decays by 100% electron capture to the excited levels of ^{57}Fe. It then continues to decay to the ground state of ^{57}Fe by internal transitions, predominately producing either gamma particles with 122 keV and 14 keV in cascade, or gamma particles with 136 keV, when decaying directly to the ground state [122, 123]. A detailed decay scheme of ^{57}Co is shown in Figure 6.7.

Figure removed due to copyright reasons.

Figure 6.7: Decay scheme of Cobalt-57 [123].

Based on the decay scheme, 3 large peaks corresponding to 14.41 keV, 122.06 keV and 136.47 keV would be expected in the obtained spectrum. But as the source is positioned outside the K400, the 14.4 keV peak will be greatly reduced due to the cryostat's layered metal structures. Therefore, the most prominent features of the spectrum are expected to be the 122.06 keV peak, with a smaller 136.47 keV peak alongside. Without considering the scattering within materials, their abundances should be approximately 8.5: 1.

Besides the full energy peaks, additional features can be produced due to Compton scattering. The energies of the scattered gamma ray and recoiled electron are given by

$$E_r{}' = \frac{E_r}{1 + (E_r/m_0c^2)(1 - \cos\theta)} \tag{6.1}$$

and

$$E_e = \frac{E_r}{1 + m_0c^2/E_r(1 - \cos\theta)}, \quad \textbf{(6.2)}$$

respectively, where m_0c^2 is the rest mass energy of the electron (0.511MeV).

If the interaction happens in the absorber crystal, and the scattered photon escapes the detector, then the deposited energy can be calculated using Equation (6.2). Since this energy depends on the scattering angle, the feature will have a continuous distribution, which is known as the Compton edge. But this edge could be softened if the photon scattered multiple times, resulting in a distribution between the Compton edge and the full energy peak.

Compton scattering may also happen within surrounding materials before the gamma particle reaches the detector. Then the remaining energy of the scattered gamma can be calculated using Equation (6.1). These backscattered gammas may then produce an inverse Compton continuum, which results in a broadened shoulder on the low energy side of the peak and a backscatter edge. This feature can again be softened by multiple scattering.

In addition, a set of X-ray escape peaks can be produced and appear in the spectrum. When the incoming photon energy is sufficient, which is the case here, with γ-energies for photons directly from the ^{57}Co source larger than 100 keV, it can break the binding of an electron of the inner shells. This leaves a vacancy in that shell, which is then filled by an electron from an outer shell, thus emitting an X-ray. The energy of these X-rays is defined by the energy differences between the electrons' initial and final shell positons.

If these X-rays are re-absorbed by the crystal, then the deposited energy will stay the same, the event will be seen as part of the full energy peak. But if these X-rays escape, then an escape peak will appear in the spectrum at the energy equals to the full energy minus the escaped X-ray energy.

For the $CaMoO_4$ crystal used in our detector, the processes where an electron from the L or M shell of molybdenum fills a vacancy in its K shell will result in X-rays with energy around 20 keV, while all the other processes only give X-rays with a few keV or less energy [124, 125]. Some characteristic X-ray energies of calcium and molybdenum are listed in Table 6.2.

	$K_{\alpha 1}$ (keV)	$K_{\alpha 2}$ (keV)	$K_{\beta 1}$ (keV)	$K_{\beta 2}$ (keV)
Calcium	3.692	3.688	4.013	-
Molybdenum	17.479	17.374	19.608	19.960

Table 6.2: Selected characteristic K-series X-ray line energies of calcium and molybdenum. Data taken from [125].

The escape peak can also be broadened by Compton scattering of the escaping photon, leaving some of its energy in the detector, while the rest still escapes. The shape of this distribution resembles an inverse Compton scattering spectrum, with the Compton edge on the lower energy side of the distribution.

In a real detector scenario, more small extra features from secondary radiations could also appear. The response to be expected for a real detector will depend on the size, shape, material of the absorber crystal, the over-all setup and the source position. The effects of these various processes can be determined by Monte Carlo simulation. Such a simulation is carried out and presented in Section 6.4 along with data.

6.3 Data Processing

The data from the phonon and the scintillation light detector are recorded separately as described in Chapter 5. When processing these data, they are first analysed separately, and then the correlation of pulses from these two detectors is investigated. The general procedure of this data analysis process is introduced in this section.

6.3.1 Phonon Detector Data Analysis

The recorded raw data from the phonon detector is a continuous modulated signal as described in Section 5.3.5. The first step of processing these data is removing this modulation. As shown in Figure 6.8, after finding the baseline (central value) and the switching points, an area depending on the NTD-Ge resistance can be defined for each period, marked as the light grey area. Due to the RC rise time, this area is calculated by summing up small slices between two consecutive data points like the dark grey area between points *i* and *i+1*, as shown in Figure 6.8. Each slice's area is calculated using the trapezium rule. This sum is them divided by the time of the period to give the average amplitude for this period.

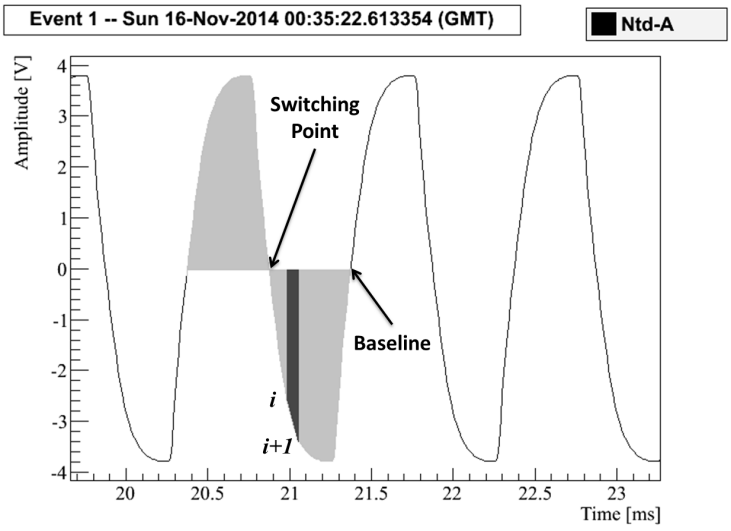


Figure 6.8: One example of recorded modulation. The light grey area between data points and baseline for one period is calculated by summing up slices like the dark grey trapezium between two consecutive data points.

After demodulation, the new sampling rate of the processed signal will be the same as the modulation frequency. A higher sampling rate of the DAQ will yield a more accurate area value for each period. Therefore, to get a better resolution, the sampling rate and modulation frequency should be set as high as possible when recording data from NTD-Ge sensor.

After getting the new array of data, an offline trigger is used for finding the pulses. This is done by setting two threshold values above the baseline: one for the beginning of a pulse where the signal rises above the first threshold value and the other for the end where the signal falls back below the second threshold value. If the signal does not fall below the second threshold, then the pulse is ended after a fixed amount of time.

These two threshold values are determined based on 70 ms of baseline data that end 15 ms before the point of interest. The average position of the baseline and the RMS of the baseline noise are calculated. Then the two thresholds are set to be 9 and 5 times the baseline RMS above the baseline value respectively. The pulse is ended after 300 ms if it does not fall below the second threshold.

Having recognised all the pulses in the record, the next step is to calculate some initial pulse parameters and apply various cuts to remove pile-up, distorted or spurious pulses before fitting with a pulse template. The cuts are mainly focused on baseline fluctuation, baseline RMS, pile-up pulses and pulse shape, as follows:

1. Baseline gradient of the pre-trigger region;
2. Pile-up parameter;
3. Pulse rise time;
4. Baseline difference between right and left side of pulse;
5. Baseline RMS of the pre-trigger region;
6. Pulse area over pulse height;
7. Pulse decay time.

These parameters are fitted with Gaussian distributions. The cutting bounds and their effects (taking a typical data set as example) are listed in Table 6.3.

Cut Parameter	Lower Bound	Upper Bound	Remaining
Baseline gradient	- σ	σ	45.0%
Pile-up parameter	0	μ + 3σ	69.9%
Pulse rise time	μ - 2σ	μ + 2σ	92.2%
Right minus left of baseline	μ - 2σ	μ + 2σ	80.7%
Baseline RMS	0	μ + 2σ	93.3%
Pulse area over pulse height	μ + 3σ	μ + 3σ	98.2%
Pulse decay time	μ + 3σ	μ + 3σ	99.4%
Combined			21.3%

Table 6.3: Applied cuts based on initial pulse parameters and their effects on the amount of event entries for a typical data set.

By applying the cuts, a clean list of events can be obtained for further analysis. The energy of each remaining pulse is first roughly estimated using the difference between the maximum point and the baseline. An initial pulse height spectrum is then produced based on this rough estimation, as shown in Figure 6.9.

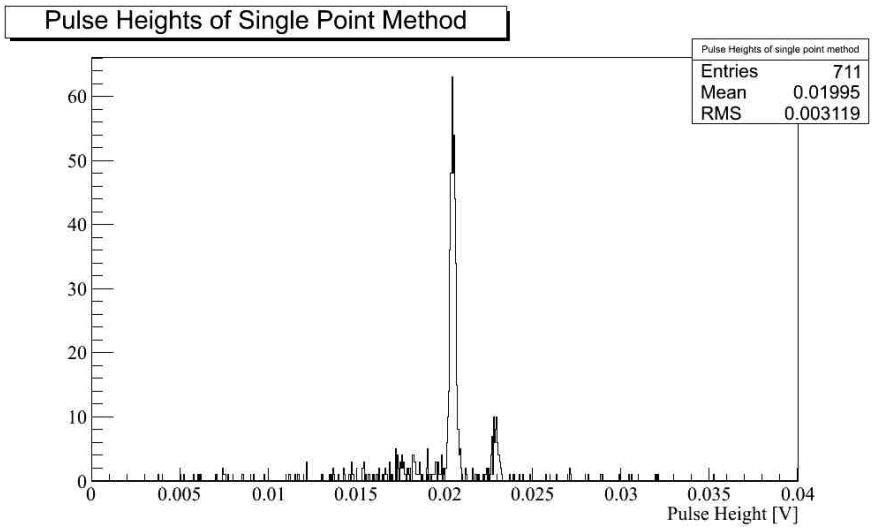


Figure 6.9: Pulse height spectrum using difference between the maximum point and baseline values for each pulse.

This spectrum is useful as a template pulse for a particular energy can be extracted from it, which then can be used to find the rough values of the time constants for the exponential pulse shape. These values are the initial parameters for the proper pulse fit later. This template pulse is obtained by averaging pulses within the maximum bin. It is fitted with the theoretical form of the pulse shape:

$$For\ t \geq t_0,$$

$$f(t) = (l + g\times t) + s\times\left(-A_1 e^{-t/\tau_1} + A_2 e^{-t/\tau_2} + A_3 e^{-t/\tau_3}\right); \quad \textbf{(6.3)}$$

$$For\ t < t_0,$$

$$f(t) = l + g\times t\,.$$

Here l and g characterise the baseline; s is a scaling factor based on the energy of the pulse; t_0 is the starting point of the pulse.

A_1, A_2, A_3, τ_1, τ_2 and τ_3 are used to characterise the pulse shape. The first exponential term is associated with the rise of the pulse while the other two terms are associated with the decay. The fast decay time depends on the decoupling of the electron and phonon system as well as the heat transfer processes within the phonon detector. The slow decay time then describes the heat transfer from the detector to the heat bath (detector holder) through the gold bond wires.

For one typical data set, the fit result is shown in Figure 6.10.

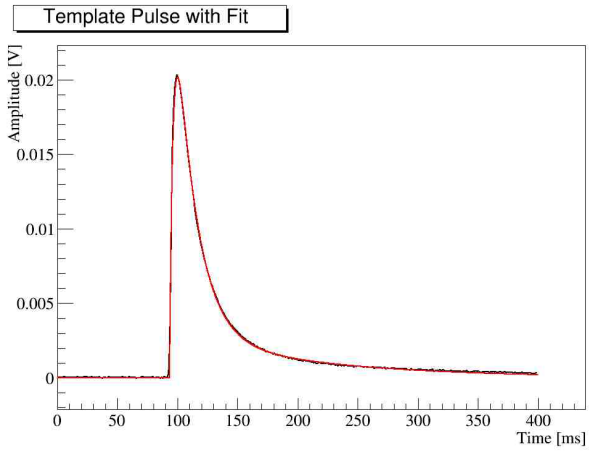


Figure 6.10: An average pulse from a typical data set. The black line is the average pulse and the red solid line is the best fit using Equation (6.3).

With the initial parameter values from the fitting of this average pulse, the complete list of pulses is fitted. Using the pulse heights found by this exponential fit, Figure 6.9 is improved to Figure 6.11.

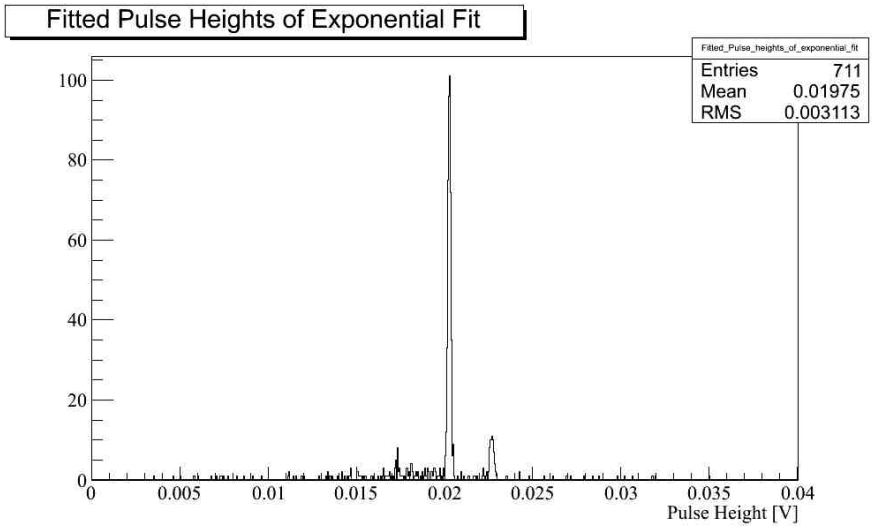


Figure 6.11: Pulse height spectrum using values given by the exponential fit for each pulse.

Based on fitting quality, which is measured by chi-square, a final cut can be carried out, which gives Figure 6.12.

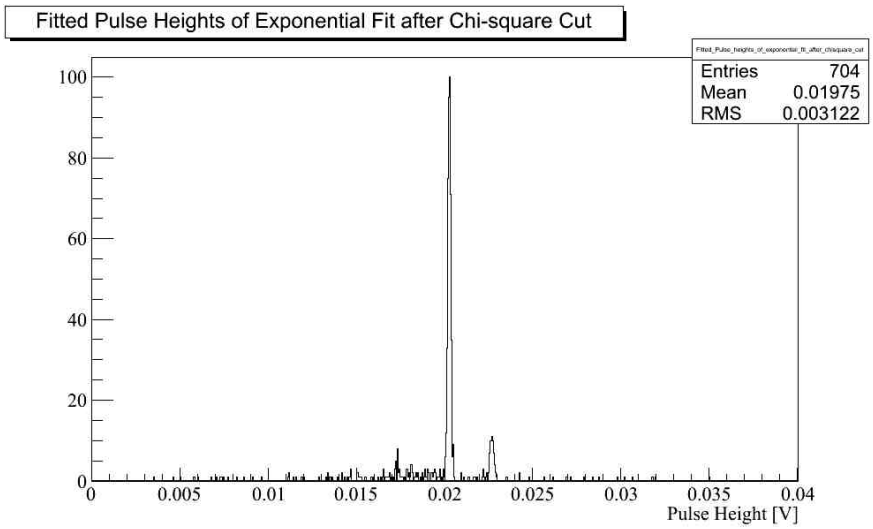


Figure 6.12: Pulse height spectrum after a cut on the chi-square of the exponential fit.

So far, the signals are represented by the changes of voltage. The final step is then converting the voltage signals into their corresponding energies. This conversion contains three factors as shown below:

$$\Delta V = \frac{dV}{dR}\frac{dR}{dT}\frac{dT}{dE}\Delta E \ . \qquad \textbf{(6.4)}$$

Since $\Delta E = C(T)\Delta T$, for a stabilised detector, the conversion between energy deposition and temperature change is linear. Additionally, as discussed in Section 5.3.4, for the small ΔT here, the resistance change of NTD-Ge sensor also has a linear relation with the change of temperature. The term dV/dR depends on the readout system and the demodulation method. The relation between the pulse height value and the NTD-Ge sensor resistance is affected by the modulation frequency and the effect of the parasitic capacitance. However, for the small changes caused by a particle interaction in the cryogenic detector, the conversion between amplitude and resistance will be approximately linear.

Therefore, for smaller signals from the phonon detector, the amplitude voltages can be converted into energies by simply multiplying a scaling constant, which can be determined from calibration with pulses of a known energy, like the 122.06 keV and 136.47 keV gammas from the cobalt-57 source used in this study. The energy spectra calibrated in keV are shown and discussed in Section 6.4.

6.3.2 Light Detector Data Analysis

Since the signal of PMT is recorded as single photon peaks arriving at the PMT's anode (photon counting mode), the energy of a scintillation event is determined by counting its photon number.

The main step of analysing the data recorded as single photons (Figure 5.20) is separating them into groups of scintillation events. This is done by comparing the time stamp of each triggered single photon record. If the time difference between photon *i* and *i+1* is larger than a value, which is optimised considering event rate and dark count rate, then photon *i* is considered to be the last photon of this scintillation event and photon *i+1* is the first photon of the next event. Then the number of single photon records within each group is the photon number of that scintillation event. An

initial spectrum can be plotted using these values, as shown in Figure 6.13. In parallel, the time stamp of the first photon record within each group is recorded as the time stamp of that scintillation event.

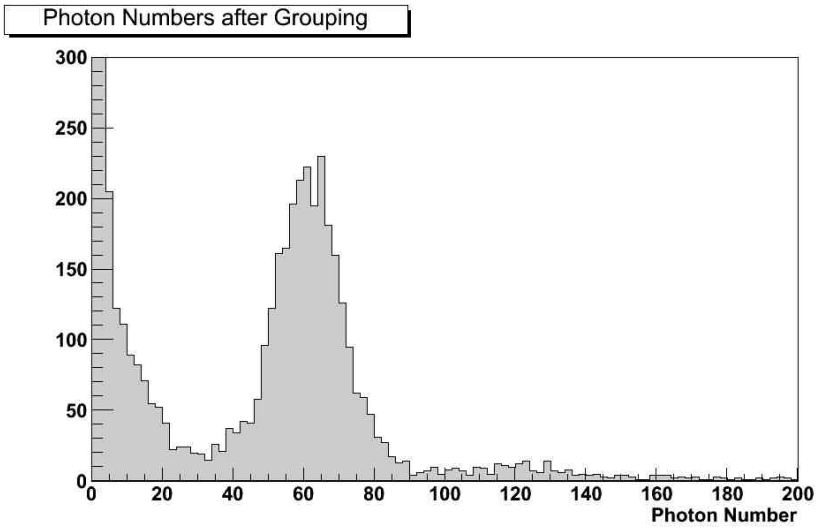


Figure 6.13: Photon number spectrum using values obtained from grouping single photon records.

6.3.3 Pulse Correlation

From previous analysis, the following information is obtained and recorded:

- The pulse heights and the pulse time stamps of the NTD signal;
- The photon numbers and the scintillation event time stamps of the PMT signal.

By comparing the time stamps, correlated pulses from the heat and light channels can be found. Figure 6.14 shows such comparison of a typical data set.

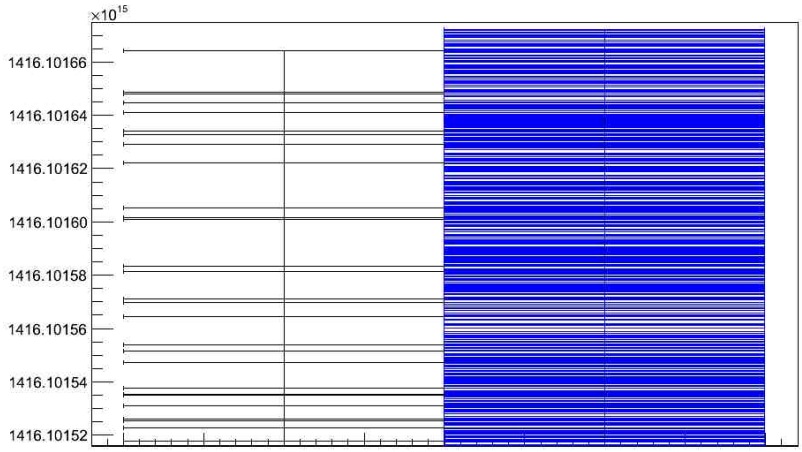


Figure 6.14: Time Stamp Comparison. The time stamps are plotted as horizontal bars here. The black lines on the left side are time stamps of the NTD pulses and the blue lines on the right side are those of the PMT events.

The remaining NTD pulses have gone through several cuts so the total number is much smaller than the PMT events. Therefore the correlation is done by iterating through the NTD pulses. If there is a PMT event within 2 ms before or after a certain NTD pulse, and it is not a dark count single peak event, then they are considered correlated.

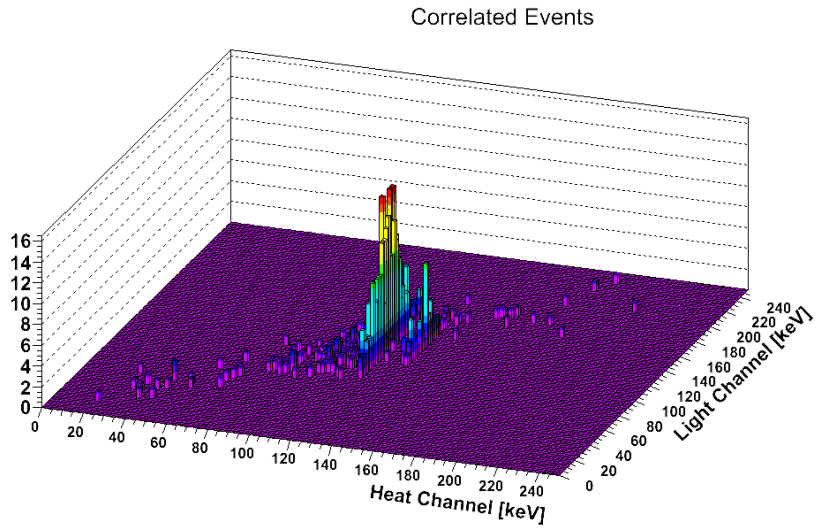


Figure 6.15: Correlated events of a typical data set.

This correlation is effectively applying a cut to the PMT signal. Using only the correlated events, the light channel photon number spectrum changes to that shown in Figure 6.16. The background and the pile-up peak at around 120 photons have disappeared.

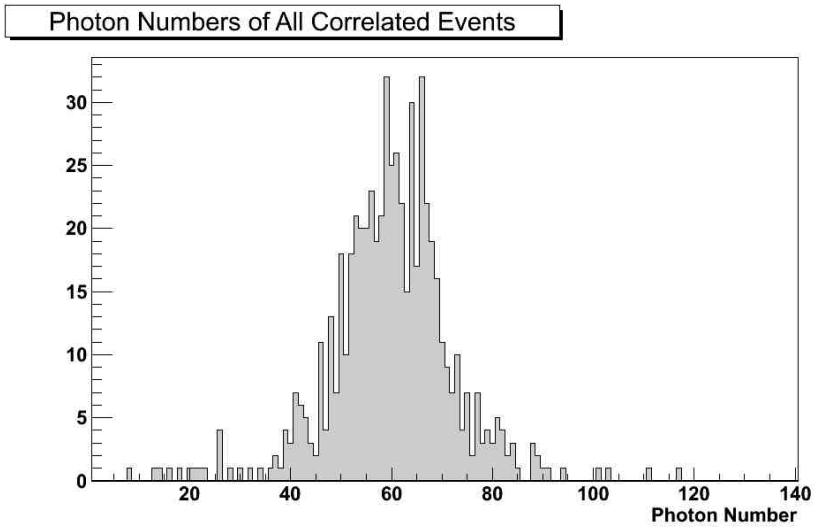


Figure 6.16: Photon number spectrum of correlated light channel scintillation events.

Using this correlation, the scintillations caused by incident particles with different energies can be separated because of the good resolution of the heat channel. For example, Figure 6.17 shows the peak corresponding to the 122.06 keV gammas from the cobalt-57 source.

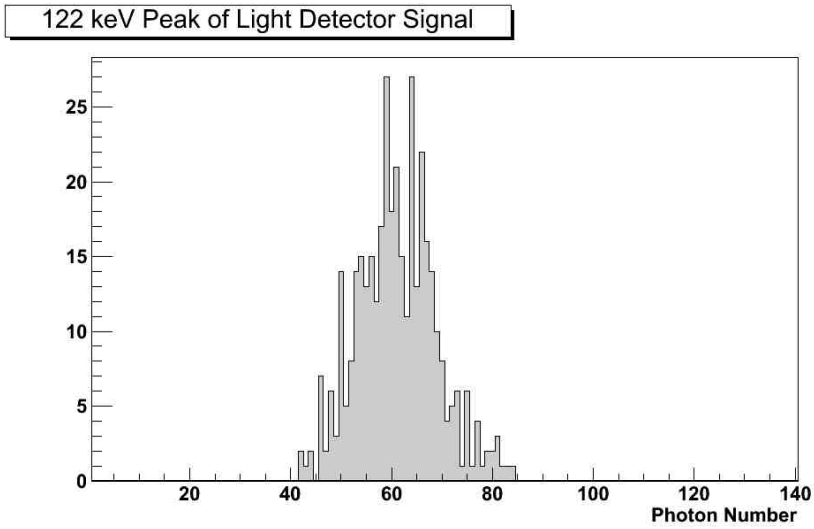


Figure 6.17: The 122.06 keV γ peak from a cobalt-57 source as measured by the light detector.

6.4 Energy Spectrum and Resolution

By studying the energy spectra from test runs, the resolution of the detector module can be determined. This section will present results obtained after the data analysis as introduced above, and discuss the detector performance.

6.4.1 Phonon Detector Energy Resolution

As discussed in Section 6.2, a number of different features are expected in the energy spectrum, which allows the resolution of the detector to be measured. Figure 6.18 shows the phonon channel energy spectrum from one of the test runs using cobalt-57 as radioactive source. The 122.06 keV and 136.47 keV γ-lines can be clearly seen as expected.

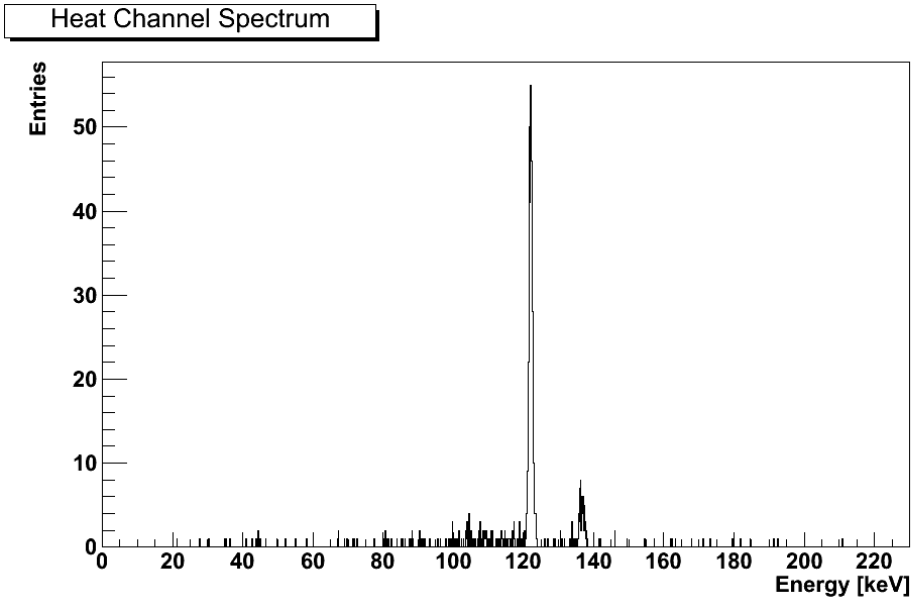


Figure 6.18: Energy spectrum of the phonon channel from a typical cobalt-57 test run.

This is obtained with the rigorous cut described above, and thus only a clean list of ideal events goes into this spectrum. Actually, some of the discarded pulses can be reinstated after the template pulse is produced. For example, pulses with large baseline gradients are cut to avoid distortions in the template pulse, but they could still be individually fitted with the slope of baseline accounted for, potentially giving

correct measurements of their energies. Distorted events can still be cut using the fitting quality. Therefore, Figure 6.19 can be obtained by taking the full list of events without any cut, applying the template fit to individual pulses and then cutting on the quality of fit, namely, chi-square. In this case, the total entries increase to 2.9 times of the previous value and features in the lower energy range become more visible in the spectrum.

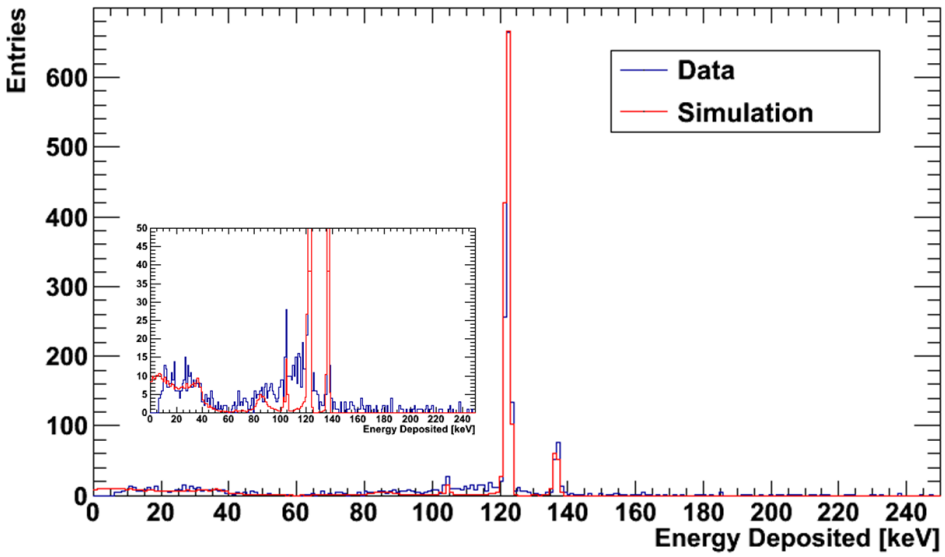


Figure 6.19: Phonon channel energy spectra. The spectrum with the blue line is obtained from measured data with only chi-square cut as described in text. The spectrum with the red line is the simulated result using GEANT4. The insert shows more details of the distribution below 122 keV.

Besides the prominent 122.06 keV and 136.47 keV γ-lines, other features caused by X-ray escaping and Compton scattering can also be seen in Figure 6.18 and Figure 6.19.

First of all, there is a continuous distribution at low energies up to ~40 keV. As discussed in Section 6.2, considering the relatively small crystal size, this is produced by the Compton scattering within the detector crystal.

A small peak at ~105 keV also appears in both spectra. Again, since the crystal is relatively small, the characteristic X-ray will not be re-absorbed completely. Therefore, this should be the contributions of the Mo escape peaks for 122 keV.

In addition, a population below the 122 keV peak appears in the spectra. This could contain contributions from several sources, for example, the backscattered gammas. The Mo escape peaks for 136 keV, expected to occur around 119 keV, could also be one contribution to distorting the low energy side of the 122 keV peak. Also, multiple Compton scattering of the escaping photons will soften features mentioned above, resulting in a contribution to this distribution below the 122 keV peak. The 136 keV peak is also broadened on the low energy side due to similar reasons.

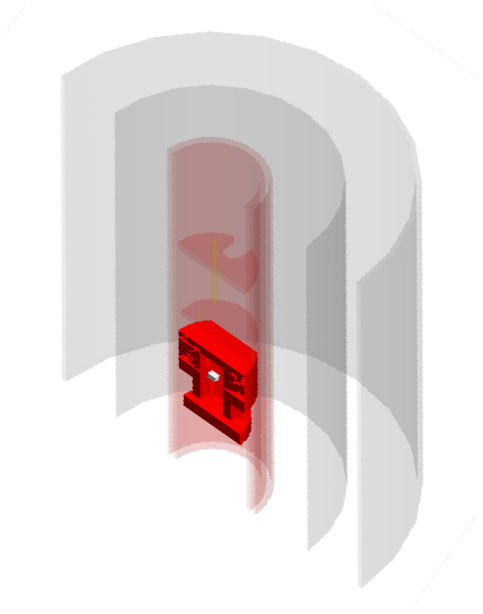


Figure 6.20: GEANT4 simulation geometry setup. The half cylinders represent the layered structure of OVC, IVC, 50 mK shielding, etc. Two experimental plates and the detector holder are shown in red, and the target crystal is shown in white.

Using GEANT4, effects from the presence of the cryostat structures, detector housing and the detector itself can be simulated. The result of the simulation is shown in Figure 6.19 as the red spectrum. Comparing it with the data, the ratio of 122 keV and 136 keV intensities matches nicely. The small features produced by Compton scattering in the detector crystal and surrounding materials, like the Compton edge,

and the Mo escape peak also matches in term of their positions. Their sizes depend largely on the source position, which changes from run to run due to various reasons, making it difficult to have an exact setup in the simulation. Further, the simulation only included the relatively large blocks of surrounding materials (Figure 6.20), which also affected the features produced by backscattered gammas. Therefore, the sizes only match broadly here. Nevertheless, the simulation sufficiently confirms the above understanding of the measured spectrum.

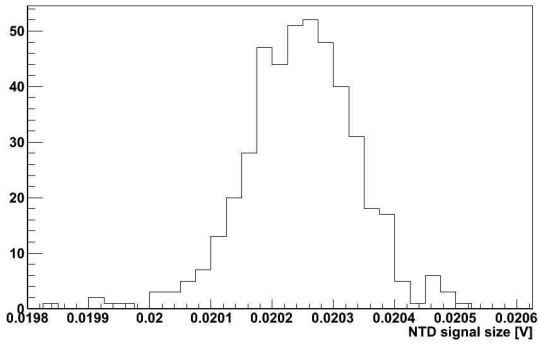


Figure 6.21: The 122 keV peak from cobalt-57 source.

The detector resolution is normally defined as the full width at half maximum (FWHM) of the full energy peak, which can be found from a Gaussian fit to that peak:

$$FWHM = 2\sqrt{2ln2}\sigma \approx 2.3548\sigma\,. \tag{6.5}$$

As discussed above, in reality, due to the size of the target crystal and secondary radiation, the full energy peaks are usually broadened on the low energy side as shown in Figure 6.21. Therefore, it will be more accurate to find the FWHM only fitting the high energy side of the peak.

The energy resolution of the phonon detector measured in a typical test run using cobalt-57 test source is listed in Table 6.4.

This shows that the resolution of the 122 keV peak deteriorates as the cut is relaxed. But the increased statistics helps to determine the 136 keV peak resolution better.

Phonon Detector (Figure 6.18)		
Peak Energy (keV)	**FWHM (keV)**	**FWHM (%)**
122.06	1.07 ± 0.10	0.88% ± 0.09%
136.47	1.60 ± 0.47	1.17% ± 0.35%
Phonon Detector (Figure 6.19)		
Peak Energy (keV)	**FWHM (keV)**	**FWHM (%)**
122.06	1.30 ± 0.07	1.07% ± 0.06%
136.47	1.41 ± 0.12	1.03% ± 0.08%

Table 6.4: FWHM of peaks at different energies for the phonon channel measured in a test run.

In real dark matter detection experiments, the crystal is normally much larger than the target crystal used in this work. Therefore, the extra features caused by photons escaping the crystal would be suppressed.

6.4.2 Light Detector Energy Resolution

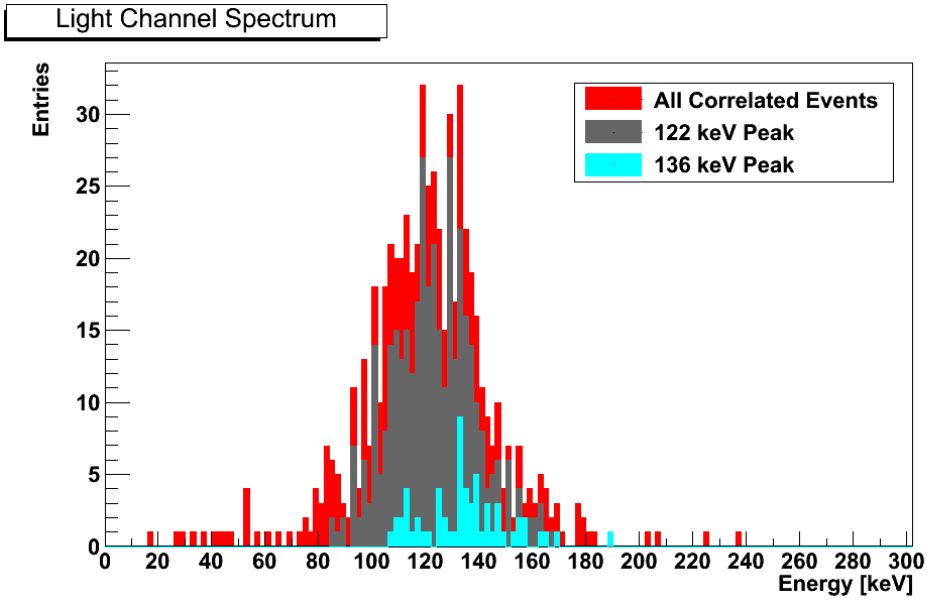


Figure 6.22: Energy spectrum of the light channel (red) from a typical cobalt-57 test run along with the 122 keV and the 136 keV peaks defined using correlation with the heat channel.

The typical light detector spectrum obtained after correlation is shown as the red histogram in Figure 6.22.

When energy is deposited in the target crystal after a particle interaction, only a small fraction of it is emitted as scintillation light, while the majority is converted into phonons. Limited by the statistical fluctuations of the scintillation process, the light channel resolution is expected to be much worse than the heat channel. As shown in Figure 6.18, the 122.06 keV peak and the 136.47 keV peak are combined as one prominent peak in the light channel spectrum. To define the 122 keV and the 136 keV peaks, the good energy resolution of heat channel is utilised as introduced previously. These peaks are also shown in Figure 6.22.

The correlation can also be done using the longer phonon channel event list, which is obtained with the more relaxed cut. The corresponding results are shown in Figure 6.23. As a result, the intensities of peaks increase and the low energy distribution produced by Compton scattering becomes visible in the light channel spectrum here.

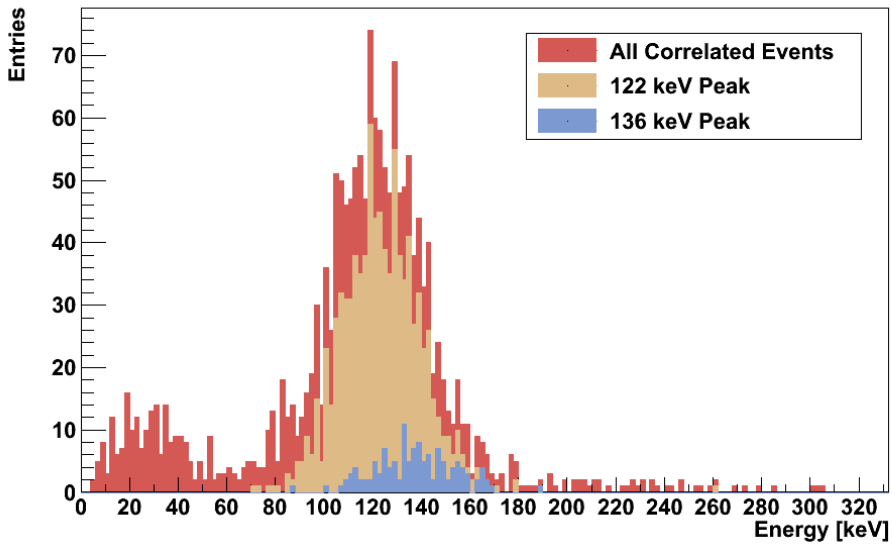


Figure 6.23: Light channel spectrum along with the 122 keV and the 136 keV peaks obtained after correlating with the longer phonon channel event list.

The corresponding FWHM is listed in Table 6.5. Similar to the phonon channel, the more relaxed cut makes the 122 keV peak resolution worse. But the increased number of entries helps in terms of determining the 136 keV peak resolution.

As discussed above, the photons from Compton scattering and the Mo escape photons are not all re-absorbed in the crystal. Some of these photons could be detected by the PMT as part of the scintillation events, which could then broaden the high energy side of the full energy peaks and worsen the detector resolution here. Again, for use of such detector module in future dark matter experiments, the target crystal will be larger, and thus this should not be an issue.

Light Detector (Figure 6.22)		
Peak Energy (keV)	**FWHM (keV)**	**FWHM (%)**
122.06	34.2 ± 1.8	28.0% ± 1.4%
136.47	57.7 ± 26.1	42.3% ± 19.1%
Light Detector (Figure 6.23)		
Peak Energy (keV)	**FWHM (keV)**	**FWHM (%)**
122.06	36.3 ± 1.0	29.7% ± 0.8%
136.47	42.8 ± 5.0	31.4% ± 3.7%

Table 6.5: FWHM of peaks at different energies for the light channel measured in a test run. The number of events in the 136 peak is too small to obtain a proper fit for calculating the corresponding resolution.

6.4.3 Light Collection

The energy resolution of the light detector can be affected by the effects of charge collection statistics, electronic noise, fluctuations in the scintillator and PMT responses, etc. The most important cause of peak broadening is normally the statistical spread, and the statistical fluctuations are most significant at the point where the number of information carriers is at a minimum. For the light detector setup in this work, this point is reached after the conversion at the PMT photocathode. The fractional FWHM contribution from this photoelectron statistics, which is usually

assumed to obey the Poisson statistics, is then proportional to $1/\sqrt{\overline{N}}$, where $\overline{N}$ is the mean value of the photoelectron number.

Given the scintillating crystal and the low-temperature PMT, this mean value is determined by the light collection efficiency. Therefore, it is a vital factor in improving the light detector resolution.

As introduced in Section 5.1.2, the inner walls of the detector holder are covered by a highly reflecting (> 98%) foil manufactured by 3M. Although a 4π full coverage is desired to ensure the maximum light collection efficiency, small gaps and holes have to be left for the gold bond wires and nylon fibres to pass through, as well as allowing gas to be pumped out during cooling. The light collection efficiency of the setup is estimated below.

The number of photoelectron can be calculated as:

$$N = E \cdot Y \cdot \eta \cdot \varepsilon\,, \tag{6.6}$$

where E is the deposited energy, Y is the scintillator light yield, η is the light collection efficiency and ε is the PMT photocathode quantum efficiency.

From Section 5.2, the light yield of $CaMoO_4$ is estimated to be 28 photon / keV. Then for the 122.06 keV gammas, the emitted photon number is about 3418. For the photocathode, its average quantum efficiency is estimated to be 8% based on information provided by the manufacturer[8]. The mean value N is around 60 (Figure 6.17). Thus, the estimated light collection efficiency is:

$$\eta = \frac{N}{E \cdot Y \cdot \varepsilon} = \frac{60}{122.06 \times 28 \times 0.08} = 21.9\%\,. \tag{6.7}$$

In previous work done by F.A. Danevich et al [126] and V. Alenkov et al [127], simulations show that for polished rectangular scintillators with an gap between the

[8] This value is based on the manufacturer's estimation of quantum efficiency at 420 nm and the fact that the PMT is not optimised for the scintillation spectrum of $CaMoO_4$.

crystal and PMT photocathode, the light collection efficiency would be around 25%. This is consistent with our estimation considering the non-perfect reflecting foil lining as mentioned above. These simulations also indicate that by diffusing the side surfaces of the crystal, the light collection efficiency may be further improved.

6.4.4 Light Yield Plot

Similar to the result obtained by EDELWEISS, CRESST and other dark matter experiments, the data from the detector module can be plotted in the light yield – energy plane as shown in Figure 6.24. The light yield is defined as E_{Light}/E_{Heat}, with the signals normalised such that the ratio is 1 for gamma ray interactions.

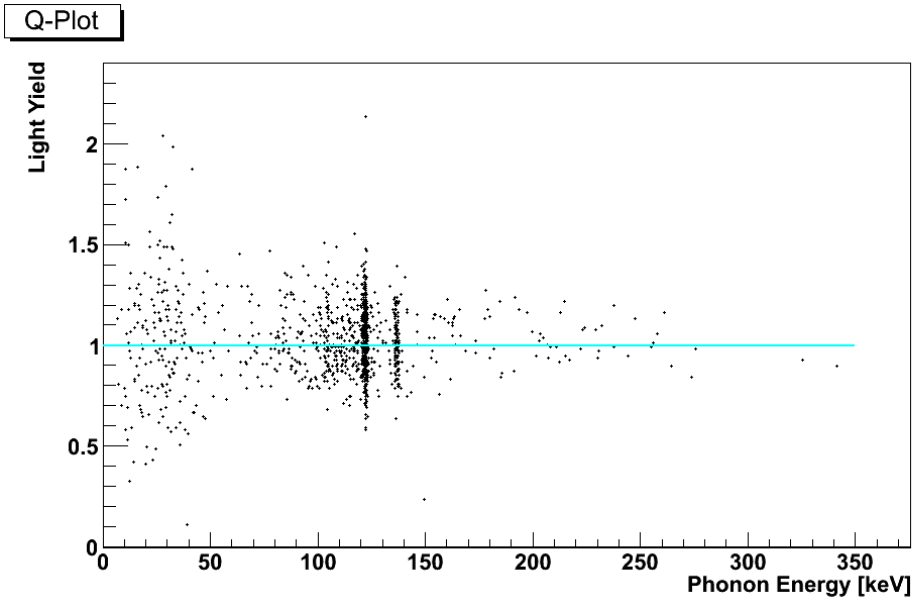


Figure 6.24: Light yield plot. Visible in the plot is the electron recoil band (centred at 1) from the γ-source. The observed width of the band is dominated by the light channel resolution.

As mentioned in Chapter 1, the light yield of nuclear recoils (WIMPs and neutrons) and that of electron recoils (electrons and photons) are different. Hence, this plot is useful for discrimination between the nuclear recoil events and the overwhelming electromagnetic background. With neutron exposures and enough calibration statistics, an electron recoil band and a nuclear recoil band can be

determined on the light yield plot, and the detector module will then be ready for electron recoil background discrimination.

6.5 Temperature Dependence of $CaMoO_4$ Scintillation Decay Time

As introduced in Section 5.2, properties of $CaMoO_4$ have been measured down to 7 K but no systematic studies at lower temperatures have been carried out so far. It is anticipated that the scintillation light yield of $CaMoO_4$ should not change with further cooling since there is no evidence suggesting otherwise. However, this is not the case for its decay constant. Previous studies indicate that the decay constant will increase below 7 K until it reaches a constant value [102, 128, 129, 130].

To provide more reliable data and to verify the indications from previous studies, the decay constant of $CaMoO_4$ at temperatures below 7 K down to milli-Kelvin is studied in parallel to testing the cryogenic phonon – scintillation detector.

6.5.1 Decay Constant Measurement

The scintillation properties of the $CaMoO_4$ crystal were previously investigated down to 7 K using a He-flow cryostat [102]. The same crystal is used here and its decay time is measured over the 17 mK – 6.4 K range.

From analysing the time structure of scintillation events, Figure 6.25 shows several scintillation decay curves of the $CaMoO_4$ target crystal measured at different temperatures.

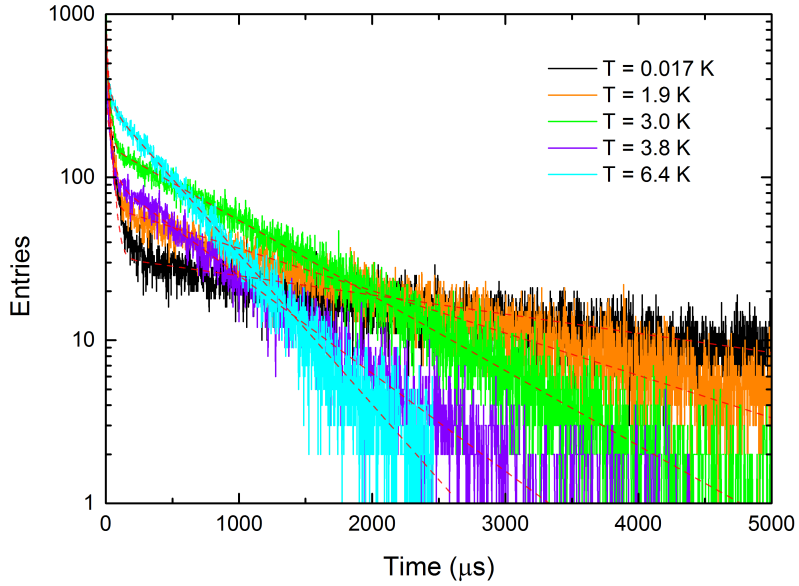


Figure 6.25: Examples of decay time spectra of scintillation in $CaMoO_4$ at different temperatures using γ excitation (^{57}Co). The red dash lines show the best fit using two exponentials.

It is obvious that the decay curves consist of both fast and slow components at low temperatures. Therefore, the experimental curves were fitted using a sum of two exponentials:

$$f(t) = A_f e^{-t/\tau_f} + A_s e^{-t/\tau_s}\,, \tag{6.8}$$

where τ_f and τ_s correspond to the time constants of the fast and slow components respectively.

The temperatures below 100 mK are deduced from the resistance of the NTD-Ge sensor attached to the $CaMoO_4$ crystal, using the generic calibration as shown in Figure 5.13[9]. At higher temperatures, this resistance becomes too small to give sensible readings, while a ruthenium oxide thermometer integrated within the K400 cryostat is within its reliable range. Hence the temperatures above 100 mK were

[9] X.-F. Navick, private communication: for a certain temperature, the resistance value from the generic calibration curve is likely to have a systematic error estimated at 20%. The error is mainly due to the fact that NTD-Ge is a piezoelectric material and the exact calibration will vary every time it is glued to a substrate.

obtained from the K400 operation monitoring system, which uses a generic calibration of a 2200 Ω RuO_2 resistor to measure the mixing chamber temperature.

6.5.2 Temperature Dependence

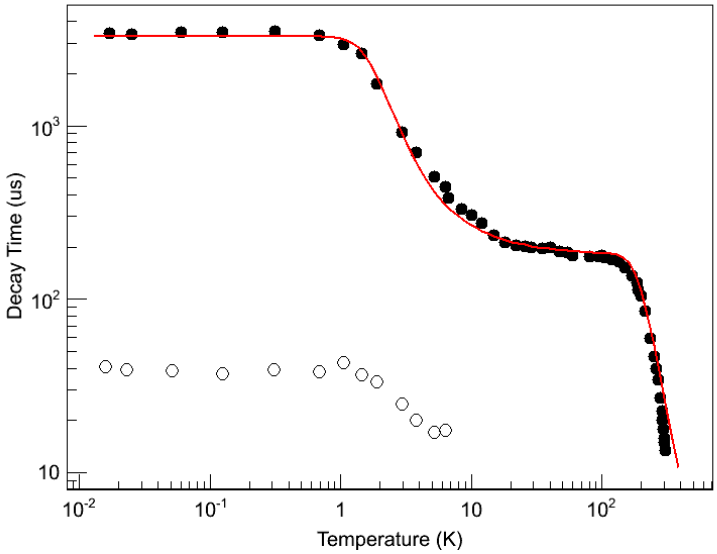


Figure 6.26: Temperature dependence of $CaMoO_4$ decay time. The black dots are the slow components and the black circles are the fast components. The red solid line shows the fit of the slow component using the three-level model explained in the text.

Combined with the results from our earlier measurements over the 7 – 291 K temperature range (slow component), the temperature dependence of $CaMoO_4$ decay time is plotted in Figure 6.26. Here, the data over 2 – 20 K measured separately using different methods are consistent with each other.

Figure 6.26 shows that τ_s is constant at low temperatures, but decreases rapidly at $T > 1$ K. It reduces by about one order of magnitude over the 1 – 20 K temperature range and then stays nearly constant until the temperature reaches around 180 K, when τ_s again starts to decrease rapidly at higher temperatures. There is no fast component data from earlier measurement, but it is obvious that τ_f is almost constant at low temperatures and starts to decrease at around 1 K.

This observed temperature dependence of the slow component can be interpreted by a three-level model consisting of a ground and two excited levels labelled as 0, 1 and 2 respectively as shown in Figure 6.27, which has been successfully used to explain decay kinetics of molybdates and tungstates.

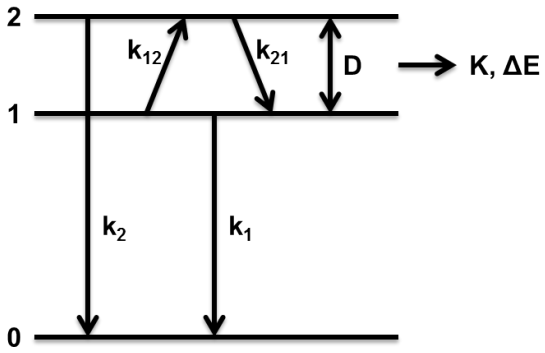


Figure 6.27: Three-level model used to interpret the temperature dependence of calcium molybdate scintillation decay time. Details are described in the text.

The key features of this model are suggested by Beard et al [131]. It is generally accepted that the luminescence of $CaMoO_4$, as well as other molybdates, is attributed to radiative transition of the triplet excited state of a self-trapped exciton[10] (STE) [132] localised at the oxyanion complex MoO_4^{2-}. Excitation of the emission centre to the upper-lying band is followed by relaxation to emission levels 2 and 1, of which the lower one is metastable [134, 136]. The emission transitions originate from the two triplet levels and terminate at the ground state. The metastable level is the cause of the increase of decay time at low temperatures (~1 – 20 K), and the rapid decrease at high temperatures ($\gtrsim$ 180 K) is attributed to processes of thermally activated quenching [131, 133].

The probabilities of radiative transitions from levels 1 and 2 are denoted as k_1 and k_2 respectively. The emitting levels are separated by an energy gap D and non-radiative transitions between these levels take place at rates k_{12} and k_{21}. The

[10] An exciton is a bound state of an electron-hole pair. A carrier can be immobilized by its own lattice distortion field, if there is a strong coupling of the carrier to the crystal lattice. An exciton involving such a carrier is generally described as a self-trapped exciton. More details can be found in [132].

probability for the emission centre to decay non-radiatively through the thermally activated process is $Kexp(-\Delta E/kT)$, where K is the decay rate and ΔE is the activation barrier. The formula for the radiative decay time constant is then given by the expression [134]:

$$\frac{1}{\tau_s} = \frac{k_1 + k_2 \exp(-D/kT)}{1 + \exp(-D/kT)} + Kexp(-\Delta E/kT). \quad \textbf{(6.9)}$$

This is used to fit the experimental results as shown in Figure 6.26. The fitting procedure is very sensitive to the selection of initial parameters and values of some parameters are with significant errors. To obtain the smallest χ^2, the fitting will favour the low temperature range due to the almost 3 orders of magnitude difference in decay time, without taking the physics meanings of the features in the curve into account. Therefore, to be more representative of the processes of thermally activated quenching in the high temperature range, the fitting is stopped by eye before reaching the lowest χ^2. The obtained values are summarised in the Table 1 together with published parameters from the fit of $\tau = f(T)$ dependences for other molybdates and tungstates.

Crystal	k_1 (s^{-1})	k_2 (s^{-1})	D (meV)	K (s^{-1})	ΔE (meV)
$CaMoO_4$	306 ± 1	10946 ± 804	0.64 ± 0.02	(3.0 ± 11.7) × 10^6	118 ± 76
$CaMoO_4$ [128]	330	8000	0.6	-	-
$CdMoO_4$ [135]	40	8000	0.07	-	-
$PbMoO_4$ [129]	6300	130000	0.37	1 × 10^5	260
$CdWO_4$ [129]	3120	95000	1.2	1.2 × 10^5	-
$ZnWO_4$ [129]	4980	58000	1.0	1 × 10^5	290
$ZnWO_4$ [130]	5000	33300	2.1	2 × 10^9	300

Table 6.6: Parameters of emission centre in $CaMoO_4$ (and for comparison, other molybdates and tungstates) obtained from fitting the temperature dependence of decay time (slow component) based on a three-level model.

The energy gap between the two emitting levels D in $CaMoO_4$ is smaller than the respective value in tungstates, this can explain the fact that the decay time keep

changing until the temperature falls below ~1 K, instead of, for example, ~10 K for $CaWO_4$.

This model does not include consideration of the fast component. It can be attributed to the radiative decay of upper-lying singlet states. Further discussion about electronic structure of the STE located on a tetrahedral oxyanion molecule is beyond the scope of this work and can be found in [136, 133].

Conclusions and Perspectives

The theme of this thesis is developing a scalable, robust cryogenic phonon-scintillation detector concept together with a radio-pure cabling system applicable down to milli-Kelvin temperatures for direct dark matter searches.

Firstly motivated by the need of building EDELWEISS-III, a two-section cabling solution that consists of semi-flexible laminated copper and stainless steel cables has been designed and produced in this work. Batches of prototypes have been tested in the K400 cryostat at Oxford and the EDELWEISS cryostat at the LSM underground laboratory, France. After being verified in these tests, a final set of cabling has been produced and installed in the EDELEISS-III setup, which is currently collecting more exposure in its science runs.

To achieve the sensitivity aimed for detecting WIMP-nucleon interactions in current and future dark matter direct detection experiments, strict control of radioactive background is crucial. Low heat conductivity of readout cabling is also vital for cryogenic experiments operating at milli-Kelvin range. The two-section design, with copper section in the detector vicinity and stainless steel section further away crossing different temperature levels, has enabled both the heatload and the radioactive background of this cabling solution to be low. The in-house production using carefully selected and assessed materials has given more control over the process and further helped limit the laminated cables' background contribution to be within the requirement of EDELWEISS-III. With proper design and heat anchoring,

detectors equipped with this cabling system can be cooled down to ~10 mK, as far as our tests show.

The cables are semi-flexible as a result of their layered construction. This then makes them more immune against microphonic noise. Also, the cold cabling system has shown similar electrical performance as the coaxial cabling when comparing different cold cabling configurations in EDELWEISS commissioning runs.

The increased target mass also yields more detectors in a cryogenic dark matter direct detection experiment like EDELWEISS and EURECA, which then poses more stringent limits on the material and space budget of cabling per detector. Individual design for each detector position has made the cables compatible with the compact cryostat design. Additionally, the assembled connectors have provided time-efficient and reliable connections as well as more flexibility in the setup.

In the future, this cabling solution will be suitable for the next generation dark matter searches. Besides that, the copper laminated cables are currently also being used to read out LUMINEU detectors at LSM, demonstrating the possibility of applying it to other rare event searches. Prototypes for even wider ranges of use, like infrastructure monitoring readout, have been produced at Oxford as well, showing a large potential of the solution.

For the next improvement, the most important aim will be finding an alternative metal contact material in the sockets. The key requirements for this material are: a) it maintains its elasticity down to ~10 mK; b) it does not contain elements that have a high (α, n) reaction cross-section; c) the overall radioactive contamination is low. One possible candidate is phosphor bronze. This needs to be a joint effort between the future dark matter direct detection collaboration and the metal socket manufacturer.

Besides, if new radiopure insulation materials with lower dielectric constant become available in the future, they may be used to further reduce the cable capacitance.

To improve the sensitivity reach in future dark matter searches, a large target mass at tonne-scale will be required, which then converts into thousands of cryogenic detectors. To be compatible with the scaling up, a novel phonon-scintillation cryogenic detector concept based on NTD-Ge sensor and low-temperature PMT with $CaMoO_4$ scintillating target crystal has been developed and tested in this work. For providing the high voltage DC power supply to the PMT without preventing the detector module from cooling down or affecting the performance of the phonon detector, a high voltage supply system based on CWG, transformer and small AC input has also been designed and studied here.

For the phonon detector, the NTD-Ge sensor was chosen as the thermometer because of its continuous exponential resistance - temperature relation. In a large cryogenic array, if the NTD-Ge sensors are all cut from the same wafer, then their characteristic curve should be very similar. Therefore, all detectors can be heatsunk to the same base temperature, instead of individually tuned and stabilised like TES. In our setup in the K400 cryostat at Oxford, a two-section semi-flexible laminated cabling was used for transferring the phonon channel signals from the detector to its front-end electronics at ~120 K. In a test run using a cobalt-57 gamma source, 1.07 keV was achieved for the FWHM of the 122.06 keV peak, which is close to what detectors used in the current dark matter direct detection achieve.

For the light detector, since only a small fraction of the deposited energy will transform into scintillation light, and it will not be collected by the light detector completely, the heat capacity of NTD-Ge sensor turned out to be too much to give a good resolution. Therefore, a low-temperature PMT from Hamamatsu was built into

our cryogenic detector as the light channel and its feasibility for operation at milli-Kelvin temperatures has been proven. As a standard technology, the PMTs have always been the preferable way of detecting scintillation light due to its excellent sensitivity for single photon detection and low noise. In the last decade, driven by experiments like noble liquid dark matter searches, a major research effort has been carried out to lower its radioactive contamination level, making it possible to be used in low-background experiments. Using PMT as the light channel will make the detector production and operation much easier compared to traditional cryogenic scintillation detectors. All PMTs can be powered with a common high voltage distribution and usually run smoothly due to their robustness. As they are commercially available, future collaborations can simply purchase them with a fixed price and guaranteed performance.

The PMT requires a DC high voltage around a few kilovolts. A power supply system that neither prevents the phonon detector from cooling to the cryogenic temperature it requires, nor deteriorates the signal quality of the heat channel, has been built. Only a few volts AC input from a function generator outside the cryostat is needed to provide the DC voltage required through the multiplication of a transformer at ~4 K and a CWG at ~0.7 K.

Tests have demonstrated that the detector module can be cooled down to and operated at ~17 mK. In a test run, the FWHM of the 122.06 keV peak is 34.2 keV (28.0%) for the light detector.

Besides applications in dark matter direct detection and other rare event searches, this work on PMT and HV supply could also be used for scintillator studies at cryogenic temperatures. In this thesis, the experimental data of $CaMoO_4$'s scintillation decay time has been extended from the previous ~7 K to ~17 mK. The

result has been interpreted by a three-level model, confirming the existence of a metastable emission level in CaMoO4 and giving various parameters of its emission centre.

Further improvements in the future are mainly focused on the light detector performance. In the next stage, $CaWO_4$ will be used as the scintillating absorber. Its scintillation spectrum will be a better fit to the quantum efficiency curve of the PMT used in this work, which could help to gain a factor of $\sqrt{2}$ in resolution. Further, the crystal surface will be made diffuse and the setup will be fine-adjusted to achieve better reflecting foil coverage. This may make the resolution even better. In the longer term, if a low-temperature PMT with higher quantum efficiency becomes available, this repeatable and scalable phonon-scintillation detector concept will be even more attractive to future dark matter experiments.

Appendix A

Test Results of Cockcroft-Walton Generator and PMT Base PCB

As the Cockcroft-Walton generator and the PMT base PCB are operated at temperatures below 1 K, the components should be suitable to be used in such environment. Candidate components for these circuits have been test down to liquid helium temperature before chosen. The results of these chosen components are listed here.

	CWG Capacitors	DC Isolation Capacitor	HV Stabilising Capacitor	Linearity Capacitors
Type	COG/NPO Ceramic			
Voltage Rating	50 V	2 kV	2 kV	1 kV
Quoted Capacitance	470 nF	1.2 nF	3.6 nF	12 nF
Room Temperature Capacitance (of Quoted)	100.6%	101.0%	101.5%	102.9%
77 K Capacitance (of Room Temperature)	100.2%	100.7%	100.1%	100.5%
4.2 K Capacitance (of Room Temperature)	99.6%	100.1%	99.7%	100.0%

Table A.1: Low-temperature performance of capacitors (typical samples) used in the CWG/PMT circuit. Measured at 10 kHz.

	DC Isolation Resistor (Two Resistors in Parallel)		Attenuator Resistor 1	Attenuator Resistor 2	Ratio
Type	Metal film		Thick film		
Voltage Rating	1.6 kV	350 V	2 kV	2 kV	
Quoted Resistance	2 MΩ	1 MΩ	1 GΩ	1 MΩ	
Room Temperature Resistance (of Quoted)	99.9%	100.0%	105.2%	99.8%	1054.9
77 K Resistance (of Room Temperature)	103.5%	101.2%	114.8%	104.7%	1156.6
4.2 K Resistance (of Room Temperature)	243.6%	103.9%	233.3%	169.1%	1454.5

Table A.2: Low-temperature performance of resistors (typical samples) used in the CWG/PMT circuit.

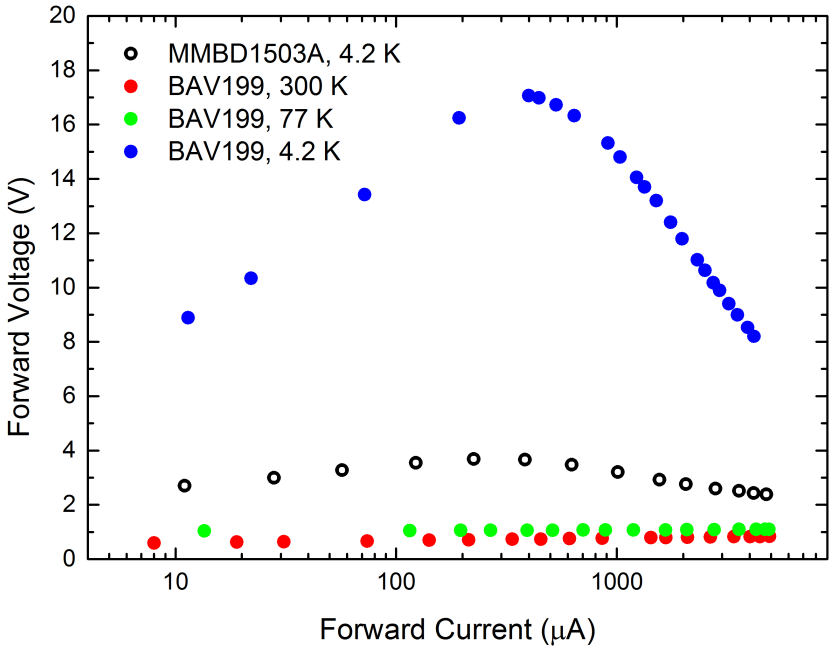


Figure A.1: Forward voltage vs. forward current. The MMBD1503A diode from Fairchild Semiconductor was tested at liquid helium temperature and used for the CWG board. Test results of another low leakage diode, BAV199 from Infineon Technologies, are also included here for comparison. The values are measured by M. Pipe.

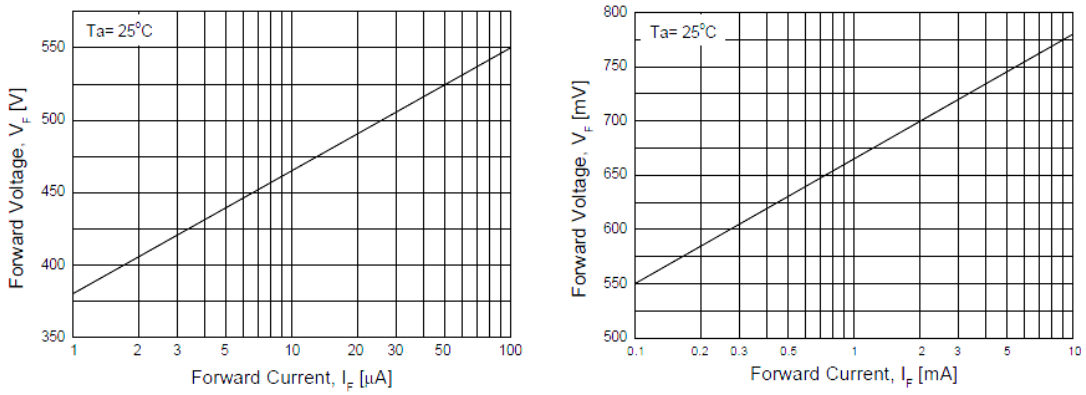


Figure A.2: Typical forward voltage vs. forward current curve of the MMBD1503A diode at 298 K. Taken from its datasheet [137].

Bibliography

[1] F. Zwicky, Die Rotverschiebung von extragalaktischen Nebeln. *Helv Phys Acta* **6**, 110-127 (1933).

[2] F. Zwicky, Republication of: The redshift of extragalactic nebulae. *Gen Relat Gravit* **41**, 207-224 (2009).

[3] V. C. Rubin, W. K. Ford Jr, Rotation of the Andromeda Nebula from a Spectroscopic Survey of Emission Regions. *Astrophys J* **159**, 379-379 (1970).

[4] M. S. Roberts, R. N. Whitehurst, The rotation curve and geometry of M31 at large galactocentric distances. *Astrophys J* **201**, 327-346 (1975).

[5] T. S. van Albada, J. N. Bahcall, K. Begeman, R. Sancisi, Distribution of dark matter in the spiral galaxy NGC 3198. *Astrophys J* **295**, 305-313 (1985).

[6] B. Fuchs, The Amount of Dark Matter in Spiral Galaxies, in *Dark Matter in Astro- and Particle Physics*, H. V Klapdor-Kleingrothaus, Ed. (Springer Berlin Heidelberg, 2001), pp. 25–32.

[7] A. Einstein, LENS-LIKE ACTION OF A STAR BY THE DEVIATION OF LIGHT IN THE GRAVITATIONAL FIELD. *Science* **84**, 506-507 (1936)

[8] G. Bertone, Ed., *Particle Dark Matter : Observations, Models and Searches* (Cambridge University Press, Cambridge, UK, 2010).

[9] C. Douglas, B. Maruša, H. G. Anthony, M. Maxim, W. R. Scott, J. Christine, Z. Dennis, A Direct Empirical Proof of the Existence of Dark Matter. *The Astrophysical Journal Letters* **648**, L109 (2006).

[10] M. Fukugita, C. J. Hogan, P. J. E. Peebles, The Cosmic Baryon Budget. *The Astrophysical Journal* **503**, 518 (1998).

[11] A. Friedman, Über die Krümmung des Raumes. *Z. Physik* **10**, 377-386 (1922).

[12] A. Friedman, On the Curvature of Space. *Gen Relat Gravit* **31**, 1991-2000 (1999).

[13] A. Liddle, *An introduction to modern cosmology* (Chichester : Wiley, Chichester, 2nd ed.., 2003).

[14] K. Freese, *The cosmic cocktail : three parts dark matter* (Princeton, New Jersey : Princeton University Press, 2014), *Science essentials (National Academy of Sciences (U.S.)) Y.*

[15] D. D. Reid, D. W. Kittell, E. E. Arsznov, G. B. Thompson, The Picture of our universe: A View from modern cosmology. (2002). arXiv:astro-ph/0209504v2.

[16] Planck Collaboration, Planck 2013 results. XVI. Cosmological parameters. *A&A* **571**, A16 (2014).

[17] G. Steigman, Primordial Nucleosynthesis in the Precision Cosmology Era. *Annual Review of Nuclear and Particle Science* **57**, 463-491 (2007).

[18] K. Nakamura, et al. (Particle Data Group), Review of Particle Physics. *Journal of Physics G: Nuclear and Particle Physics* **37**, 075021 (2010).

[19] J. M. Overduin, P. S. Wesson, Dark matter and background light. *Physics Reports* **402**, 267-406 (2004).

[20] E. A. Baltz, Dark matter candidates. (2004). arXiv:astro-ph/0412170.

[21] J. R. Primack, Dark Matter and Galaxy Formation. *AIP Conference Proceedings* **1192**, 101-137 (2009)

[22] J. L. Feng, Dark Matter Candidates from Particle Physics and Methods of Detection. *Annual Review of Astronomy and Astrophysics* **48**, 495-545 (2010).

[23] L. Bergström, Dark matter candidates. *New Journal of Physics* **11**, 105006 (2009).

[24] J. D. Lewin, P. F. Smith, Review of mathematics, numerical factors, and corrections for dark matter experiments based on elastic nuclear recoil. *Astroparticle Physics* **6**, 87-112 (1996).

[25] J. Engel, Nuclear form factors for the scattering of weakly interacting massive particles. *Physics Letters B* **264**, 114-119 (1991).

[26] G. Jungman, M. Kamionkowski, K. Griest, Supersymmetric dark matter. *Physics Reports* **267**, 195-373 (1996).

[27] D. R. Tovey, R. J. Gaitskell, P. Gondolo, Y. Ramachers, L. Roszkowski, A new model-independent method for extracting spin-dependent cross section limits from dark matter searches. *Physics Letters B* **488**, 17-26 (2000).

[28] G. Angloher, et al., Results from 730 kg days of the CRESST-II Dark Matter search. *The European Physical Journal C* **72**, 1-22 (2012).

[29] CDMS Collaboration, Silicon Detector Dark Matter Results from the Final Exposure of CDMS II. *Physical Review Letters* **111**, 251301 (2013).

[30] A. Brown, S. Henry, H. Kraus, C. McCabe, Extending the CRESST-II commissioning run limits to lower masses. *Phys Rev D* **85**, 021301 (2012).

[31] G. Angloher, et al., Results on low mass WIMPs using an upgraded CRESST-II detector. *The European Physical Journal C* **74**, 1-6 (2014).

[32] SuperCDMS Collaboration, Search for Low-Mass Weakly Interacting Massive Particles with SuperCDMS. *Physical Review Letters* **112**, 241302 (2014).

[33] D. Y. Akimov, et al., WIMP-nucleon cross-section results from the second science run of ZEPLIN-III. *Physics Letters B* **709**, 14-20 (2012).

[34] LUX Collaboration, First Results from the LUX Dark Matter Experiment at the Sanford Underground Research Facility. *Physical Review Letters* **112**, 091303 (2014).

[35] D. C. Malling, et al., After LUX: The LZ Program. (2011). arXiv:1110.0103v2.

[36] XENON100 Collaboration, Dark Matter Results from 225 Live Days of XENON100 Data. *Physical Review Letters* **109**, 181301 (2012).

[37] P. Agnes, et al., First results from the DarkSide-50 dark matter experiment at Laboratori Nazionali del Gran Sasso. *Physics Letters B* **743**, 456-466 (2015).

[38] XMASS Collaboration, Search for Bosonic Superweakly Interacting Massive Dark Matter Particles with the XMASS-I Detector. *Physical Review Letters* **113**, 121301 (2014).

[39] M. G. Boulay for the DEAP Collaboration, DEAP-3600 Dark Matter Search at SNOLAB. *Journal of Physics: Conference Series* **375**, 012027 (2012).

[40] S. Archambault, et al., Constraints on low-mass WIMP interactions on 19F from PICASSO. *Physics Letters B* **711**, 153-161 (2012).

[41] COUPP Collaboration, First dark matter search results from a 4-kg CF3I bubble chamber operated in a deep underground site. *Phys Rev D* **86**, 052001 (2012).

[42] PICO Collaboration, Dark Matter Search Results from the PICO-2L C3F8 Bubble Chamber. (2015). arXiv:1503.00008v1.

[43] R. Bernabei, et al., Final model independent results of DAMA/LIBRA-phase1 and perspectives of phase2. *Phys. Part. Nuclei* **46**, 138-146 (2015).

[44] L. Baudis, Direct dark matter detection: The next decade. *Physics of the Dark Universe* **1**, 94-108 (2012).

[45] L. Baudis, WIMP dark matter direct-detection searches in noble gases. *Physics of the Dark Universe* **4**, 50-59 (2014).

[46] P. Cushman, et al., Snowmass CF1 Summary: WIMP Dark Matter Direct Detection. (2013). arXiv:1310.8327v2 [hep-ex].

[47] The Super-Kamiokande Collaboration, An Indirect Search for Weakly Interacting Massive Particles in the Sun Using 3109.6 Days of Upward-going Muons in Super-Kamiokande. *The Astrophysical Journal* **742**, 78 (2011).

[48] IceCube Collaboration, Multiyear search for dark matter annihilations in the Sun with the AMANDA-II and IceCube detectors. *Phys Rev D* **85**, 042002 (2012).

[49] T. Gaisser, F. Halzen, IceCube. *Annual Review of Nuclear and Particle Science* **64**, 101-123 (2014).

[50] F. Donato, Indirect searches for dark matter. *Physics of the Dark Universe* **4**, 41-43 (2014).

[51] Fermi-LAT Collaboration, Dark matter constraints from observations of 25 Milky Way satellite galaxies with the Fermi Large Area Telescope. *Phys Rev D* **89**, 042001 (2014).

[52] C. Ilias, P. F. Douglas, G. Lisa, W. Neal, The PAMELA positron excess from annihilations into a light boson. *Journal of Cosmology and Astroparticle Physics* **2009**, 007 (2009).

[53] O. Adriani, et al., Cosmic-Ray Positron Energy Spectrum Measured by PAMELA. *Physical Review Letters* **111**, 081102 (2013).

[54] AMS Collaboration, High Statistics Measurement of the Positron Fraction in Primary Cosmic Rays of 0.5–500 GeV with the Alpha Magnetic Spectrometer on the International Space Station. *Physical Review Letters* **113**, 121101 (2014).

[55] DELPHI Collaboration, Photon events with missing energy in e + e- collisions at √s = 130 to 209 GeV. *Eur. Phys. J. C* **38**, 395-411 (2005).

[56] DELPHI Collaboration, Search for one large extra dimension with the DELPHI detector at LEP. *The European Physical Journal C* **60**, 17-23 (2009).

[57] CDF Collaboration, Search for Dark Matter in Events with One Jet and Missing Transverse Energy in $p\bar{p}$ Collisions at √s = 1.96 TeV, *Physical Review Letters* **108**, 211804 (2012).

[58] V. A. MITSOU, SHEDDING LIGHT ON DARK MATTER AT COLLIDERS. *International Journal of Modern Physics A* **28**, 1330052 (2013).

[59] ATLAS Collaboration, Search for new phenomena in final states with an energetic jet and large missing transverse momentum in pp collisions at √s =8 TeV with the ATLAS detector. *The European Physical Journal C* **75**, 1-43 (2015).

[60] EDELWEISS Collaboration, Final results of the EDELWEISS-I dark matter search with cryogenic heat-and-ionization Ge detectors. *Phys Rev D* **71**, 122002 (2005).

[61] G. Heuermann, EDELWEISS-III dark matter search: first results and future. Talk given at *the 25th International Workshop on Weak Interactions and Neutrinos*, 2015 June 08-13, Heidelberg, Germany.

[62] A. Juillard, Status and prospects of the EDELWEISS-III direct WIMP search experiment. Talk given in *the 16th International Workshop on Low Temperature Detectors*, 2015 July 20-24, Grenoble, France.

[63] B. Schmidt, et al., Muon-induced background in the EDELWEISS dark matter search. *Astroparticle Physics* **44**, 28-39 (2013).

[64] J. Gascon, N. Bastidon, for the EDELWEISS Collaboration, The EDELWEISS-III Project and the Rejection Performance of Its Cryogenic Germanium Detectors. *Journal of Low Temperature Physics*, 1-6 (2014).

[65] EDELWEISS Collaboration, A new high-background-rejection dark matter Ge cryogenic detector. *Physics Letters B* **681**, 305-309 (2009).

[66] B. Censier, et al. for the EDELWEISS Collaboration, EDELWEISS Read-out Electronics and Future Prospects. *Journal of Low Temperature Physics* **167**, 645-651 (2012).

[67] G. A. Cox, et al, A multi-tiered data structure and process management system based on ROOT and CouchDB. *Nuclear Instruments and Methods in Physics Research Section A: Accelerators, Spectrometers, Detectors and Associated Equipment* **684**, 63-72 (2012).

[68] EDELWEISS Collaboration, Final results of the EDELWEISS-II WIMP search using a 4-kg array of cryogenic germanium detectors with interleaved electrodes. *Physics Letters B* **702**, 329-335 (2011).

[69] EDELWEISS Collaboration, Background studies for the EDELWEISS dark matter experiment. *Astroparticle Physics* **47**, 1-9 (2013).

[70] The EURECA Collaboration, EURECA Conceptual Design Report. *Physics of the Dark Universe*, **3**, 41–74 (2014).

[71] D. L. Vanek, Selective electrofinishing. *Metal Finishing* **100, Supplement 1**, 345-358 (2002).

[72] D. S. Akerib, et al., Design and performance of a modular low-radioactivity readout system for cryogenic detectors in the CDMS experiment. *Nucl Instrum Meth A* **591**, 476-489 (2008).

[73] N. Ensslin, The Origin of Neutron Radiation, in *Passive Nondestructive Assay Nuclear Materials (NUREG/CR-5550)* (1991), pp. 337 – 356.

[74] J. B. Marion, F. C. Young, *Nuclear Reaction Analysis* (John Wiley & Sons, Inc., New York, 1968).

[75] Apical polyimide film datasheet, http://www.gts-flexible.com/

[76] E. H. Lee, Ion Beam Modification of Polyimides, in *Polyimides: Fundamentals and Applications*, M. K. Ghosh, K. L. Mittal, Eds. (Marcel Dekker, Inc., New York, 1996).

[77] Delrin datasheet, http://www.pds-arden.co.uk/

[78] E. Bogatin, *Signal and Power Integrity - Simplified* (Prentice Hall, Upper Saddle River, N.J., 2nd ed., 2010), *Prentice Hall modern semiconductor design series. Prentice Hall signal integrity library. Y*.

[79] D. C. Meeker, Finite Element Method Magnetics, Version 4.2 (01Oct2011 Build), http://www.femm.info

[80] T. P. Murphy, E. C. Palm, L. Peabody, S. W. Tozer, Capacitance thermometer for use at low temperatures and high magnetic fields. *Review of Scientific Instruments* **72**, 3462-3466 (2001).

[81] Oxford Instruments, Kelvinox Dilution Refrigerator System: Operator's Handbook.

[82] F. Pobell, *Matter and Methods at Low Temperatures* (Springer-Verlag, 1992).

[83] J. W. Ekin, *Experimental Techniques for Low-temperature Measurements* (Oxford University Press, 2006).

[84] D. L. Rule, D. R. Smith, L. L. Sparks, Thermal Conductivity of a Polymide Film Between 4.2 and 300K, with and without Alumina Particles as Filler. (1990). NISTIR 1990:3948

[85] A. Bergmann, M. Kaveh, N. Wiser, Explanation of the anomalous T 4 behaviour of the low-temperature electrical resistivity of silver. *Journal of Physics F: Metal Physics* **10**, L71 (1980).

[86] E. Borchi, S. D. Gennaro, On the low-temperature electrical resistivity of copper and gold. *Journal of Physics F: Metal Physics* **10**, L271 (1980).

[87] M. Barucci, L. Lolli, L. Risegari, G. Ventura, Measurement of thermal conductivity of the supports of CUORE cryostat. *Cryogenics* **48**, 166-168 (2008).

[88] J. Lawrence, A. B. Patel, J. G. Brisson, The thermal conductivity of Kapton HN between 0.5 and 5 K. *Cryogenics* **40**, 203-207 (2000).

[89] R. Radebaugh, N. V. Frederick, J. D. Siegwarth, Flexible laminates for thermally grounded terminal strips and shielded electrical leads at low temperatures. *Cryogenics* **13**, 41-43 (1973).

[90] S. Pirro, et al., Vibrational and thermal noise reduction for cryogenic detectors. *Nuclear Instruments and Methods in Physics Research Section A: Accelerators, Spectrometers, Detectors and Associated Equipment* **444**, 331-335 (2000).

[91] A. Raccanelli, L. A. Reichertz, E. Kreysa, Eliminating the vibrational noise in continuously filled 1 K pots. *Cryogenics* **41**, 763-766 (2001).

[92] P. Gorla, C. Bucci, S. Pirro, Complete elimination of 1K Pot vibrations in dilution refrigerators. Nuclear Instruments and Methods in Physics Research Section A: Accelerators, Spectrometers, Detectors and Associated Equipment **520**, 641-643 (2004).

[93] A. S. Barabash, et al., Enriched Zn100MoO4 scintillating bolometers to search for 0ν2β decay of 100Mo with the LUMINEU experiment. *The European Physical Journal C* **74**, 1-7 (2014).

[94] P. Coulter, *Cryogenic phonon-scintillation detectors with NTD germanium readout*. D.Phil thesis, University of Oxford. (2013).

[95] Y. H. Kim, et al., Measurements and modeling of the thermal properties of a calorimeter having a sapphire absorber. *Nuclear Instruments and Methods in Physics Research Section A: Accelerators, Spectrometers, Detectors and Associated Equipment* **520**, 208-211 (2004).

[96] G. B. Kim, et al., Thermal Model and Optimization of a Large Crystal Detector Using a Metallic Magnetic Calorimeter. *Journal of Low Temperature Physics* **176**, 637-643 (2014).

[97] M. Schwark, F. Pobell, W. P. Halperin, C. Buchal, J. Hanssen, M. Kubota, R. M. Mueller, Ortho-para conversion of hydrogen in copper as origin of time-dependent heat leaks. *Journal of Low Temperature Physics* **53**, 685-694 (1983).

[98] M. F. Weber, C. A. Stover, L. R. Gilbert, T. J. Nevitt, A. J. Ouderkirk, Giant Birefringent Optics in Multilayer Polymer Mirrors. *Science* **287**, 2451-2456 (2000).

[99] NIST, http://www.nist.gov/pml/data/star/index.cfm

[100] NIST, http://www.nist.gov/pml/data/xraycoef/index.cfm

[101] V. B. Mikhailik, H. Kraus, Performance of scintillation materials at cryogenic temperatures. *physica status solidi (b)* **247**, 1583-1599 (2010).

[102] V. B. Mikhailik, S. Henry, H. Kraus, I. Solskii, Temperature dependence of CaMoO4 scintillation properties. *Nuclear Instruments and Methods in Physics*

Research Section A: Accelerators, Spectrometers, Detectors and Associated Equipment **583**, 350-355 (2007).

[103] M. Moszyński, M. Balcerzyk, W. Czarnacki, A. Nassalski, T. Szczęśniak, H. Kraus, V. B. Mikhailik, I. M. Solskii, Characterization of CaWO4 scintillator at room and liquid nitrogen temperatures. *Nuclear Instruments and Methods in Physics Research Section A: Accelerators, Spectrometers, Detectors and Associated Equipment* **553**, 578-591 (2005).

[104] I. M. Solskii, D. Y. Sugak, M. M. Vakiv, Growing Large Size Complex Oxide Single Crystals by Czochralski Technique for Electronic Devices. *Acta Phys Pol A* **124**, 314-320 (2013).

[105] I. S. Shlimak, Neutron transmutation doping in semiconductors: Science and applications. *Phys. Solid State* **41**, 716-719 (1999).

[106] N. P. Palaio, M. Rodder, E. E. Haller, E. Kreysa, Neutron-transmutation-doped germanium bolometers. *Int J Infrared Milli Waves* **4**, 933-943 (1983).

[107] P. W. Anderson, Absence of Diffusion in Certain Random Lattices. *Phys Rev* **109**, 1492-1505 (1958).

[108] N. F. Mott, W. D. Twose, The theory of impurity conduction. *Advances in Physics* **10**, 107-163 (1961).

[109] D. McCammon, in *Cryogenic Particle Detection,* C. Enss, Ed. (Springer Berlin Heidelberg, 2005), vol. 99, chap. 2, pp. 35-62.

[110] A. L. Efros, B. I. Shklovskii, Coulomb gap and low temperature conductivity of disordered systems. *Journal of Physics C: Solid State Physics* **8**, L49 (1975).

[111] A. Senyshyn, H. Kraus, V. B. Mikhailik, L. Vasylechko, M. Knapp, Thermal properties of CaMoO4: Lattice dynamics and synchrotron powder diffraction studies. *Physical Review B* **73**, 014104 (2006).

[112] S. J. Lee, et al., The development of a cryogenic detector with CaMoO4 crystals for neutrinoless double beta decay search. *Astroparticle Physics* **34**, 732-737 (2011).

[113] E. Olivieri, M. Barucci, J. Beeman, L. Risegari, G. Ventura, Excess Heat Capacity in NTD Ge Thermistors. *Journal of Low Temperature Physics* **143**, 153-162 (2006).

[114] S. Kelham, H. M. Rosenberg, The thermal conductivity and specific heat of epoxy-resin from 0.1-80K. *Journal of Physics C: Solid State Physics* **14**, 1737 (1981).

[115] C. I. Nicholls, H. M. Rosenberg, The excitation spectrum of epoxy resins; neutron diffraction, specific heat and thermal conductivity at low temperatures. *Journal of Physics C: Solid State Physics* **17**, 1165 (1984).

[116] H. Kraus, V. B. Mikhailik, First test of a cryogenic scintillation module with a CaWO4 scintillator and a low-temperature photomultiplier down to 6K. *Nuclear Instruments and Methods in Physics Research Section A: Accelerators, Spectrometers, Detectors and Associated Equipment* **621**, 395-400 (2010).

[117] Hamamatsu R8520-06 PMT datasheet, http://www.hamamatsu.com/

[118] C. K. Dwivedi, M. B. Daigavane, Multi-purpose low cost DC high voltage generator (60 kV output), using Cockcroft-Walton voltage multiplier circuit. *International Journal of Science and Technology Education Research* **2**, 109-119 (2011).

[119] Blaze labs research, http://blazelabs.com/e-exp15.asp

[120] F. Teyssandier, D. Prêle, Commercially Available Capacitors at Cryogenic Temperatures, in *Ninth International Workshop on Low Temperature Electronics - WOLTE9*. (Guaruja, Brazil, 2010). <hal-00623399>

[121] S. Ingleby, *Cryodetector readout for direct dark matter searches*. D.Phil thesis, University of Oxford. (2013).

[122] Nucleonica Wiki, http://www.nucleonica.net/wiki/index.php?title=Decay_Schemes.

[123] M.-M. Bé *et al.*, *Table of Radionuclides* (Bureau International des Poids et Mesures, Pavillon de Breteuil, F-92310 Sèvres, France, 2004), vol. 1 of *Monographie BIPM-5*.

[124] R. D. Deslattes, E. G. Kessler, P. Indelicato, L. de Billy, E. Lindroth, J. Anton, X-ray transition energies: new approach to a comprehensive evaluation. *Reviews of Modern Physics* **75**, 35-99 (2003).

[125] Tables of Physical & Chemical Constants (16th edition 1995). 2.1.4 Hygrometry. Kaye & Laby Online. Version 1.0 (2005), www.kayelaby.npl.co.uk

[126] F. A. Danevich, V. V. Kobychev, R. V. Kobychev, H. Kraus, V. B. Mikhailik, V. M. Mokina, I. M. Solsky, Impact of geometry on light collection efficiency of scintillation detectors for cryogenic rare event searches. *Nuclear Instruments and Methods in Physics Research Section B: Beam Interactions with Materials and Atoms* **336**, 26-30 (2014).

[127] V. Alenkov, O. A. Buzanov, N. Khanbekov, V. N. Kornoukhov, H. Kraus, V. B. Mikhailik, V. A. Shuvaeva, Application of the Monte-Carlo refractive index matching (MCRIM) technique to the determination of the absolute light yield of a calcium molybdate scintillator. *Journal of Instrumentation* **8**, P06002 (2013).

[128] J. A. Groenink, C. Hakfoort, G. Blasse, The Luminescence of Calcium Molybdate. *physica status solidi (a)* **54**, 329-336 (1979).

[129] V. Babin, P. Bohacek, E. Bender, A. Krasnikov, E. Mihokova, M. Nikl, N. Senguttuvan, A. Stolovits, Y. Usuki, S. Zazubovich, Decay kinetics of the green emission in tungstates and molybdates. *Radiation Measurements* **38**, 533-537 (2004).

[130] M. Itoh, T. Kajitani, Decay kinetics of the triplet luminescence from self-trapped excitons in CdMoO4 and ZnWO4. *physica status solidi (b)* **248**, 422-425 (2011).

[131] G. B. Beard, W. H. Kelly, M. L. Mallory, Temperature Dependent Luminescence of CaWO4 and CdWO4. *Journal of Applied Physics* **33**, 144-147 (1962).

[132] R. T. Williams, K. S. Song, The self-trapped exciton. *Journal of Physics and Chemistry of Solids* **51**, 679-716 (1990).

[133] M. Itoh, T. Kajitani, Polarized luminescence from Jahn-Teller split triplet states of self-trapped excitons in PbMoO4. *Physical Review B* **87**, 085201 (2013).

[134] V. B. Mikhailik, H. Kraus, S. Henry, A. J. B. Tolhurst, Scintillation studies of CaWO4 in the millikelvin temperature range. *Physical Review B* **75**, 184308 (2007).

[135] A. Kotlov, L. Jönsson, H. Kraus, V. Mikhailik, V. Nagirnyi, G. Svensson, B. I. Zadneprovski, Excited states of molybdenum oxyanion in scheelite and wolframite structures. *Radiation Measurements* **42**, 767-770 (2007).

[136] V. B. Mikhailik, H. Kraus, M. Itoh, D. Iri, M. Uchida, Radiative decay of self-trapped excitons in CaMoO 4 and MgMoO 4 crystals. *Journal of Physics: Condensed Matter* **17**, 7209 (2005).

[137] Fairchild Semiconductor MMBD1503A diode datasheet, https://www.fairchildsemi.com